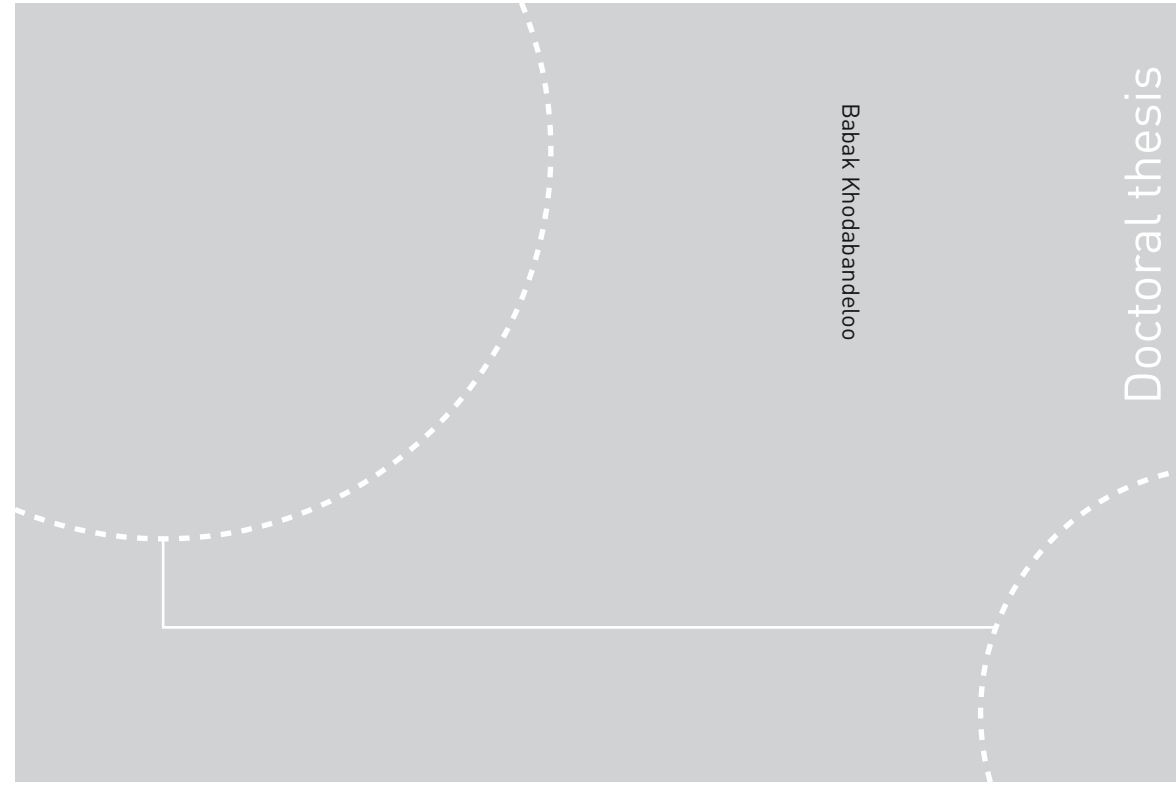


ISBN 978-82-326-3268-8 (printed ver.)
ISBN 978-82-326-3269-5 (electronic ver.)
ISSN 1503-8181



Doctoral theses at NTNU, 2018:239

Babak Khodabandeloo

Modeling and characterizing acoustic signals from cavity clouds generated by marine seismic air-gun arrays

Implications for marine mammals

 **NTNU**
Norwegian University of
Science and Technology

Doctoral theses at NTNU, 2018:239

 NTNU

NTNU
Norwegian University of Science and Technology
Thesis for the Degree of
Philosophiae Doctor
Faculty of Engineering
Department of Geoscience and Petroleum

 **NTNU**
Norwegian University of
Science and Technology

Babak Khodabandeloo

Modeling and characterizing acoustic signals from cavity clouds generated by marine seismic air-gun arrays

Implications for marine mammals

Thesis for the Degree of Philosophiae Doctor

Trondheim, August 2018

Norwegian University of Science and Technology
Faculty of Engineering
Department of Geoscience and Petroleum



Norwegian University of
Science and Technology

NTNU
Norwegian University of Science and Technology

Thesis for the Degree of Philosophiae Doctor

Faculty of Engineering
Department of Geoscience and Petroleum

© Babak Khodabandeloo

ISBN 978-82-326-3268-8 (printed ver.)
ISBN 978-82-326-3269-5 (electronic ver.)
ISSN 1503-8181

Doctoral theses at NTNU, 2018:239

Printed by NTNU Grafisk senter

Abstract

Marine seismic air-gun arrays generate not only low-frequency ($< \sim 300$ Hz) acoustic waves which benefit seismic imaging, but also high-frequencies up to tens of kilohertz. Although such high-frequencies are much weaker than the low-frequency parts, they might impact cetacean species that are sensitive to acoustic signals in the high-frequency range (10–150 kHz). Ghost cavitation is believed to be the main underlying mechanism for such high-frequency (>10 kHz) acoustic signals.

In this doctoral thesis, ghost cavitation phenomenon is studied through numerical modeling and field measurements. Ghost cavity cloud consists of several acoustically induced cavities which are formed due to the pressure drop caused by reflected pressure waves, i.e. ghost, from the sea surface.

The thesis is a collection of several independent papers organized in chapters together with an introductory part (chapter 1) which reviews the key concepts that are relevant as background and motivation for the work presented.

In chapter 2, A synthetic modeling scheme for simulation of acoustically induced cavitation in seismic air-gun arrays is developed. The growth and subsequent collapse of individual cavities around the array are modeled by bubble dynamic equations. The pressure fields generated by individual cavities are added to model the acoustic signal from the cavity cloud. To validate the modeling technique, the simulation results are compared to the field recorded data.

In chapter 3, using the numerical modeling scheme, high-frequency emissions caused by ghost cavitation for two different air-gun arrays are compared. The developed numerical scheme has the potential to evaluate air-gun arrays regarding the amount of high-frequency ghost cavitation acoustic signal.

In chapter 4, photographed ghost cavity cloud by a high-speed video camera in a field experiment are presented which provide an undebatable evidence of the phenomenon. Furthermore, the modeling scheme for the cavity cloud is further evaluated.

In chapter 5, sound velocity within the cavity cloud was investigated using a k-space pseudo-spectral numerical method. Presence of several small vapor cavities has potential to significantly drop the sound speed of water within the cavity cloud at frequencies below the resonance frequencies of the cavities. It is shown that if the sound velocity drops within the cavity cloud, though for a short time (8-10 ms), it affects the far-field acoustic pressure.

In the appendix, the effects of cavity collapses within the ghost cavity cloud on

the near-field hydrophones are simulated. In this paper, the model is tuned (calibrated) such that both the amplitude of the high-frequency modeled signal and its associated low-frequency part match the measurements.

Preface

This thesis is submitted to the Norwegian University of Science and Technology (NTNU) for partial fulfilment of the requirements for the degree of philosophiae doctor. This doctoral work has been performed at the Department of Geoscience and Petroleum, NTNU, Trondheim with Professor Martin Landrø as supervisor. The research was funded by the Research Centre for Arctic Petroleum Exploration (ARCEX).

Acknowledgements

My sincere gratitude goes to my supervisor, Prof. Martin Landrø, for great guidance, insightful discussions, and inspiring conversations. It has been an honor and a privilege to have the opportunity to conduct my PhD studies under his supervision. I hope I have learned from his deep academic insight, professional attitude, and nice human skills for future academic life.

I would like to acknowledge the Research Center for Arctic Petroleum Exploration (ARCEX) for financing my PhD studies. My special thank goes to Prof. Alfred Hanssen, the ARCEX director, for his support and encouragement. His positive and energetic attitude has made ARCEX a friendly and constructive environment. I would like to thank the administrative coordinator of ARCEX, Ellen Ingeborg Hætta, who always has been helpful and supportive. Furthermore, ROSE consortium is acknowledged for financial support. I thank Statoil ASA (Equinor) for publication travel grant.

I am grateful to the assessment committee members: Prof. Michele Pipan (University of Trieste, Italy), Prof. Tor Arne Johansen (University of Bergen, Norway), and Prof. Børge Arntsen (Norwegian University of Science and Technology, Norway). I am thankful to Dr. Marianne Helene Rasmussen, research professor in marine biology, at the University of Iceland, for the field work and discussions about the marine mammals' sound. I appreciate the former PhD candidate, Dr. Kjetil E. Haavik for sharing his knowledge on air-gun modeling.

I am thankful to the administrative staff at IGP for all the help and support. I would like to thank all my ARCEX friends, IGP friends, all PhDs, and Post-docs for their supports and the good moments I spent with them. I would like to thank my friend and former colleague Dr. Rasoul Khaledialidusti for all the time we spent. Thanks to my office mates (in an alphabetical order), Dr. Lucas Cantinelli Sevillano, Nur Suriani Mamat, and Xiaoqian Cheng who made the office a desirable place.

I would like to express my deepest thanks to my parents for their unconditional love, support and encouragement throughout life. I would also like to thank my sister and brother for their support and always being there for me. Last but not least, I thank my wife for her help and support during my PhD studies.

Babak Khodabandeloo,
Trondheim, Norway
August 2018

Contents

Abstract	i
Preface	iii
Acknowledgements	v
Contents	vii
1 Chapter 1: Introduction	1
1.1 Marine seismic surveys	2
1.2 Air-guns and air-gun arrays	2
1.3 High-frequency emission by seismic air-gun arrays – Ghost Cavitation	9
1.4 Impacts of sound on marine environment	11
1.4.1 Quantifying the magnitude of noise	12
1.4.2 Auditory weighting functions Sound	14
1.4.3 Weighted far-field energy spectrum of recorded full air- gun array.	19
1.4.4 Behavioral effects	22

1.5	Mitigation of air-gun noise impacts on the marine environment . . .	23
1.6	Alternative marine seismic sources	25
1.6.1	Air-guns with flexible bandwidth control (eSource)	25
1.6.2	Marine Vibrators (MVs)	25
1.6.3	Low Pressure Source and Tuned Pulse Source	26
1.6.4	Encoded source sequences	27
1.7	Basic acoustic source models	28
1.7.1	Acoustic impedance and radiation efficiency	28
1.7.2	Pulsating sphere	29
1.7.3	Vibrating baffled circular piston	30
1.8	K-space pseudo spectral method	32
1.9	Thesis structure	33
1.10	Contributions	35
2	Chapter 2: Acoustic generation of underwater cavities – comparing modeled and measured acoustic signals generated by seismic air gun arrays	37
2.1	Abstract	38
2.2	Introduction	38
2.2.1	Background	38
2.2.2	Acoustic waves and cavitation	40
2.2.3	Cavities in plasma due to an external electric field	41
2.3	The field experiment	42
2.4	Ghost cavitation signal modeling	44
2.4.1	Modeling the pressure drop caused by reflected air gun signals from the sea surface	46
2.4.2	Cavity collapse	47
2.4.3	Propagation of cavity signatures from source to receiver	53

2.5	Results	54
2.5.1	Model 1 - No interaction between cavities	55
2.5.2	Model 2 - With pressure interaction between cavities	55
2.6	Discussion and conclusions	59
2.7	Acknowledgment	60
3	Chapter 3: High frequency ghost cavitation – a comparison of two seismic air-gun arrays using numerical modelling	61
3.1	Abstract	61
3.2	Introduction	62
3.3	Ghost cavitation signal modelling	64
3.4	Two air-gun arrays configurations	66
3.5	Results	67
3.6	Discussion and conclusions	71
3.7	Acknowledgements	71
4	Chapter 4: Acoustically induced cavity cloud generated by air-gun arrays – comparing video recordings and acoustic data to modeling	73
4.1	Abstract	73
4.2	Introduction	74
4.3	The field experiment	77
4.3.1	High-frequency signal measurement	78
4.3.2	Field video recording	79
4.4	Modeling the ghost cavity cloud	81
4.5	Comparison of numerical modeling and field measurements	85
4.6	Discussion	89
4.7	Conclusion	90
4.8	Appendix:Ghost cavitation modeling	90

4.9	Acknowledgment	93
5	Chapter 5: Characterizing acoustic properties of cavity cloud as a time-dependent effective medium surrounding an air-gun array	95
5.1	Summary	95
5.2	Introduction	96
5.3	Visualizing ghost cavity cloud	98
5.4	Theory: speed of sound in gas/vapor mixture	99
5.5	Field experiment	102
5.6	Numerical implementation of wave propagation in the time-dependent medium – k-wave simulations	104
5.6.1	Governing equations and K-wave implementation	104
5.6.2	Effects of layered sea-floor on the recorded pressure	108
5.6.3	Effects of local time-dependent medium around the source array	110
5.7	Results	112
5.7.1	Cavity cloud as a fixed ellipsoid	112
5.7.2	Cavity cloud modeling based on modeled pressure values	117
5.7.3	Including ghost cavitation signal in the modeling	120
5.8	Discussion	121
5.9	Conclusion	124
5.10	Acknowledgment	125
6	Concluding Remarks	127
A	Appendix A: Effects of Ghost Cavitation Cloud on Near-field Hydrophones Measurements in the Seismic Air Gun Arrays	131
A.1	Abstract	131

A.2	Introduction	132
A.3	Spatial and temporal distribution of pressure drops	133
A.4	Cavity collapse simulations	133
A.5	Comparison of simulated and field measured signals	134
A.6	Nearfield hydrophone signals simulation	136
A.7	Conclusions	137
A.8	Acknowledgements	137

References**139**

Chapter 1

Introduction

When marine seismic air-gun arrays are used as sources in marine seismic acquisition, ghost cavitation is assumed to be the underlying mechanism behind most of the high-frequency (>10 kHz) energy in the acoustic signal. It consists of generation and collapse of several cavities induced by the pressure drop due to the reflected pressure waves – so-called ghost reflections – from the sea surface. In this PhD project, a synthetic modeling scheme for modeling the cavity cloud and the corresponding acoustic signal is presented. Furthermore, various aspects of ghost cavitation and possible impact(s) on the source signature are studied.

The primary motivation for studying high-frequency acoustic emissions by marine seismic sources is environmental concerns. Such high-frequencies do not benefit seismic reflection imaging and are weak compared to the seismic band energy. However, they might impact marine fauna, especially the ones with sensitive high-frequency hearing. A related example for this concern is probably the environmental effects of ship traffic noise. Marine vessels radiate most energies at low-frequencies (< 250 Hz) and hence until recently the effects of ship noise on marine mammals with poor low-frequency hearing were dismissed. In recent studies on captive and free-ranging porpoises, it was observed that the low-level high-frequency acoustic energy radiated by marine vessels induce noticeable behavioral responses. Therefore, there are increasing concerns regarding the apparently low-level high-frequency acoustic energy on porpoises and small toothed whales which have sensitive high-frequency hearing. In fact, when evaluating the impact of underwater noise on a marine animal, it is essential to take into account the hearing curve of that animal. Frequency weighting of the noise serves this purpose by de-emphasizing frequencies where the animal has less sensitive hearing.

In addition to the potential environmental impacts, ghost cavitation might affect seismic imaging by altering the array signature. For example, the generated signal by several collapsing cavities can contain some low-frequency components in the seismic band. Furthermore, the presence of cavities might distort the array signature by changing the acoustic properties of the medium surrounding the array.

This thesis is a collection of several independent papers organized in chapters. The current chapter provides an introduction to some of the key concepts that are relevant as background and motivation for the work presented.

1.1 Marine seismic surveys

Marine seismic surveys are performed to delineate geological structure and usually to find hydrocarbon resources below the seabed. An acoustic source is required to emit the acoustic energy. The acoustic waves propagate from the source and travel through the subsurface layers where the waves are reflected at interfaces between various geological layers. The reflected waves are recorded by seismic receivers such as geophones, hydrophones or accelerometers. Underground geological strata are determined by processing the recorded signals. The common approach is to use towed acoustic sources in the water layer which means some acoustic waves are radiated into the surrounding water which might impact marine animals. Air-gun arrays are the dominant marine seismic source thanks to many attractive features they provide for seismic imaging.

1.2 Air-guns and air-gun arrays

Air-gun arrays have been the most common and efficient marine seismic source (Duren, 1988; Barger and Hamblen, 1980) and still are (Watson, et al. 2016; Gisiner, 2016). An array consists of several air-guns with different air-chamber volumes. An air-gun is a mechanical device that stores high-pressure air in a reservoir and releases it into the surrounding water within a short time through small ports. By releasing the compressed air, part of its energy is converted to the acoustic waves. Expansion and contraction of the bubble, which formed by releasing high-pressure air into the water, generates the acoustic pressure wave which is called air-gun source signature (Dragoset, 2000; Caldwell and Dragoset, 2000). A pressure signature 100m below a typical 100 in³ single air-gun fired at 5 m depth is modeled by NUCLEUSTM and shown in Figure 1.1(a). The first peak of source signature is direct arrival and corresponds roughly to the opening

of air-gun ports. The first trough after the direct arrival is surface ghost and is the reflection of direct arrival from water-air interface. Since the reflection coefficient of the water-air boundary is negative, source ghost and direct arrival have opposite polarity. The subsequent smaller peaks after the main peak are called bubble pulses and correspond to expansion and contraction of air bubble generated by the fired air-gun. The air-gun source signature depends on air-chamber volume, firing pressure, surrounding pressure, and port shapes. Volume of air-gun chambers are usually between 30 in³ to 800 in³.

It is convenient to decompose the measured pressure signature as a combination of two sources: a monopole located at the gun position that accounts for the direct arrival and an image source for the reflected pressure from the sea surface as shown schematically in Figure 1.1(b). This decomposition enables us to determine the pressure at any location as a linear combination of the signatures from the source and its image (ghost source). This is the concept of notional source signature (Ziolkowski et al. 1982). The notional source signature of an air-gun is its net pressure output including the interaction effects of other sources such as effects from the ghost (image) source or the other firing air-guns in the array (Tabti et al, 2017). The notional source signature and the ghost are shown by blue and red, respectively. Given the location of the air-gun and the receiver (for example see Figure 1.1b), the notional source signature can be estimated from the recorded pressure as:

$$p(t) = \frac{1}{r}p'(t - \frac{r}{c}) + \frac{R}{r_g}p'(t - \frac{r_g}{c}) \quad (1.1)$$

Where $p(t)$ is the recorded pressure by the hydrophone, $p'(t)$ is the air-gun's notional source signature, r is the source-receiver distance, r_g is the distance between ghost (or image) source and the hydrophone, c is the water phase speed, and R is the reflection coefficient at the sea surface which is approximately -0.9994 and is usually selected equal to -1.

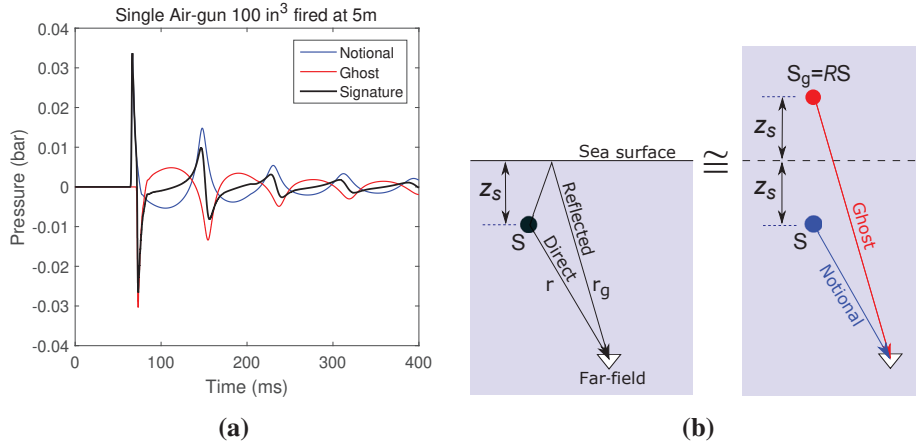


Figure 1.1: Notional source signature (blue), reflected ghost signal (red) and the air-gun signature (black) of a 100-in³ single air-gun fired 5m below the sea-surface modeled by NUCLEUSTM (PGS) 100 m below the air-gun.

The peak amplitude of an air-gun source signature is linearly proportional to the firing pressure and proportional to the cube root of its volume (Dragoet, 1990). For example, operating under the same air pressure, the acoustic amplitude of a 160 in³ is only twice that of an air-gun with a 20 in³ volume chamber. Therefore, for a fixed air volume capacity, it is more efficient to partition the air among many smaller air-guns than few large air-guns.

Rarely one single air-gun is used as an acoustic source for marine seismic imaging. Instead, several (typically 12-48) air-guns with different volumes are arranged together in an array (Dragoet, 2000). Using the array concept is an efficient way to increase the source strength. The other advantage is to direct more energy downward and to reduce the lateral directivity. In addition, by simultaneous firing of several air-guns with different volumes, their direct arrivals add constructively while the bubble pulses add incoherently and cancel each other which results in a cleaner pulse shape signature. Air-gun array strength is (1) linearly proportional to the number of air-guns in the array; (2) roughly proportional to the cube root of array volume; (3) and almost linearly proportional to the operating pressure of array (Dragoet, W.H., 1990; Landrø and Amundsen, 2010). Notional source signature of air-guns in an array can be estimated using equation 1.2 as suggested by Ziolkowski (1982). To estimate the notional source signatures, this equation requires at least the same number of independent pressure measurements as the number of air-guns in the array by hydrophones placed close to the air-guns in the array. Having N air-guns, the i^{th} near-field measurement denoted by $h_i(t)$ can be

expressed by a linear superposition of air-gun notional source signatures represented by p'_j as represented by equation 1.2 (Ziolkowski, 1982; Parkes et al., 1984). Subsequently, notional source signatures can be estimated by solving a system of linear equations.

$$h_i(t) = \sum_{j=1}^N \frac{1}{r_{ij}} p'_j \left(t - \frac{r_{ij}}{c} \right) + R \sum_{j=1}^N \frac{1}{r_{g_{ij}}} p'_j \left(t - \frac{r_{g_{ij}}}{c} \right) \quad (1.2)$$

In this formula, r_{ij} and $r_{g_{ij}}$ represent the distance between the i^{th} near-field hydrophone and j^{th} air-gun and its ghost (image), respectively. The notional source signature of air-guns with different air-chamber volumes being fired individually and in an array configuration are shown in Figure 1.2. The acoustic pressure from other air-guns interact with the output acoustic pressure from an air-gun.

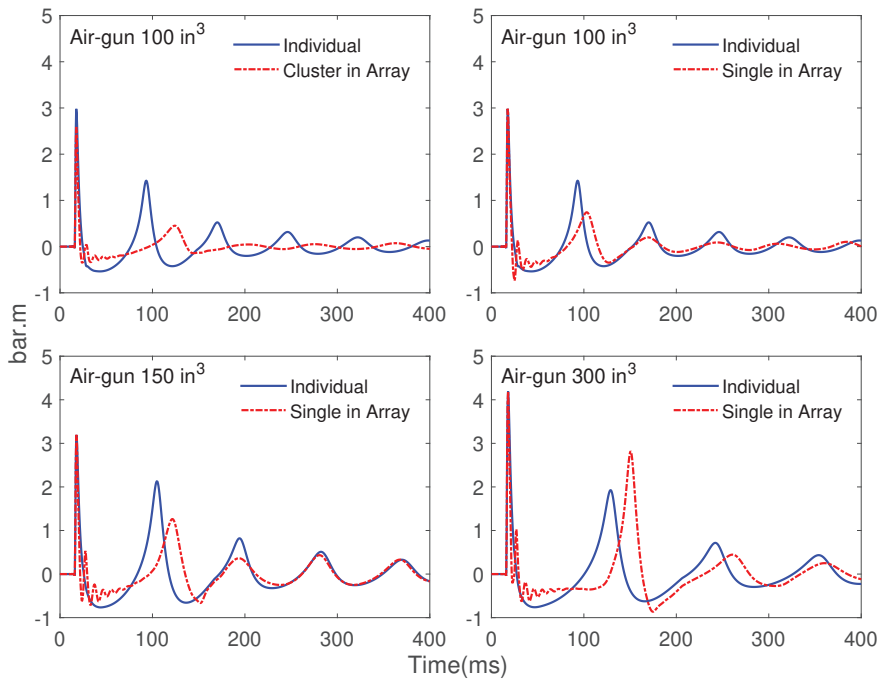


Figure 1.2: Notional source signature of an air-gun being used single and in an array modeled by NUCLEUSTM. The array configuration was same as S_1 in Figure 1.3. Top left is the 100 in³ cluster in the side sub-array. Top right is the single 100 in³ in the middle sub-array next to 150 in³. Bottom left is 150 in³ in the middle sub-array. Bottom right is the single 300 in³ in the middle sub-array.

As example of various array configurations, four different air-gun arrays are shown in Figure 1.3. Arrays S_1 and S_3 are the configurations used in the field experiments presented in the subsequent chapters and S_2 is used for numerical modeling in Chapter 3. Arrays S_1 and S_2 consist of three sub-arrays, array S_3 has two sub-arrays and S_4 is the center sub-array of S_1 .

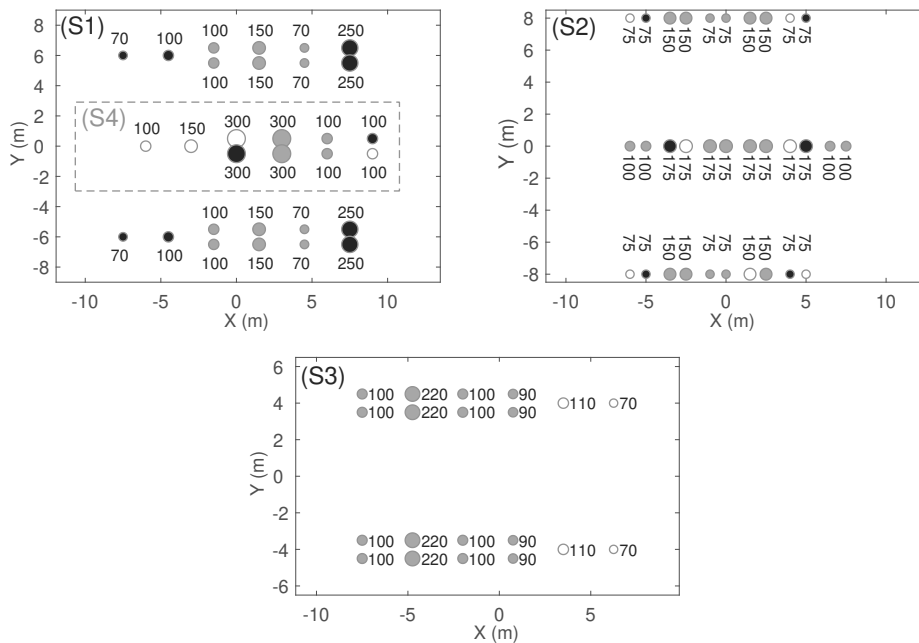


Figure 1.3: Four different array configurations labeled by S_1 to S_4 . Each air-gun is shown by a circle and the number beside it represents its air-volume chamber. White, gray, and black circles represent single, cluster, and inactive air-guns, respectively. S_1 and S_2 include three sub-arrays. S_3 has two sub-arrays and S_4 has one sub-array which is similar to the center sub-array of S_1 .

Peak pressure of these four arrays and a single 300in^3 air-gun are extracted from the modeled source signatures by NUCLEUSTM at different angles for cross-line and in-line directions and are shown in the left of Figure 1.4, top and bottom, respectively. Their normalized counterparts are plotted beside them in the right side. The radial values are pressure (bar) at 1 meter. The peak pressures are extracted

from pressure signatures in the far-field estimated at different angles at the distance of 1000 m from the source. They are scaled by compensating for the geometrical spreading to obtain their values at 1m (i.e. multiplying with 1000).

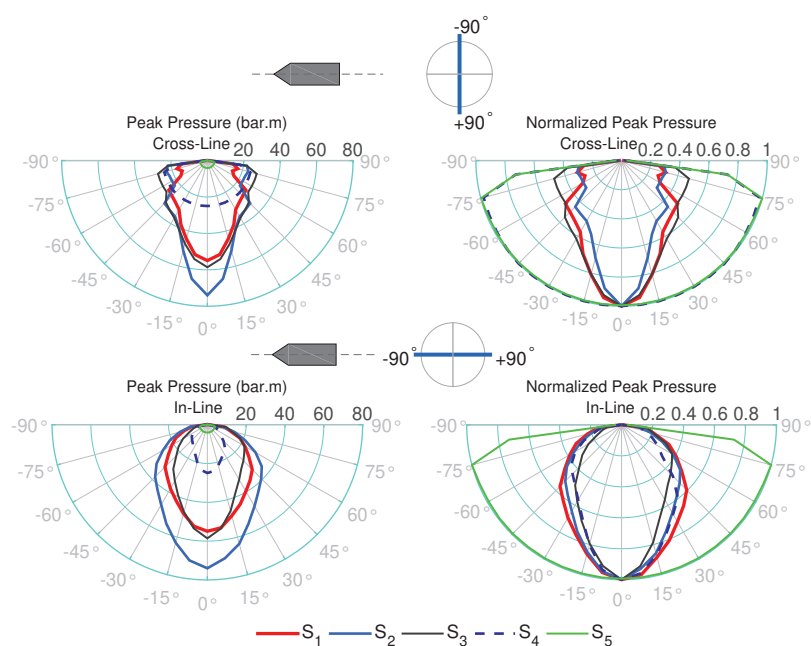
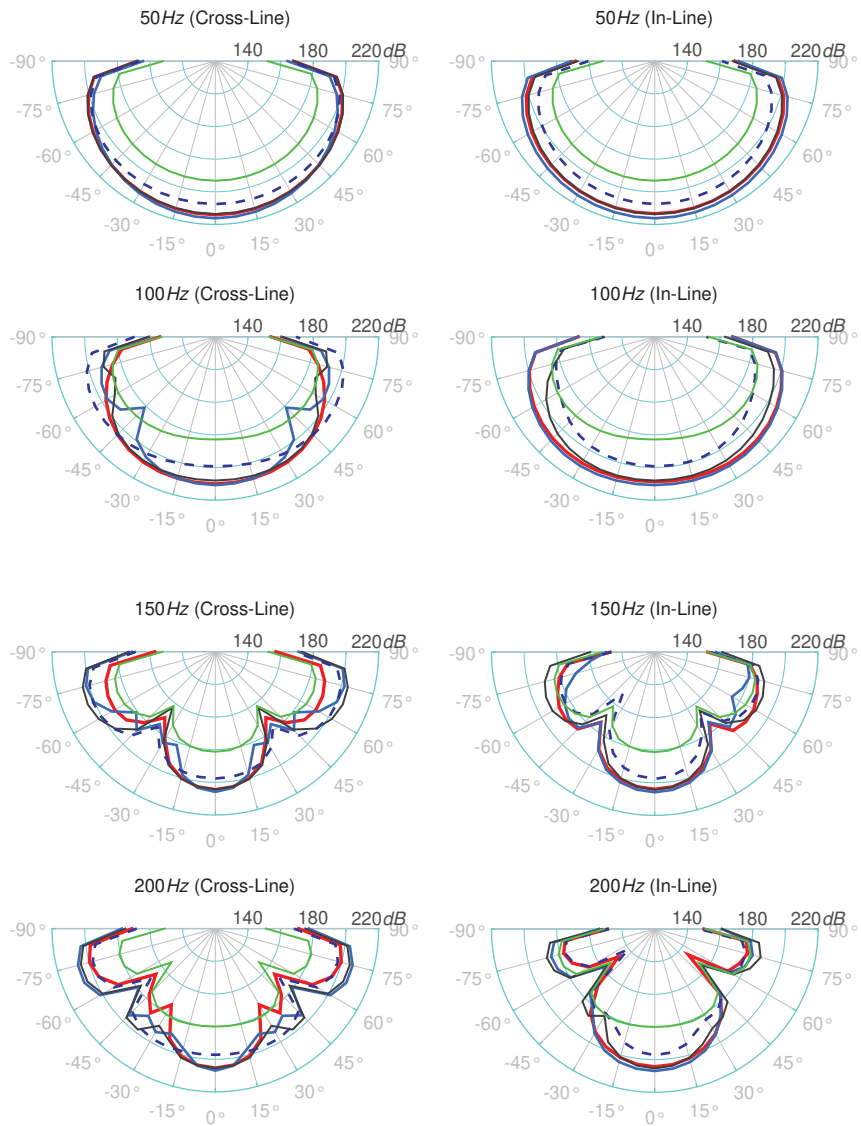


Figure 1.4: Peak pressures at different angles in two directions: Cross-line (top) and In-line (bottom) as indicated in the figure. Peak pressure pattern for four arrays (shown in Figure 1.3) together with a single air-gun (S_5) with 300 in^3 .

It is observed that the magnitude of the peak pressure is maximum at zero angle (i.e. downward) and it is reduced in the lateral direction for the full arrays in both cross-line and in-line directions. However, the center array, S_4 , is directional in the in-line direction but it is same as single air-gun in the cross-line direction.

It is instructive to look at the energy radiation pattern of the above-mentioned sources at different frequencies. In Figure 1.5, the radiated energy at six different frequencies, i.e. 50, 100, 150, 200, 250, and 300 Hz, as a function of angle are plotted in cross-line and in-line directions.



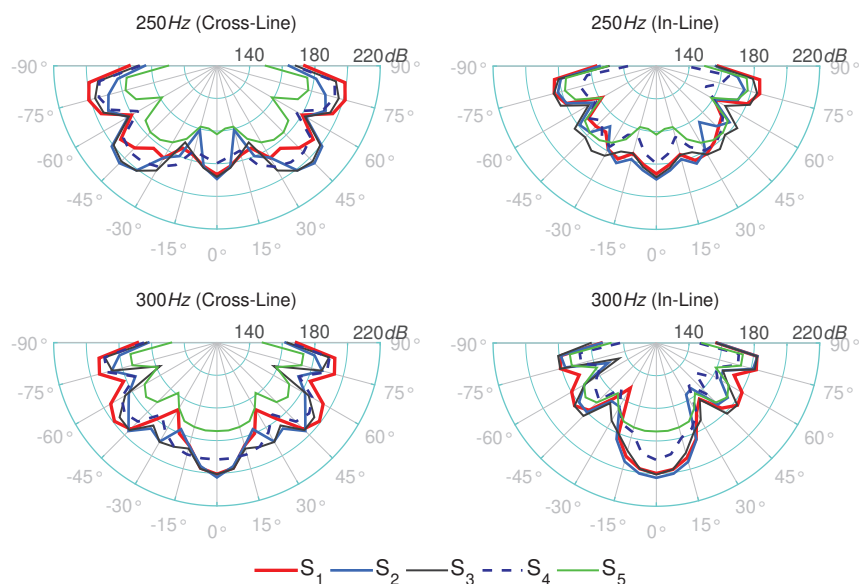


Figure 1.5: Energy radiation pattern (dB rel $1 \mu\text{Pa}$) at six different frequencies for cross-line and in-line directions shown in the left and right side, respectively.

It is seen that at 50 Hz, for both cross-line and in-line directions, maximum energy is radiated at zero angle (downwards), then gradually and smoothly decreases going to the horizontal direction. The energy radiation pattern at 100 Hz is same as the radiation pattern at 50 Hz for all sources except for S_2 in the cross-line direction which shows 30 dB decrease at $\pm 45^\circ$. At 150 and 200 Hz, there are more energies radiated in the zero angle for in-line direction. While in the cross-line direction there are almost equal amount of energies radiated in zero and around $\pm 70^\circ$ for all sources except S_1 . At 250 Hz, almost all five sources radiate more energy lateral than downward in the cross-line direction. At 300 Hz, for the in-line direction the arrays radiate most of the energy downward, but they radiate almost equally at 0 and $\pm 45^\circ$.

1.3 High-frequency emission by seismic air-gun arrays – Ghost Cavitation

In a field experiment, acoustic pressure waves were recorded using a broad-band hydrophone (bandwidth=125 kHz) located on the sea-bed at a depth of around 60m. Energy spectrum of the recorded signal for three different source configur-

ations, i.e. a single air-gun, a single array (S₄ in Figure 1.3), and a full array with three sub-arrays (S₁ in Figure 1.3), are plotted in Figure 1.6. The energy spectrum of ambient, or background, noise is estimated from part of the signal before the source was fired and plotted in the same figure.

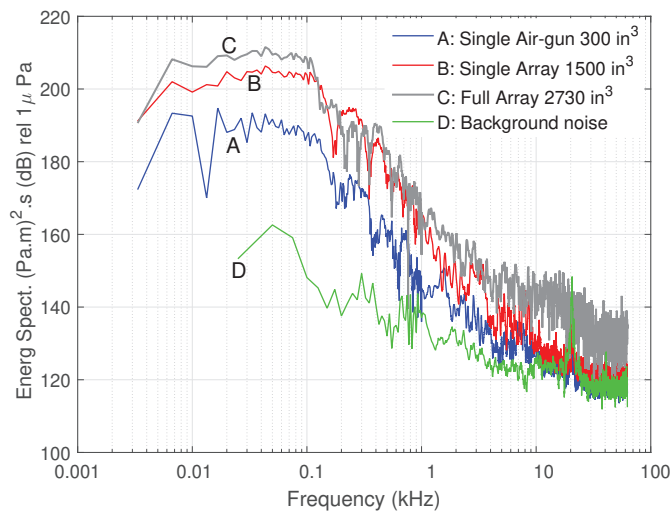


Figure 1.6: Energy spectrum densities (ESDs) of signals generated by different sources and recorded by a broad-band hydrophone (bandwidth=125 kHz). The sources were a single air-gun 300 in³, single array 1500 in³, and a full air-gun array 2730 in³. ESD of background noise is plotted with green line.

In the seismic frequency range ($< \sim 100$ Hz), the acoustic signal is increased by increasing the strength of the source, as expected. However, in the high-frequency range (> 10 kHz) the full array generates much stronger energy compared to the single air-gun and single array which are almost in the same level as the background noise. The observed peak at 20 kHz in the background noise is due to the active echosounder on the shooting vessel. The recorded time signal from the full array is plotted by blue in the first row in Figure 1.7. Its band-pass filtered (5-10 kHz) and 10kHz high pass filtered signals are plotted after amplifying by a factor of 10.

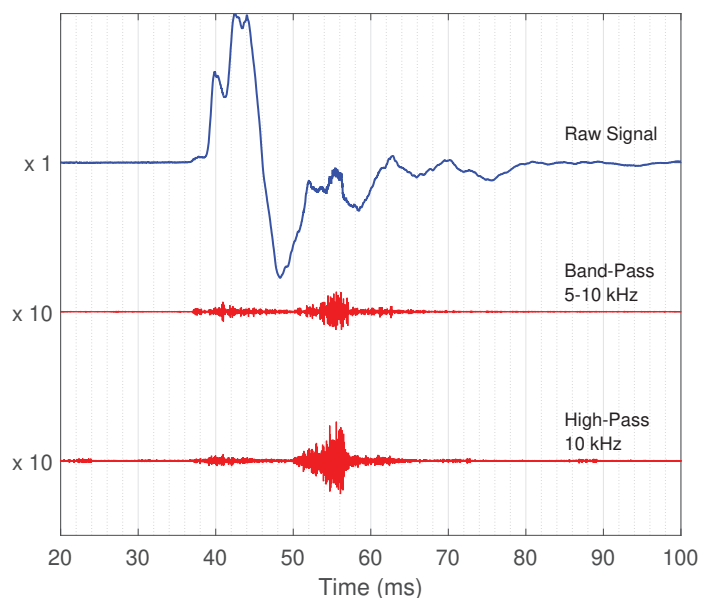


Figure 1.7: recorded signal from a full air-gun array and its frequency contents in 5-10 kHz and >10 kHz bands are plotted after amplification by a factor of 10.

It is seen that the majority of high-frequency energies appear with around 8 ms time delay after the main peak (direct arrival). This time delay roughly corresponds to the ghost pressure wave to reach 2-3 meters above the mid-array. Landrø et al. (2011) hypothesized that these high-frequencies are due to the cavitation phenomena and called it ghost cavitation. That is the reflected pressure waves from the sea surface (i.e. ghost) drop the hydrostatic pressure below the water vapor pressure which can induce cavitation.

1.4 Impacts of sound on marine environment

Hearing is the primary sense for most marine mammals to obtain information about surrounding underwater environment where sound travels much more efficient than light (Mooney et al., 2012). This is especially true for cetaceans and they have some of the most sensitive, sophisticated and developed hearing systems of all mammals for audio processing (Mooney et al., 2012; NRC, 2003). They produce and receive sound over a broad range of frequencies for several purposes such as foraging, communication, social interaction, orientation, predator

avoidance (Wright et al. 2007). Anthropogenic noise introduced into the marine environment has the potential to influence many of these activities directly by impacting the animals' hearing system or masking the signals as well as indirectly by affecting the prays (Richardson et al., 1995; Nowacek et al., 2007). Possible impacts of anthropogenic noise on marine mammals are categorized into four zones, in the order of increasing severity, as: (1) Zone of audibility is the area within which the sound is audible to the animal (2) Zone of responsiveness (or behavioral disturbance), (3) Zone of masking where noise is sufficiently strong to interfere with detection of other sounds, (4) Zone of injury or hearing loss is the region where the received sound pressure levels are so high that it might cause temporary or permanent threshold shift (TTS or PTS) in animal's hearing (Nowacek et al., 2007; Richardson et al., 1995).

To facilitate the study of acoustic effects on cetaceans, they are divided into three functional hearing groups based on their measured or estimated hearing characteristics (Southall et al., 2007):

- (1) Low-frequency (LF) cetacean which include all the mysticetes (or baleen whales).
- (2) Mid-frequency (MF) cetaceans include most odontocetes (toothed whales) e.g. delphinid species, killer whales, beaked whales, bottlenose whales, and sperm whales.
- (3) High-frequency (HF) cetaceans include the porpoises, river dolphins, and Cephalorhynchus.

All the species within a group are assumed to have the same auditory sensitivity and susceptibility to noise (Finneran and Jenkins, 2012).

1.4.1 Quantifying the magnitude of noise

One relevant question regarding underwater acoustic noise is that which sound metric(s) is appropriate to quantify the magnitude of the noise. In addition, since pulses and non-pulse sounds have different potential impacts on the hearing of marine mammals, their distinction is important (Southall et al., 2007). For example, underwater acoustic pressure is variously reported in terms of peak pressure, peak-peak, root mean square (rms) and peak-equivalent of rms. The magnitude of a sound pressure level (SPL) underwater is often expressed as a dB scale relative to 1 μ Pa, the reference pressure. Sound pressure of a non-pulse (continuous) signal is usually expressed in terms of rms metrics, while the sound pressure for a pulse (transient) signal is expressed in terms of its peak pressure. Sound pressure level (SPL) is a tool to characterize the amplitude of an acoustic

wave. It is defined as (NRC, 2003):

$$SPL = 20 \log_{10} \left(\frac{A_p}{p_{ref}} \right) \quad (1.3)$$

Where A_p can be peak pressure amplitude or rms amplitude and p_{ref} is the reference pressure (1 μ Pa for water). The SPL of root mean squared pressure (rms) of a signal is given by:

$$SPL_{rms} = 10 \log_{10} \left(\frac{1}{T} \int_0^T \frac{p^2(t) dt}{p_{ref}^2} \right) \quad (1.4)$$

For aperiodic signals, the difference between peak-peak pressure and rms can often be 15 dB and more (Madsen, 2005). In addition, the rms level varies by changing the integration time duration. Accordingly, to get meaningful results, the selection of duration is crucial. Hearing studies of mammals, both marine and terrestrial, indicate that the mammalian ear integrates energy over certain time duration which is called hearing integration time (Kastelein et al., 2010). Detectability and auditory threshold of a short duration acoustic signal improve with increasing the signal duration up to the hearing integration time. The measured hearing integration times for few marine mammals indicate that they are similar to those of terrestrial ones and are a few hundred milliseconds (Erbe et al., 2016). Time window of 200 ms is commonly used for computing rms SPLs (Breitzke et al., 2010). Increasing the signal duration beyond the integration time does not further improve the animal's ability to hear the given signal.

Impulsive acoustic waves can include very high-peak sound pressure levels while containing a very small amount of energy. Consequently, when assessing the acoustic impact of a sound pulse, it is both the peak pressure and the energy flux that should be taken into the account (Madsen, 2005; Ward, 1997). The energy of signal within specified time duration, T , is defined by time integral of squared pressure over the time interval (Southall et al, 2007):

$$E(T) = \int_0^T p^2(t) dt \quad (1.5)$$

Sound exposure level (SEL) is a measure of energy that includes not only the received level, but also the duration of exposure. The sound exposure level for the time duration T , is approximated by (Southall et al, 2007):

$$SEL = 10 \log_{10} \left(\int_0^T \frac{p^2(t) dt}{p_{ref}^2} \right) \quad (1.6)$$

SEL can be calculated for a single impulse of noise or multiple impulses to generate cumulative sound exposure level.

1.4.2 Auditory weighting functions Sound

Magnitude, frequency, and time duration are the physical properties of acoustic waves or sound. Experimental results indicate that hearing in marine mammals is not equally sensitive to the sound magnitude at all frequencies. Therefore, guidelines that are based on exposure limits defined by received SPL regardless of frequency, duration, and temporal pattern of sound and have ignored hearing sensitivities of different marine mammals are inappropriate. Auditory weighting functions are mathematical functions to include the frequency-dependent features of auditory sensitivity to better predict the auditory effects of man-made sound on marine mammals. Weighting functions are used to weight frequency ranges to de-emphasize where animals are less sensitive (Houser et al. 2017; Tougaard and Dahne, 2017). Weighting functions enable us to generate a single weighted threshold value by combining the weighted noise levels at each frequency. Without weighting functions there would be a large number of individual thresholds corresponding to each frequency (Finneran and Jenkins, 2012).

To derive weighting functions for marine mammals, the most appropriate method is to relate the effect of interest to the level and frequency of noise for each animal or species. Such effects have been permanent or temporarily threshold shift (PTS/TTS) in the hearing of marine mammals. However weighting functions are not applied to predict behavioral disturbances, annoyance, or masking effects of noise (Houser et al. 2017). One of the sound metrics that has influence on the development of marine mammals weighting functions is marine mammals' audiogram which is hearing threshold as a function of frequency (Nedwell et al., 2007). Most marine mammals' audiograms are obtained using psychophysical (behavioral) procedures. The other flourishing method to obtain marine mammals hearing thresholds is neurophysiological measures based on auditory evoked potentials (AEP). AEP is a relatively rapid method to test the hearing sensitivity of animal by measuring generated small voltage by neurons in the auditory system in response to sound (Mooney et al., 2012). Despite the pattern of frequency dependent hearing sensitivity agrees between these two methods, the absolute sensitivity is different (Yuen et al., 2005; Nachtigall et al., 2005; Cook et al., 2006). An audiogram provides the minimum level of acoustic stimuli at each frequency that is barely

audible (Branstetter et al., 2017). Most likely a sound should be more intense than threshold level to be perceived loud and adversely affect the animal.

The other sound metric is called equal loudness contours which represents the sound pressure level of sound at each frequency that are judged equally loud (Finneran and Schlundt, 2011). Using behavioral technique, equal loudness contours were measured for a bottlenose dolphin at three different levels 90, 105, and 115 dB (re $1\mu\text{Pa}$ at 10 kHz). It is observed that the loudness curves in dolphin flatten at higher sound levels (Finneran and Schlundt, 2011). It is reported that it took 9 months to train a bottlenose dolphin and 15 additional months to acquire these contours. Therefore, instead of daunting task of measuring equal loudness contours directly, the alternative was to measure reaction time of animal to the acoustic stimuli at different SPLs to estimate loudness. Connecting the equal reaction times in response to acoustic waves with various frequency and SPLs, equal latency contours are obtained (Mulsow et al., 2015; Wensveen et al., 2014). At low sound levels near the threshold, the equal latency curves are similar to the audiograms. The major limitation of equal latency contours is that above a certain sound level, the reaction times do not decrease as the sound level increases which limit the understanding of perceived loudness of higher SPLs.

Noise induced temporary threshold shift (TTS) curves are the other metrics used to develop audiometric weighting functions for marine mammals. TTS contours provide the required sound exposure level (SEL) to induce a certain amount of TTS in different frequencies. Several experiments are conducted to study the effects of SPL, frequency, duration, and temporal pattern of noise on TTS (Finneran, 2015). TTS due to being exposed to various SPLs and durations was investigated and it was revealed that there is a correlation between TTS and SEL (Popov et al., 2014; Kastelein et al., 2012; Mooney et al., 2009). TTS accumulates over time, but for the exposure with the same SEL, shorter duration or intermittent exposure produce less TTS than longer duration or continuous exposure. This is probably due to the recovery of hearing threshold shift occurred between the exposures.

Southall et al. (2007) developed the first widely applied marine mammal weighting functions called M-weighting functions. At that time there existed no equal loudness or equal latency contours for marine mammals and it was reasonable to use species' hearing sensitivities as weighting functions. But the existing audiograms for odontocetes had a much steeper reduction at low-frequencies compared to the TTS data of dolphin and beluga which was somehow flat between 3 and 20 kHz. As a result, M-weighting functions were developed based on the shape of human C-weighting functions which matches human sensitivity to louder sounds than A-weighting function. M-weighting functions for LF, MF, and HF cetaceans are given in Southall et al. (2007) and plotted in Figure 1.8 by solid lines. From exper-

iments on dolphin (Finneran, 2010; Finneran and Schlundt, 2009), it was observed that above 3kHz the dolphin susceptibility to TTS increases (which means TTS onset is lower) while the M-weighting function for MF cetacean is flat between 3 to 20 kHz. After the equal loudness curves were obtained for a bottlenose dolphin in 2011 (Finneran and Schlundt, 2011), new auditory weighting functions (EQL weighting) were presented based on equal loudness contours passing through 90, 105, and 115 dB re 1 μ Pa at 10 kHz. The EQL weighting function based on the 90 dB (re μ Pa) provides the best fit to the susceptibility data and are plotted after normalizing at 3 kHz in Figure 1.8 by dashed blue. The curves for LF and HF cetaceans are obtained by extrapolation (Finneran and Jenkins, 2012).

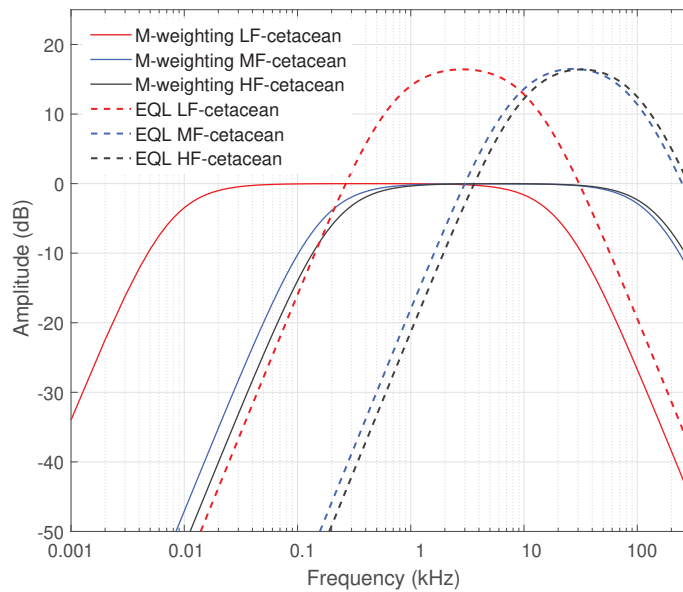


Figure 1.8: M-weighting and EQL based weighting functions for LF, MF, and HF cetaceans (See (Finneran and Jenkins, 2012)).

M-weighting has a flat shape over a broad frequency range with tapering off at low and high frequencies. A more restrictive weighting system was introduced by the National Oceans and Atmosphere Administration (NOAA) guidance (National Marine Fisheries Service, 2016). Audiogram-weighting or NOAA-weighting functions resemble inverted audiograms and are plotted in (Figure 1.9) for LF, MF, and HF cetacean groups.

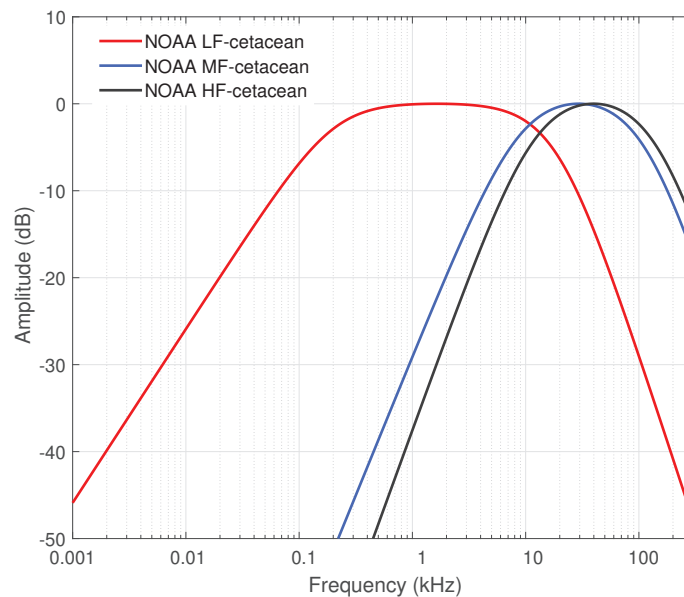


Figure 1.9: NOAA-weighting or Audiogram-weighting functions for LF, MF, and HF cetaceans (See (National Marine Fisheries Service. 2016)).

An intermediate weighting system is the Navy marine mammal weighting functions Type II (Houser et al., 2017; Finneran and Jenkins, 2012) and are plotted in Figure 1.10 for three functional hearing groups. Navy weighting Type II functions utilize features of both M-weighting and EQL-weighting functions; they have a broad weighting with emphasis on the best hearing frequency range. The accuracy of EQL weighting functions for MF cetaceans is unknown at lower frequencies. The reason is the lack of TTS data for MF cetaceans below 3kHz and equal loudness data are not available below 2.5 kHz 2011 (Finneran and Schlundt, 2011). Therefore, the Navy Type II weightings are based on M-weighting functions in the low-frequency range and they match the EQL weighting functions in the higher frequencies to accommodate the susceptibility of listener which indicate the listener's sensitivity to noise.

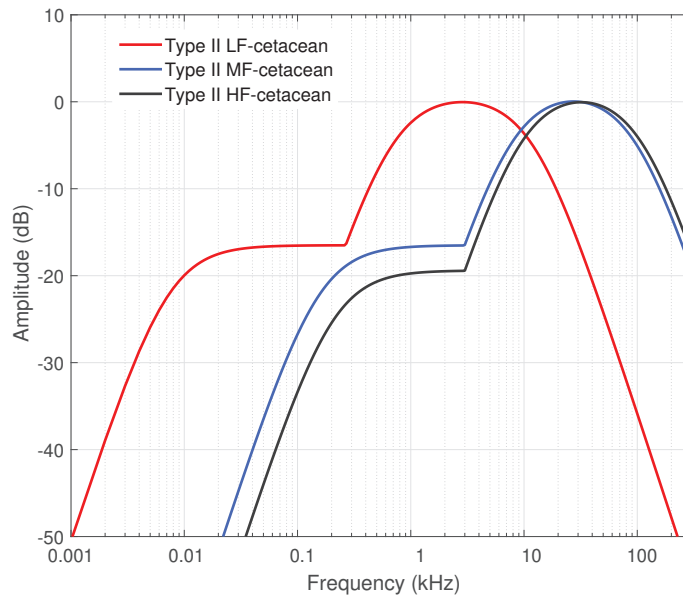


Figure 1.10: Navy weighting functions Type II for low-frequency (LF), mid-frequency (MF), and high-frequency (HF) cetaceans (Finneran and Jenkins, 2012).

Acoustic sources can induce physiological and behavioral effects on marine mammals. Physiological effects due to explosive sources are not limited to TTS or PTS, but also include tissue damage. To predict the auditory effects (TTS and PTS) of impulsive sounds, using weighted SEL threshold is appropriate (Finneran and Jenkins, 2012). For MF cetaceans, the SEL-based TTS onset threshold is 172 dB re $1 \mu\text{Pa}^2\cdot\text{s}$ which is selected according to the available TTS data from a bluga exposed to impulsive acoustic waves generated by a seismic water-gun (Finneran et al., 2002). Since such data is not available for LF cetacean, the TTS threshold for MF cetaceans is used. For HF cetaceans, the SEL-based TTS onset threshold is 146 dB re $1 \mu\text{Pa}^2\cdot\text{s}$ based on TTS data from a harbor porpoise exposed to underwater impulsive sound from a seismic air-gun (Lucke et al., 2009). The SEL-based TTS exposure functions are plotted in Figure 1.11. It is worth emphasizing that the study of noise effects on cetaceans is challenging because they are pelagic animals and it is difficult and costly to keep them in captivity (Mooney et al., 2012).

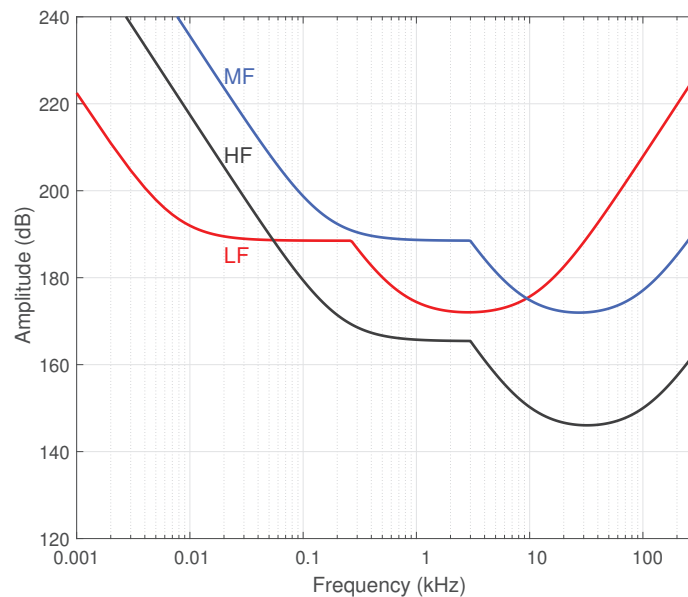


Figure 1.11: Navy type II TTS exposure function for impulsive noise (Finneran and Jenkins, 2012). Low-frequency (LF), Mid-frequency (MF), and High-frequency (HF) cetaceans.

1.4.3 Weighted far-field energy spectrum of recorded full air-gun array.

Different weighting functions presented above are applied to the energy spectrum of the acoustic signal generated by an air-gun array (S_1 in Figure 1.3) and recorded by a broad-band hydrophone. The weighted spectrums for three hearing cetacean groups, i.e. LF, MF, and HF, are plotted together with unweighted energy spectrum of the signal and the background noise in Figures 1.12, 1.13, and 1.14, respectively.

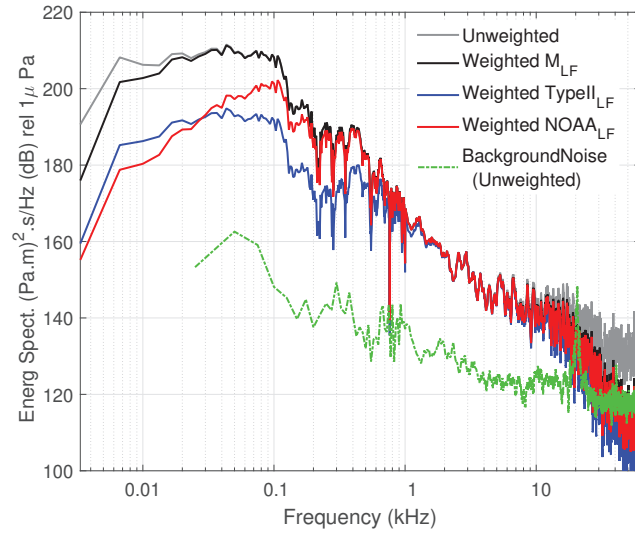


Figure 1.12: Recorded energy spectrum of the air-gun array by a broad-band hydrophone without weighting and with different weighting functions for low-frequency (LF) cetacean group.

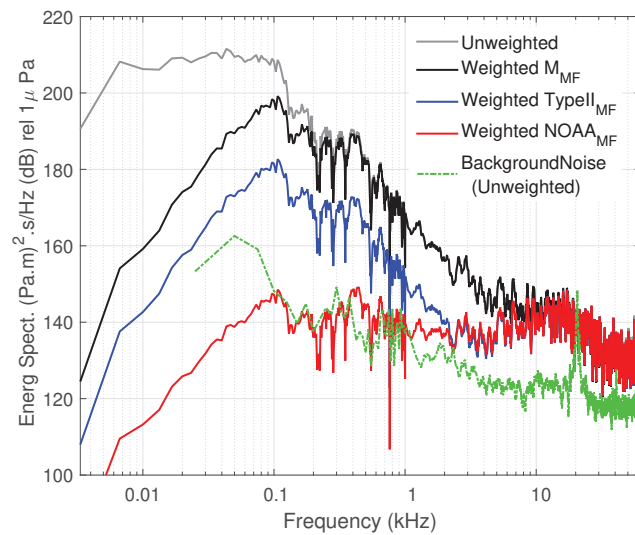


Figure 1.13: Recorded energy spectrum of the air-gun array by a broad-band hydrophone without weighting and with different weighting functions for mid-frequency (MF) cetacean group.

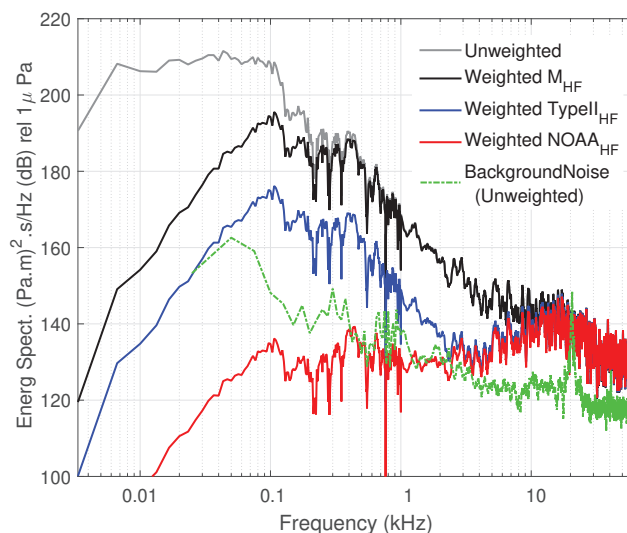


Figure 1.14: Recorded energy spectrum of the air-gun array by a broad-band hydrophone without weighting and with different weighting functions for high-frequency (HF) cetacean group.

For LF cetaceans, the low frequencies are dominant in all the weighted and unweighted Energy spectrum densities (ESDs) (see Figure 1.12). For MF cetaceans, as shown in Figure 1.13, the high frequencies become almost as important as low-frequencies for NOAA-weighted energy spectrum. For HF cetaceans as shown in Figure 1.14, high frequencies become dominant with NOAA weighting functions. Furthermore, the weighted ESD by Type II function is almost equally strong above the unweighted background noise level in both low and high frequency ranges.

The energy spectrums shown in Figure 1.6 are plotted together with the Navy type II TTS exposure functions for impulsive noise in Figure 1.15. It is observed that for the given array the generated high frequencies are below the TTS curves for all three cetacean groups and hence TTS occurrence is unlikely based on Navy type II exposure criteria. However, it should be noticed that the energy spectrums are given for one shot and if the animal is exposed to several shots it might impact animal's hearing threshold because SEL is the accumulated exposure level. Furthermore, the noise impact is not limited to TTS. Lower levels of noise have potential to cause other effects such as behavioral disturbances.

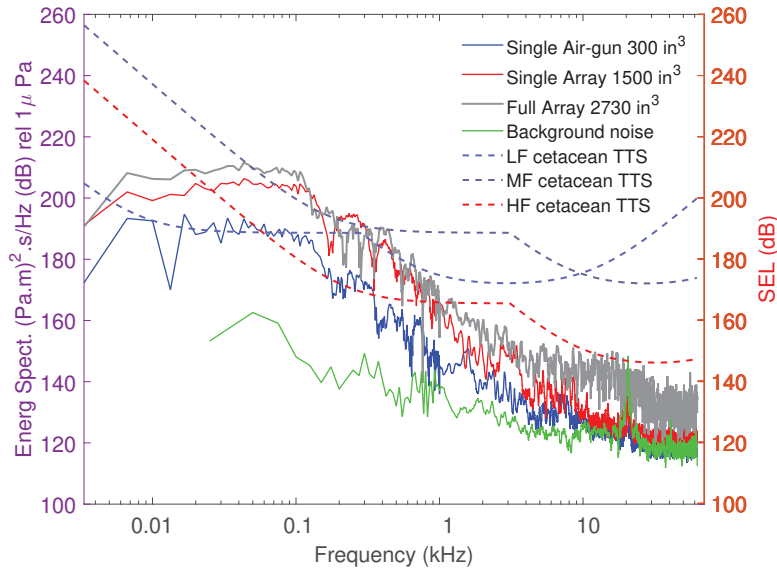


Figure 1.15: Energy spectrums of signals generated by, a single 300 in³ (solid blue), single array 1500 in³ (solid red), a full array 2730 in³ with three sub-arrays (solid grey), and Navy type II TTS exposure function for impulsive noise for LF, MF, and HF cetaceans shown in Figure 1.11

1.4.4 Behavioral effects

Other than temporary or permanent threshold shift (TTS or PTS), sound exposure might cause effects which are overlooked since they are more difficult to notice or hard to measure particularly in cetaceans (Tougaard et al., 2015). For example, physiological discomfort is hardly detectable before it becomes extensive enough to induce increased levels of stress hormones. Anthropogenic noise provokes behavioral responses and the elevated background noise might have longer term biological consequences.

There was a correlation observed between the amount of stress hormones in the North Atlantic right whales (*Eubalaena glacialis*) and the underwater noise based on measurements conducted between 2001 and 2004 in the Bay of Fundy, Canada (Rolland et al., 2012). Different Marine mammals showed behavioral disturbances when they were exposed to the noise from seismic air-guns (Stone et al., 2006). For instance, in response to active air-guns, baleen whales and orcas (killer whales) evinced localized spatial avoidance while small odontocetes showed strong lateral spatial avoidance. Feeding of several species of toothed whales (Miller et al. 2012; Isojunno et al. 2016), humpback whales (Sivle et al. 2016) and blue whales (Gold-

bogen et al. 2013) are observed to be interrupted during and after the end of exposure to naval sonar signal. Measurements indicate that as a result of increased noise in the frequency band of right whale calls, they have shifted their calls to higher frequencies within around three decades (Parks et al., 2007).

Noise from ships has most power at low frequencies. Therefore, it is considered to impact only the baleen whales that have good hearing at low frequencies and the species with sensitive high-frequency hearing have been overlooked. However, it is recently observed that the ignored weak high-frequencies from shipping noise induce noticeable behavioral responses in porpoises even 1000 meters away from the source (Dyndo et al., 2015). Unlike the previous study on captive porpoises, effects of noise exposure on free-ranging harbor porpoises under natural condition were quantified using sound and movement recording tags (DTAGs) (Wisniewska et al., 2018). It was revealed that exposure to the noise levels greater than 96 dB re 1 μ Pa rms in 16 kHz third octave band led to a general pattern of reduced foraging efforts. This study raises concerns regarding the effects of overlooked low-levels of high-frequency noise on other toothed whale species (Wisniewska et al., 2018).

1.5 Mitigation of air-gun noise impacts on the marine environment

To mitigate the impact of seismic air-gun arrays on marine wildlife, different strategies such as minimizing sound output, defining safety zones, soft-start or ramp-up, visual observations and passive acoustic monitoring (PAM) are implemented (Compton et al. 2008). To minimize the sound output it is recommended by the Joint Nature Conservation Committee (2017) to use the lowest power level required to fulfil the survey objectives or to minimize the amount of high-frequencies beyond the useful band for seismic imaging. Furthermore, air-guns should be arranged in the array to have most of the sound energy directed downwards and minimize the horizontal propagation (Johnson et al, 2007).

Safety zones or exclusion zones is the area around the source array where the received sound levels have potential to cause at least temporary hearing impairment (HESS, 1999).

Visual observation is the most common method for monitoring if animals are present in the safety zones and should be carried out by trained marine mammal observers (JNCC, 2004). If a marine mammal is observed within the safety

zone, mitigation strategies such as shutting-down the survey for 30 minutes will be implemented according to different guidelines by different countries (Weir and Dolman, 2007; Parsons et al., 2009; Nowacek et al., 2013). Visual observations are however restricted to day-light time and require relatively good weather and calm sea state. Furthermore, cetaceans spend most of their time submerged and come to the surface of the water for short time intervals. During the night it is more challenging to visually observe them even with night-vision cameras due to reduced view-field (Gordon and Steiner, 1992; Lewis et al., 2000). Other than visual monitoring, the area might be monitored acoustically using a short hydrophone array. With this technique, some of the animals that are calling can be detected but not located. The other possibility is using thermal infrared camera for monitoring (Verfuss et al., 2018).

Passive acoustic monitoring (PAM) technology helps to overcome some of the above-mentioned limitations of visual and acoustic observations. PAM uses a linear array of hydrophones towed behind the seismic vessel to detect and localize the vocalizing cetacean (Abadi et al., 2017). Augmenting PAM with visual observations increases the likelihood of localizing cetaceans. PAM is still a young technology and suffers from some issues such as error in distance estimation, undetected animals, limitation of low-frequency calls detection, engineering design for reliability, having low self-noise and low interference (Bingham, 2011). Use of PAM technology to supplement the visual surveys is encouraged by U.K.'s Joint Nature Conservation Committee (JNCC) (Wright and Cosentino, 2015). Another mitigation strategy is to gradually increase the source level and is called ramp-up or soft-start to allow the animal to leave the area. This approach starts usually with firing smallest air-gun in the array and subsequently additional air-guns are activated in ascending size order over a time duration of 30-45 minutes (Barlow and Gisiner, 2006). Soft-starts are one of the long-standing and main operational guidelines for seismic surveys. This strategy relies on the supposition that animals will move away from the source in a logical way. The expected logical response assumes that animals can and are willing to leave the area with disturbing noise. However, there may be areas with plenty of food which entice the animal to resist the noise until the exposure level become dangerous (Wright and Cosentino, 2015). There are observations which falsify the 'logical response' assumption. For example, using acoustic tagging on northern bottlenose whales indicated that lower sound might attract the animal to the sound source instead of warning it to move away. The tagged bottlenose whale turned to approach the sound source at a received SPL of 98 dB re 1 μ Pa. But in response to a received SPL of 107 dB re 1 μ Pa, the animal showed and unusual moves and then performed the longest and deepest recorded dive (94 min, 2339 m) for this species and afterwards the animal stayed unusually silent for several hours (Miller et al., 2015).

1.6 Alternative marine seismic sources

There have been many different marine seismic sources. Some of them such as air-guns have stood the test of time, while some others diminished by time for lack of competence (Parkes and Hatton, 1986). The challenge of new marine seismic sources is to have minimal impact on the marine environment while satisfying the requirement for seismic imaging. Some of these new sources are briefly explained in the following.

1.6.1 Air-guns with flexible bandwidth control (eSource)

A new air-gun, named eSource, reduces the environmental impact of marine seismic surveys by greatly reducing unnecessary high-frequency acoustic emission (Coste et al., 2014). eSource is jointly developed by Teledyne Bolt and WesternGeco. To understand the high-frequency generation mechanism and optimize the acoustic output, advanced computational fluid dynamics (CFD) was used. Such simulations are challenging because of extreme pressure gradients, multiphase flows, and supersonic velocities (Gerez et al., 2015). The short rise time - and consequently sharp slope - of the acoustic pulse causes almost all the high-frequency acoustic energy emitted by an individual air-gun. In the new air-gun design, the released air at the air-gun ports is regulated by controlling the motion of air-gun shuttle. In addition to the reduced high-frequencies, it generates lower peak pressure compared to the conventional air-guns while retains the useful low-frequencies for seismic imaging (Groenaas et al., 2016).

1.6.2 Marine Vibrators (MVs)

Vibrators were introduced in 1958 for onshore seismic explorations and could successfully replace explosive sources such as dynamites which were hazardous for operators (Wei et al., 2010). Accordingly, marine vibrators were introduced in the late 1960s and in principle they should reduce most types of environmental impacts compared to the impulsive sources such as air-guns. Output spectral energy of a vibrator can be controlled to avoid emission of frequencies outside the seismic band to reduce the impact on marine mammals. Furthermore, since the vibrator energy output is spread over a long-time interval, e.g. 10 s, the peak pressure output of a vibrator is much lower than that of an impulsive source. Therefore, marine vibrators might be less harmful to the aquatic environment (Dragoset, 1988). Despite these intriguing advantages, they have been far less used than air-guns in last 50 years (Gisiner, 2016).

Besides the problems related to the MVs mechanical durability, one of the most

crucial challenges with marine vibrators is the difficulty of generating low frequency acoustic waves. The required vibration amplitude to generate a desired sound pressure level (SPL) increases exponentially as the frequency decreases (Long and Tenghamn, 2018). To overcome the problem of inefficient low-frequency generation, the source should have a good impedance match with the surrounding water. The low-frequency generation can be enhanced by designing a source with low resonance frequencies which is a challenging task (Sornmo et al., 2016; Long and Tenghamn, 2018). There are achievements in improving the efficiency of MV's low-frequency generation by developing, for example, MVs with a flextensional shell. Due to their mechanical construction, they have two separate resonances in the low-frequency band which has enabled them to radiate low frequencies more efficiently (Tenghamn, 2013; 2006). An Efficient flextensional shell design provides improved coupling between the vibrator and water at low frequencies. Therefore, the vibrator can efficiently move a sufficient volume of water at low frequencies to create acoustic waves (Pramik et al., 2015). Controllability and repeatability of MV's output amplitude and phase is a crucial and challenging issue (Ozasa et al., 2015). Marine vibrators produce undesired high-frequency harmonic due to nonlinear effects. One method to effectively suppress the undesired higher harmonics is to use frequency-domain iterative learning control (Sornmo et al., 2016; Long and Tenghamn, 2018). Same as air-gun arrays, marine vibrators are also arranged in an array to meet the required amplitude spectrum (Mougenot et al., 2017).

1.6.3 Low Pressure Source and Tuned Pulse Source

Air-guns emit a considerable amount of unwanted high-frequencies into the marine environment. Part of these high frequencies is due to the generated jets of air by releasing high-pressure air through the ports. A new source which can be considered as an evolution of air-gun, operates with lower pressure, has increased air-volume, and modified ports shuttle (Ronen et al., 2015). The air released from a low-pressure source has larger raise time and shorter peak pressure. Furthermore, it is easier to control the discharge of air at lower pressure. Tuned Pulse Source (TPS) is a pneumatic acoustic source which operates with low-pressure air stored in a high-volume chamber (Ronen and Chelminski, 2017). It has a cup shaped flange and its ports are extended almost 360° around the operating housing. It generates acoustic pulse with a long raise time by releasing the large volume of air into the surrounding water over a controlled time. The length of the firing chamber tunes the pulse (Chelminski, 2015). Compared to the air-guns, TPS has much stronger low frequency content which is important for seismic imaging and especially important for full waveform inversion (FWI), sub-salt and sub-basalt

imaging. TPS mitigates the damage to the marine environment by generating less high-frequency acoustic waves which have potential to impact marine mammals especially those with sensitive hearing in the high-frequency band.

1.6.4 Encoded source sequences

In a conventional seismic acquisition, one source is activated at a time. The shot time intervals should be sufficiently large to avoid the interference of energy from previous shot with the next one (Berkhout, 2008). For marine seismic acquisition since there is a minimum vessel speed limitations, the required minimum time interval between the shots limits not only the acquisition rate but also in-line source sampling (Moore et al., 2008). Acquisition of simultaneous source data, also referred to as blended acquisition, improves the acquisition efficiency and provides data with denser source sampling and hence better seismic images (Hampton et al., 2008; Abma et al., 2015). However, when firing several sources nearly simultaneously, conventional seismic imaging processing are not appropriate because the recorded data contain wave-fields from more than one source. To solve this problem, separation of the wave-fields from corresponding sources must be performed before further processing. Source encoding is one of the methods which enables simultaneous source separation by a processing technique (Robertsson et al., 2008). Unlike a conventional air-gun array, where all the air-guns are activated simultaneously to generate an impulsive source signature, in the source encoding method the individual air-gun are activated sequentially over an extended time period. The activation time pattern is referred to as a Popcorn pattern and the time-extended source signal is called a Popcorn signature (Abma and Ross, 2013 and 2015). By designing the orthogonal encoded source sequences, separation of wave-fields are achieved by cross-correlating the data with the corresponding source sequence (Muller et al., 2015). Nowadays thanks to the availability of High-performance computational resources, it is possible to reconstruct the equivalent impulsive source signal from encoded source datasets using a sparse inversion algorithm which is computationally demanding (Muller, 2016). Furthermore, the pattern can be designed to attenuate the source ghost, reduce or control the bubble interaction between air-guns (Abma and Ross, 2015; Mougnot et al., 2017).

In addition to the mentioned benefits for seismic acquisition, due to the distributed activation times, the peak pressure amplitude of the source signature is much smaller than that of conventional air-gun array signature and thereby reduces its potential environmental impacts (Abma and Ross, 2015; Muller, 2016).

1.7 Basic acoustic source models

Any acoustic source can be expressed mathematically as a dominant order of a multipole (Ross, D. 1976). Many of the acoustic sources can be modeled in terms of simple sources such as breathing spheres, oscillating pistons or combinations thereof (Norton and Karczub, 2003, chapter 2). Therefore, basic equations for acoustic pressure and power radiation by these two simple sources are briefly reviewed in this section. Before introducing two basic acoustic sources, it is helpful to define acoustic impedance and radiation efficiency.

1.7.1 Acoustic impedance and radiation efficiency

In an ideal acoustic source, all its energy should be converted into an acoustic field. But in practice, sources generate a hydrodynamic non-radiating field in addition to the radiated acoustic pressure field. Radiation impedance is a useful definition to express these concepts (Ross, D. 1976):

$$Z_r = R_r + jX_r \quad (1.7)$$

The real and imaginary parts are called resistance and reactance, respectively. The former is proportional to the acoustic power while the later one is proportional to the hydrodynamic non-radiating motion of medium.

Acoustic generation is caused by the compressibility of a medium. Since water is less compressible than air, acoustic conversion efficiencies of sources in water are much less than those in air (Ross, D. 1976). In analyzing acoustic sources, acoustic conversion efficiency (or radiation efficiency) is an instructive concept. It is defined as the ratio of radiated acoustic power to the entire power in the acoustic and hydrodynamic motion (Ross, D. 1976):

$$\eta_{rad} = \frac{W_{ac}}{W_{ac} + W_{hyd}} = \frac{R_r}{|Z_r|} = \frac{R_r}{\sqrt{R_r^2 + X_r^2}} \quad (1.8)$$

In the above equation, W_{ac} is the acoustic power and W_{hyd} hydrodynamic sloshing motion of fluid. In the following we will analyze the radiating acoustic pressure by a pulsating sphere and a vibrating circular disk.

1.7.2 Pulsating sphere

For a radially oscillating (pulsating) sphere with frequency ω , equilibrium radius a , and normal surface velocity $\mathbf{u}_a = U_a e^{i\omega t}$, the fluctuating acoustic pressure at distance r from the center of sphere is (Norton and Karczub, 2003 chapter 4; Pierce, 1989 chapter 4):

$$p(r, t) = \frac{a^2 U_a}{r} \left(\frac{jk\rho c}{1 + jka} \right) e^{j(\omega t - k(r-a))}. \quad (1.9)$$

Where k is the wave-number, ρ is density, and j is the imaginary unit. When $ka \ll 1$, i.e. for low frequency approximation or when the sphere is small compared to the acoustic wavelength, equation 1.9 can be written as:

$$p(r, t) = \frac{j\rho c k a^2 U_a}{r} e^{j(\omega t - k(r-a))}. \quad (1.10)$$

When $ka \gg 1$, i.e. for high frequency approximation or when the sphere is large compared to the acoustic wavelength, equation 1.9 can be written as:

$$p(r, t) = \frac{\rho c U_a}{r} e^{j(\omega t - k(r-a))}. \quad (1.11)$$

For a pulsating sphere the acoustic radiation impedance evaluated at the surface is (Ross, 1976; Norton and Karczub, 2003, chapter 4):

$$Z_r = \rho c S_0 \left[\frac{(ka)^2}{1 + (ka)^2} + \frac{jka}{1 + (ka)^2} \right]. \quad (1.12)$$

Where S_0 is the surface area of the sphere. The radiated acoustic power is obtained by (Lawrence et al., 2000 chapter 7; Pierce, 1989 chapter 4):

$$\Pi = \frac{1}{2} U_a^2 R_r. \quad (1.13)$$

Where the R_r is the real part of Z_r in equation 1.12. The radiation efficiency can be obtained from equations 1.8 and 1.12.

1.7.3 Vibrating baffled circular piston

Another simple acoustic source is a vibrating baffled circular disk. The pressure at distance r from the center of the sphere is (Norton and Karczub, 2003 chapter 4; Pierce, 1989 chapter 4):

$$p(r, \theta, t) = \frac{j}{2} \rho c U_a \frac{a}{r} k a \left[\frac{2J_1(ka \sin \theta)}{ka \sin \theta} \right] e^{j(\omega t - kr)}. \quad (1.14)$$

The term in the brackets represents directivity factor. Acoustic radiation impedance evaluated at the piston surface is (Lawrence et al., 2000 chapter 7; Pierce, 1989 chapter 5):

$$Z_r = \rho c S_0 \left[\left(1 - \frac{2J_1(2ka)}{2ka} \right) + j \frac{2H_1(2ka)}{2ka} \right]. \quad (1.15)$$

In the above equation, J_1 and H_1 are the Bessel function and Struve function of first order, respectively. The surface area of the piston is represented by S_0 . Then the acoustic power radiated by the baffled circular piston is estimated using equation 1.13 where R_r is the real part of radiation impedance in equation 1.15.

Based on the given formulas in this section, acoustic radiation efficiency of a pulsating sphere and a vibrating baffled circular piston with the initial radius of 0.3 m and 0.6 m are given in Tables 1.1 and 1.2 for eight frequencies. Furthermore, the required vibration amplitude and input energy at different frequencies to generate a source level of 195 dB and 205 dB (rel $1\mu\text{Pa}$) for a pulsating sphere and a vibrating baffled circular piston with two different equilibrium radiuses are given in Tables 1.1, 1.2, and 1.3.

Table 1.1: 195 dB 1m rel $1\mu Pa$, $a_0 = 0.3m$

$f(Hz)$	Sphere			Piston		
	A(mm)	RE (%)	IP (kW)	A(mm)	RE (%)	IP (kW)
7	45.6	0.88	30.1	91.4	0.52	25.6
10	22.4	1.26	21.1	44.8	0.74	17.9
30	2.5	3.77	7.02	5	2.2	6
50	0.9	6.27	4.21	1.8	3.7	3.6
100	0.2	12.5	2.09	0.45	7.4	1.8
500	0.01	53.2	0.36	0.018	36	0.35
1000	0.003	78.3	0.21	0.0045	66	0.155
5000	0.0006	98.8	0.26	0.0002	99.7	0.0069

 f : Frequency

A : Amplitude

RE: Radiation Efficiency

IP: Input Power

Table 1.2: 195 dB 1m rel $1\mu Pa$, $a_0 = 0.6m$

$f(Hz)$	Sphere			Piston		
	A(mm)	RE (%)	IP (kW)	A(mm)	RE (%)	IP (kW)
7	11.4	1.7	15.1	22.8	1.0	12.8
10	5.6	2.5	10.5	11.2	1.48	8.9
30	0.62	7.5	3.5	1.24	4.44	3.0
50	0.22	12.5	2.1	0.44	7.4	1.8
100	0.056	24.4	1.0	0.11	14.7	0.89
500	0.0028	78.2	0.21	0.0045	66	0.15
1000	0.0014	92.9	0.25	0.0011	96.3	0.05
5000	0.0003	99.7	0.26	0.00004	99.9	0.002

Table 1.3: 205 dB 1m rel $1\mu Pa$, $a_0 = 0.6m$

$f(Hz)$	Sphere			Piston		
	A(mm)	RE (%)	IP (kW)	A(mm)	RE (%)	IP (kW)
7	36.1	1.7	150.6	72.2	1.0	127.8
10	17.7	2.5	105.4	35.4	1.48	89.5
30	1.97	7.5	35.1	3.9	4.44	29.8
50	0.71	12.5	20.9	1.4	7.4	17.9
100	0.18	24.4	10.2	0.35	14.7	8.9
500	0.0088	78.2	2.1	0.0142	66	1.5
1000	0.0044	92.9	2.5	0.0035	96.3	0.49
5000	0.0009	99.7	2.6	0.0001	99.9	0.016

It is seen that the required vibration amplitude and input power increases drastically by reducing the frequency. As expected the pulsating sphere is more efficient acoustic radiator than vibrating piston. By increasing the size of acoustic source, the required vibration amplitude and input power to generated certain sound pressure level decreases.

1.8 K-space pseudo spectral method

To investigate the acoustic properties of the ghost cavitation cloud, numerical methods are required. There are several different numerical schemes to solve acoustic wave equation. Finite-difference time-domain (FDTD) method (Yee, 1966) which has been widely used to solve electromagnetic wave equations, is applied in other fields such as acoustics (Chang and McMechan, 1989; Botteldooren, 1995; Wang, 1996) where numerical methods are required to solve time-dependent partial differential equations. Both the spatial and temporal derivatives are approximated by finite difference equations usually based on Taylor series expansion. The number of terms used in the Taylor series determines the accuracy of the approximation. It is possible to start discretizing second-order acoustic wave equation or a set of coupled equations based on conservation of mass, momentum and equation of state (Liu, 1998). Discretizing and solving a set of coupled first order equations makes it easier to include mass and force sources and to include a perfectly matched layer (PML) around the computational domain. PML absorbs the acoustic waves that reach the boundaries of the computational domain and prevents

their reflection back to the computational domain. FDTD suffers from excessive dispersion error which accumulates with time as the waves advance in the computational domain (Hadi and Picket, 1997). To overcome the dispersion problem, one method is to use a relatively large number of nodes per minimum wavelength or decrease the time step. Therefore, the FDTD method is computationally expensive. Alternatively, higher order finite-difference methods can be used which means including more terms of Taylor series in the difference approximations (Zygidis and Tsiboukis, 2004). Instead of using local approximation to the spatial derivatives based on finite differences, pseudo-spectral methods use a Fourier transform to estimate the spatial derivative using all the grid points. Then only two grid points per shortest wavelength are required to achieve the same accuracy as 8-16 grid points per shortest wavelength in the FDTD method (Liu, 1997). Therefore, pseudo-spectral finite difference (PSTD) methods are much more efficient than FDTD methods. While spatial derivatives are accurately represented using Fourier transform, the temporal derivatives are significantly dispersive in PSTD methods (Tabei et al, 2002) and therefore the small time-step requirement reduces their expected efficiency. Temporal derivative estimations can be considerably improved by using k-space family of methods which use k-t (spatial frequency and time) space scheme for temporal iterations (Bojarski, 1982; Mast et al., 2001). Same as pseudo-spectral methods which require fewer grid points per wave length, the use of Fourier Transform in k-space has made it possible to have larger time steps (Cox et al., 2007). K-space pseudo-spectral algorithm is more efficient than many finite-difference and finite-element methods because it provides same degree of accuracy with much coarser grid spacings and larger time steps (Tabei et al., 2002). K-wave is an efficient MATLAB toolbox for acoustic wave propagation (Treeby and Cox, 2010; Treeby et al., 2012). It uses k-space and pseudo-spectral method for temporal and spatial discretization, respectively.

1.9 Thesis structure

The main part of this thesis comprises four independent papers, either published or submitted to peer-review journals and a peer reviewed conference paper is presented as an appendix. Therefore, invariably and inevitably there are some overlapping introductory and background materials presented in different chapters.

In chapter 2, a synthetic modeling scheme for modeling ghost cavitation and the resulting acoustic signal is presented. By superposition of pressure fields from air-guns, the pressure around the array is estimated. Temporal and spatial distribution of locations where the cavitation is likely to occur, that is when the pressure

drops below the water vapor pressure, are determined. In the second step, cavity growth and collapse are modeled at different locations using the Prosperetti bubble dynamic equations and subsequently the resulting pressure signature is estimated. Individual cavity pressure signatures are propagated from where they are formed to the receiver location. Geometrical spreading and absorption effects are included. By adding the signatures of individual cavities, the resulting acoustic signal from the cavity cloud is obtained. The results are compared to the field recorded data. There is a good correspondence between modeled and measured data regarding the onset time and the duration of the high-frequency cavitation signal.

In chapter 3, using the developed ghost cavitation modeling scheme in the previous chapter, the ghost cavitation signal for two different air-gun arrays were modeled. Both arrays have three sub-arrays. One of the arrays has total air-chamber volume of 2730 in³ and the distance between the sub-arrays is 6m. The second one has total air-chamber volume of 3250 in³ with 8m horizontal distance between the sub-arrays. The second array generates around 150% more high-frequencies (>5 kHz) while its energy in the seismic band is only around 20% more than the smaller array.

In chapter 4, the ghost cavity cloud generated by an air-gun array with two sub-arrays is video recorded using a high-speed video camera. It is the first convincing photographic evidence of the ghost cavitation phenomena. Acoustic signals were measured by a broad-band hydrophone suspended below the array. There is a good agreement between the onset and duration of photographed cavity cloud and the one from modeling. The shape and position of modeled and photographed cavity clouds share similar features. The envelopes of high-pass filtered modeled and measured acoustic signal fits the field measured acoustic signal.

In chapter 5, the sound varying velocity within the cavity cloud is investigated by comparing the numerical modeling to the far-field recordings. Presence of vapor cavities within the cloud can significantly drop the sound speed of water within the cavity cloud at frequencies below the resonance frequencies of the cavities. Therefore, it is an acoustic wave propagation in a time-dependent medium. A modified k-wave which is a k-space pseudo-spectral numerical method is used to model effects of temporarily sound velocity reduction within the cavity cloud on the far-field acoustic recording. We observed that temporarily sound velocity reduction of 50% within the cloud changes the modeled.

In appendix A, the effects of cavity collapses within the ghost cavity cloud on the near-field hydrophones are simulated. In this paper the model is tuned (calibrated) such that both the amplitude of high-frequency modeled signal and its associated low-frequency part matches the measurements.

1.10 Contributions

The contributors to the papers in the thesis are as follows:

- **Paper 1, Chapter 2:** Acoustic generation of underwater cavities – comparing modeled and measured acoustic signals generated by seismic air gun arrays. *Published in The Journal of the Acoustical Society of America*, Volume. 141, Issue 4 (April 2017), 2661-2672. DOI: 10.1121/1.4979939. This work was performed by Babak Khodabandeloo as the lead author and researcher. Martin Landrø participated as a supervisor. Alfred Hanssen wrote the section about cavitation in plasma, contributed in discussion about interaction between cavities, reviewed and helped in discussion of the paper.
- **Paper 2, Chapter 3:** High frequency ghost cavitation – a comparison of two seismic airgun arrays using numerical modelling. *Published in Energy Procedia*, 125 (2017), pp.153-160. This work was performed by Babak Khodabandeloo as the lead author and researcher. Martin Landrø participated as a supervisor.
- **Paper 3, Chapter 4:** Acoustically induced cavity cloud generated by air-gun arrays – comparing video recordings and acoustic data to modeling. *Published in The Journal of the Acoustical Society of America*, Volume. 143, Issue 6 (June 2018), 3383-3393. DOI: 10.1121/1.5040490. This work was performed by Babak Khodabandeloo as the lead author and researcher. Martin Landrø participated as a supervisor.
- **Paper 4, chapter 5:** Characterizing acoustic properties of cavity cloud as a time-dependent effective medium surrounding an air-gun array. *The paper is under review in Geophysical Journal International*. This work was performed by Babak Khodabandeloo as the lead author and researcher. Martin Landrø participated as a supervisor.
- **Paper 5, Appendix:** Effects of Ghost Cavitation Cloud on Near-field Hydrophones Measurements in the Seismic Air Gun Arrays. Published In 79th EAGE Conference and Exhibition 2017. This work was performed by Babak Khodabandeloo as the lead author and researcher. Martin Landrø participated as a supervisor.

Chapter 2

Acoustic generation of underwater cavities – comparing modeled and measured acoustic signals generated by seismic air gun arrays ¹

Babak Khodabandeloo, Martin Landrø
*Department of Geoscience and Petroleum,
Norwegian University of Science and Technology (NTNU)
NO-7491 Trondheim, Norway*

Alfred Hanssen
*Department of Geosciences, ARCEX, University of Tromsø
The Arctic University of Norway,
NO-9037 Tromsø, Norway*

¹Paper Published in *the Journal of the Acoustical Society of America*, Volume. 141, Issue 4 (April 2017), 2661-2672. DOI: 10.1121/1.4979939

2.1 Abstract

Underwater vapor cavities can be generated by acoustic stimulation. When the acoustic signals from several air guns are reflected from the sea surface, the pressure drop at some locations is sufficient for cavity growth and subsequent collapse. In this paper the generation of multiple water vapor cavities and their collapses are numerically modeled and the results are validated by comparing with field data from a seismic air gun array test. In a first modeling attempt where cavity interaction is neglected, a correspondence between measured and modeled data is found. Then, this correspondence is improved by assuming that the acoustic signal generated by the other cavities changes the hydrostatic pressure surrounding each cavity. This modeling can be used to estimate the amount and strength of high frequency signals generated by typical marine air gun arrays, given that a calibration step is performed prior to the modeling.

2.2 Introduction

2.2.1 Background

Underwater man-made noise is recognized to have several adverse effects on aquatic animals and it is a worldwide problem (Southall, 2008; Williams et al., 2015). Such noise is mainly due to shipping, seismic surveys, military activities, and pile driving for offshore construction (Hildebrand, 2009). In marine seismic surveys, most common and widely used techniques utilize acoustic waves to image the earth's subsurface. A majority of this type of surveys is for hydrocarbon exploration. An active source radiates acoustic waves into the earth and subsequently the subsurface structure is determined from measured reflected elastic waves using a large number of receivers. These receivers might be hydrophones organized in long cables that are towed behind the seismic vessel, or geophones that are deployed at the seabed. For seabed geophones, it is today common to measure the three spatial components of the displacement field (x , y and z) and in addition to measure also the pressure component using a single hydrophone. This is known as four-component seismic, or 4C seismic. On the other hand, acoustic waves that propagate in the water layer are crucial and a very effective sensory tool for marine mammals. These animals use sound for a variety of vital purposes such as foraging, social interactions, mating, navigation, and detecting predators (Wright et al., 2007). Effects of the anthropogenic noise on marine fauna can be behavioral reactions (McCauley et al., 2000), acoustic masking, prey effect, physiological effects (Nowacek et al., 2007), and/or hearing impairment and threshold shifts (either temporarily or permanently) (Erbe and Farmer, 2000; Gordon et al., 2003). Marine animals use different frequency ranges for communication and echolocation.

Many species of toothed whales, one of two main groups of cetaceans, use 1-20 kHz for communication and 20 kHz to 150 kHz for echolocation. The other group, baleen whales, uses lower frequencies ranging from 12 Hz to 8 kHz (Richardson et al., 1995). To reduce the impact of noise on the marine mammals, it is reasonable to avoid or reduce overlap with their frequency ranges (Ketten, 2004). It should be noted that detailed knowledge of how and to what extent marine mammals exploits acoustic waves is still not fully explored. Air gun arrays are the most common and efficient marine seismic source compared to other seismic sources such as marine vibrators and water-guns (Duren, 1988; Barger and Hamblen, 1980). Marine seismic acquisition is a major noise source in the marine environment and its impacts on aquatic life are therefore crucial to understand. Air guns produce loud impulsive bursts of underwater sound by a sudden release of high pressure air (typically 137 bar) which forms a rapidly expanding and contracting bubble (Caldwell and Dragoset, 2000). In practice instead of using one single air gun, several air guns with different volumes are used together which is referred to as an air gun array. The purpose of using many air guns is to increase the strength of the seismic source, to enhance the source signature, as well as to modify directionality of the source to reduce the lateral directivity (Dragoset, 2000). Such arrays radiate acoustic waves that propagate through the water layer and into the subsurface beneath the seabed. Subsequently, seismic profiles for hydrocarbon exploration and scientific mapping of the earth's crust are created from measured responses using receiver cables that are towed behind a seismic vessel or deployed at the seabed. For seismic imaging, only low frequencies (less than 100 Hz) are required since they penetrate deeper into the earth. However, there are also much higher frequencies generated by air gun arrays which do not benefit seismic imaging. Goold and Fish (1998) measured frequencies up to 22 kHz some kilometers away from a 2120 cubic inch air gun array. Using a broad-band hydrophone, it was reported that air-gun arrays produce significant high frequencies up to 60 kHz (Landrø et al., 2011) but much weaker than the signal recorded at seismic frequencies. These high frequencies emitted from air gun arrays overlap with the hearing curves of many cetacean species and may adversely affect them (Ketten, 2004, Landrø et al., 2011). Despite some concerns about seismic air gun impact on marine life (NRC, 2003; Madsen et al., 2006), they are still the dominant seismic source (Landrø and Amundsen, 2010; Weilgart, 2013). The main reason is that there is no better seismic source today and that the impact on marine life is considered low or minimal. Marine seismic vibrators were introduced few years after the air gun and since then they have been in development. But they are still not a popular seismic source because of weak signal and practical issues related to operations. The radiated acoustic power is proportional to the square of the radiator size to the wavelength ratio (Norton and Karczub, 2003). Consequently they must be impractically large to radiate

low frequency acoustic waves efficiently. Sources such as the Low level Acoustic Combustion Source (Askeland, 2007), Tunable Organ Pipe (Morozov and Webb, 2007) Hydro-acoustic Transduction (Bouyoucos, 1975) and low pressure air gun (Chelminski, 2015) may remain a future solution. The interest to reduce the high frequency content generated by air gun arrays is increasing. An air gun silencer was tested for a 50 bar air gun and the experimental results showed that frequencies above 700 Hz were reduced by approximately 6 dB (Spence et al., 2007). The drawbacks are the need for replacing acoustically absorbent foam in the silencer after few shots and the silencer effectiveness is not satisfactory (Spence, 2009). To reduce the high frequencies which are due to the steep rise time of pressure signals from each individual air gun, a new air gun was designed and successfully tested (Coste et al., 2014; Gerez et al., 2015). Another mechanism is interaction between reflected ghost wave and air gun bubble which generates frequencies between 400-600 Hz (King, et al 2015a; King, 2015b). A third high frequency generation mechanism is ghost cavitation (Landrø et al., 2011). It was observed that a full air gun array, unlike single air guns or single arrays, has a much larger high frequency content compared to single guns. This signal occurs a few milliseconds after the ghost reflection (Landrø et al., 2011). Such high frequencies are attributed to cavitation phenomena caused by reflected pressure signals from the water-air surface. These reflections are referred to as ghost signals, and hence the term ghost-cavitation is used for this phenomenon.

2.2.2 Acoustic waves and cavitation

Acoustic waves in a liquid can generate cavities. When the water pressure drops below the vapor pressure or partial pressure of the dissolved gases, there is a possibility of vapor or gas cavity formation in the liquid (Mellen, 1954; Plesset, 1970). The vapor cavity is called acoustic cavitation if it is from an oscillating pressure due to an acoustic wave propagating through a liquid (Frohly et al., 2000; Apfel, 1984). The threshold pressure in an acoustic field that ruptures the water and creates cavitation varies significantly from moderate low pressures to high relative negative pressures. However, it is experimentally observed that presence of cavitation nuclei facilitates cavity generation (Caupin and Herbert, 2006; Herbert et al, 2006; Brennen, 2013). For example in a venturi nozzle experiment, cavitation was observed when a small air bubble entered the low pressure region (Harrison, 1952). Cavitation collapse generates loud noise and high frequencies. For example acoustic pressure is measured up to 0.7 MPa at distance of 1-3 cm from cavity collapse from a snapping shrimp (Lohse et al., 2001). The pressure inside a cavity at its minimum size is very high and might be up to thousands of bars (Mellen, 1954; Yasui et al., 2010; Harrison, 1952). The cavitation noise is most severe when there are many collapsing cavities together which is often denoted cloud cavitation (Re-

isman et al., 1998). In the case of air gun arrays, ghost cavitation clouds can be formed because of the sudden pressure drop due to multiple reflected ghost signals from several single air guns in the array (Landrø et al., 2011, 2013). This acoustically generated cavitation is assumed to be generated by a cavitation cloud and this hypothesis was further confirmed by more dedicated experiments (Landrø et al., 2016).

2.2.3 Cavities in plasma due to an external electric field

It is interesting to note that there exists a surprisingly similar dynamical phenomenon in driven and damped plasmas. Plasmas are (partially) ionized gases, which imply that their dynamical properties are dominated by long range Coulomb forces acting between the charged particles (Pecseli, 2012). By driving a plasma with an external electric field, an ensemble of cavities (density depressions or “cavitons”) may form by means of a resonance mechanism (nucleation). Local high-frequency electric fields can be trapped in these cavities, inducing a collapse of the cavities until they become so small that they dissipate their energy as heat and sound waves (the burn-out) (Russell et al., 1986; Hanssen et al., 1992). Thereafter, the burnt-out cavities relax until they again become the nucleus for a new cycle of cavity nucleation, collapse, and burn-out. This phenomenon is called strong plasma turbulence (Russell et al., 1986; Hanssen et al., 1992), and it results in heating of the plasma, in addition to emission of sound and electromagnetic waves (Mjøllhus et al., 1995).

We believe that the similarity between nucleation-collapse-burnout dynamics in plasmas and cavitation-expansion-collapse in fluids is more than skin-deep. Hence, both systems is governed by an external energy source (sound pulses in the case of seismic, electromagnetic waves in the case of plasma), and both kinds of cavities dissipate their energy to the surrounding medium as they dampen and finally collapse. The dynamics is inherently nonlinear, rendering the modelling and analysis difficult. The air gun generated bubble dynamics is in many ways the more complex of the two, as it involves phase transitions which does not take place in plasma turbulence. Also, under certain conditions a hot and dense microplasma may be formed inside the vapor cavities, emitting electromagnetic waves (light and UV radiation) during their collapse (e.g., Bataller et al., 2014; McNamara et al. 1999). This connection between the plasma caviton collapse and vapor cavities collapse in fluids indicates interesting similarities between nonlinear fluid dynamics and nonlinear plasma dynamics. It is evident that the emitted sound and light from both types of collapse points to some deeper common underlying dynamics that is still poorly understood. In this work we have modelled the ghost cavitation signal by assuming that the measured signal at any location is an aggregate of individual signatures from cavity collapses. To do so, temporal and spatial dis-

tribution regions around the air guns where cavities are more likely to be formed are required. The pressure values around the air guns are calculated based on air gun array signature modeling. Then, it is determined where and when the pressures drop below the assumed threshold level for cavitation growth. Afterwards, using bubble dynamics equations, the response of a microbubble, or impurities, to the estimated pressure from air gun arrays and their ghost is obtained. Having the cavitation signature corresponding to the estimated minimum pressure and its location and formation time, it is possible to forward propagate it to the receiver point. Geometrical spreading and absorption effects are included. Results of this modelling provide us with strong evidence that supports the ghost cavitation hypothesis. This work improves our understanding of one of the underlying mechanisms for the high frequency content of air gun arrays which might be used to develop strategies to reduce them. Even though we lack enough data regarding effects of noise on marine mammals we don't know how much these high frequencies bother or impact marine fauna. Hence, reducing the high frequency content is a correct strategy and as a pre-caution. To our knowledge this is the first attempt to perform quantitative modeling of the ghost cavitation signal and compare the modeled results to far field measurements.

2.3 The field experiment

The field experiment was conducted in 2008 in the Black Sea offshore Turkey. The source vessel was sailing along a straight line above a permanent hydrophone located at the sea bed. The shot interval was 25 meters. The process is schematically shown in Figure 2.1. The Location of the hydrophone with respect to the closest shot is given by $x_0 = 1.2m$, $y_0 = 39m$, and $z_0 = 55m$.

Normalized measured signals for shot number 15 to 25 and their 10 kHz high pass (HP) filtered signals are plotted together in Figure 2.2. It is clear that shot 20 is the closest shot to the hydrophone.

We have plotted the normalized measured signal for shot 20 –which is the nearest shot to the hydrophone –and its normalized 10 kHz HP filtered signal as well as the 200 Hz low pass (LP) filtered signal in Figure 2.3. It is observed that the strong high frequency signal appears a few milliseconds after the surface ghost. The energy level of the high frequencies (>10 kHz) is around 50 to 60 dB less than the maximum energy level of the air gun signal which occurs between 50 to 100 Hz (Landrø et al., 2011). To compare the relative magnitude of the low and high (>10 kHz) frequency signals the raw and the high-pass filtered signals are shown without normalization in Figures 2.3a and 2.3b, respectively. We observe that the amplitude of the high frequency signal is around 2-3% of the amplitude of the raw signal. However, although the signal strength is weak compared to the low-

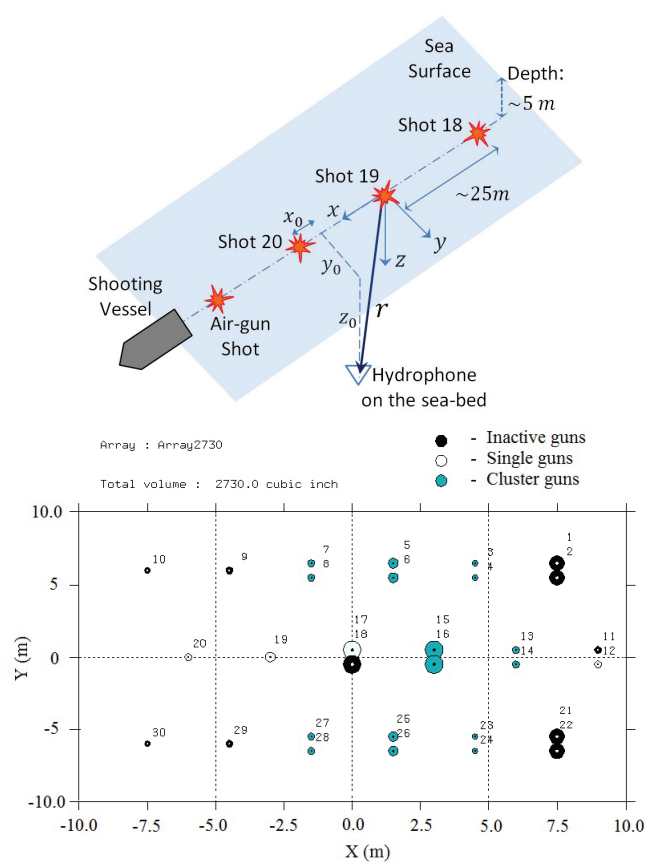


Figure 2.1: Top: Schematic view of the field experiment; the hydrophone is stationary at the sea bed. The shooting vessel moves along a straight line above the hydrophone. The source depth is 5 meter. Below: The air gun array configuration seen from above.

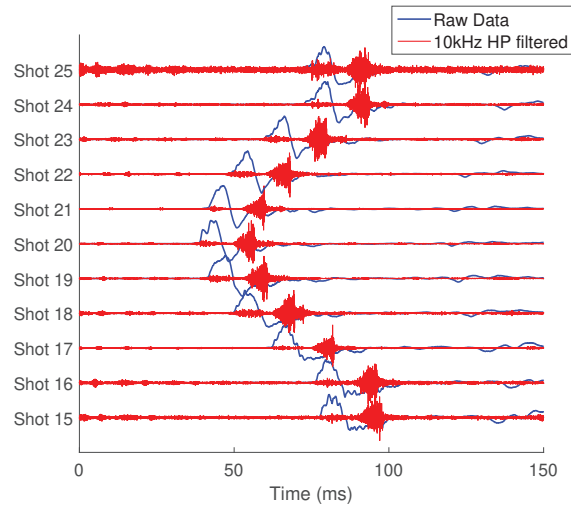


Figure 2.2: Normalized raw measured signals (blue lines) and their normalized 10 kHz HP filtered signal (red lines) for different shots 15 to 25.

frequency part of the air gun signature, these high frequencies might still influence marine mammal behavior. For example the hearing of many of the odontocetes (toothed whales) is around 80 to 100 dB more sensitive in the frequency range from 10 to 100 kHz compared to lower frequencies (Ketten, 2004).

To have a reference point (zero time) for selecting the high frequency signals, the reference is chosen 5 ms after the peak time of the low pass filtered signal for each shot. The reference point is important for comparing the measured field data with those from simulations which will be discussed later in this paper.

2.4 Ghost cavitation signal modeling

When the content (which is water vapor molecules) of a cavity is highly compressed, the pressure inside the cavity is increased tremendously and its subsequent sudden collapse produces an intense acoustic signal (Brennen, 2005). There are several marine animals that create cavities in the water. The killer whale creates cavities by rapid movement of the tail. Another good example is the pistol shrimp which generates a cavity by snapping the claw (Versluis et al., 2000). There are differences between collapses of a single cavity in the free field versus near boundaries and or presence of other cavities in its vicinity. A single cavity in free field collapses in a spherical shape without any liquid jet or vortex ring formation (Lauterborn and Hentschel, 1985). On the other hand, the cavities will be distorted due to the existing pressure field from other cavities or boundaries. Other effects

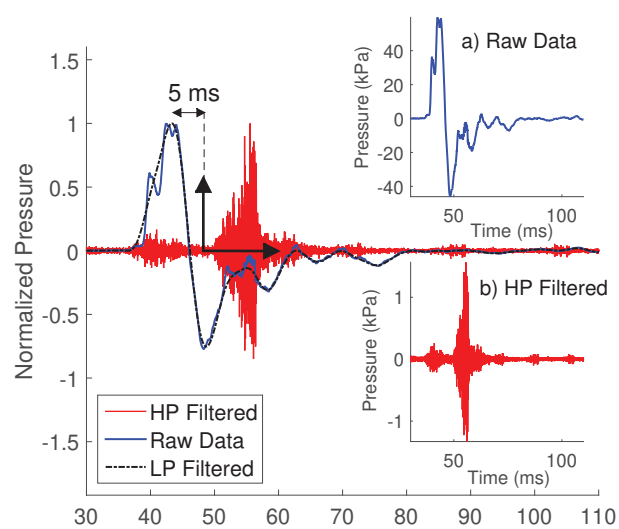


Figure 2.3: Normalized raw measured signal (blue) for shot 20 and its normalized 10kHz high pass filtered signal (red). The corresponding low pass filtered signal is shown as a black dashed-dotted line. The reference point (zero time) for HP filtered signal is shown by thick black axes. To compare the magnitude of high frequencies with the measured signal, raw measured signal at hydrophone and its 10 kHz high passed filtered signal are also plotted without normalization in (a) and (b), respectively.

related to cavity creation are jet formation, coalescence or proliferation of cavities (Chew et al., 2011). Furthermore, by solving the Keller-Miksis equation numerically (Li et al., 2013), it was shown that the presence of smaller cavity intensifies the pressure pulse of bigger ones compared to isolated cavities and is maximized when the cavities have equal initial radii. Experimental results also show that severe cavitation noise and very large pressure pulses occur when many cavities collapse within a cloud in close proximity to each other (Reisman et al., 1998; Wang and Brennen, 1995). Despite the fact that interaction between cavities is complex, Harrison (1952) argues that the noise spectrum from a cloud of cavities can be considered to be formed by summation of pulses from individual cavities. Hence, we will assume a simple model for our modeling, assuming a simple superposition of individual cavities that collapse.

2.4.1 Modeling the pressure drop caused by reflected air gun signals from the sea surface

Reflected acoustic pressure waves from the sea surface have opposite polarity compared to the positive incident wave from individual air guns in an air gun array. This reversal is due to the fact that the reflection coefficient of pressure waves is close to -1 for the water-air interface. It is important to stress that this polarity reversal occurs for the relative or dynamic pressure, which is the acoustic pressure relative to the hydrostatic pressure. This means that the absolute pressure in the water is never negative, however, when the dynamic pressure is negative, the absolute pressure will approach zero, and cavity creation will then occur. Such negative pressure created by the ghost signals from many individual air guns might “add up” in some regions and cause the absolute hydrostatic pressure to approach zero. To find the spatial and temporal distribution of the absolute hydrostatic pressure in the water and map when and where it approaches zero, we use air gun modeling (Ziolkowski, 1970). We model the acoustic pressure generated by the air gun array in a volume surrounding the array. This volume is divided into small cells using a grid resolution of 0.2 m and a computational time sampling of 0.1 ms. Using these dense values for time and space discretization, ensures no spatial and temporal aliasing in the modeling of the pressure. The regions where the absolute hydrostatic pressure of water is less than -0.1 bar are shown at four different time instants in the top row of Figure 2.4. Here it should be noted that the air gun modeling theory is based on linear superposition when the pressure contribution from each air gun is added, and the actual number of -0.1 bar is an assumption which is found practical to achieve a reasonable match between modeled and measured data. As the absolute pressure in the water approaches zero, the superposition principle breaks down due to non-linear effects which are not accounted for in the modeling software we use. Since each air gun is considered as a point source in the

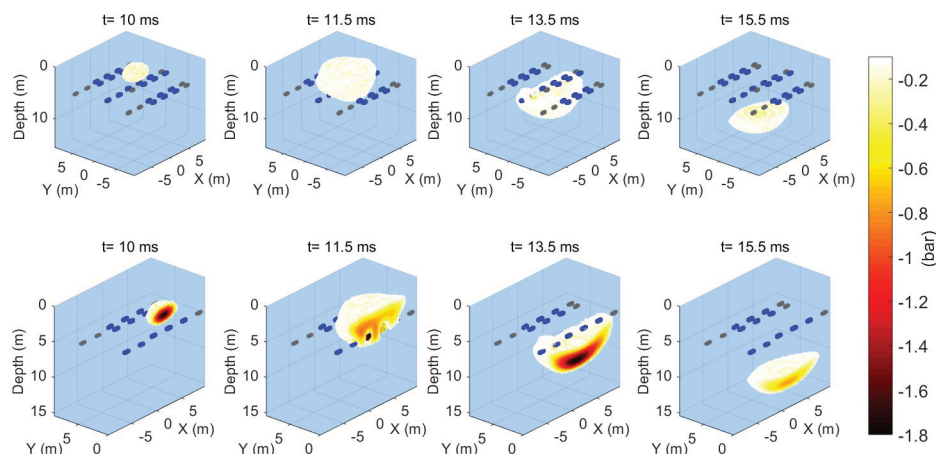


Figure 2.4: Top row: regions where the absolute hydrostatic pressure is less than -0.1 bar at four time instants. The computational domain is divided to the cells of 0.2 m and time resolution is 0.1 ms. The active air guns in the arrays are shown by blue while the inactive air guns are shown by gray. Bottom row: cut sections of images shown in the top row (to visualize where the minimal pressures occur).

computational domain and the released pressure from each air gun will be scaled by the inverse of the propagation distance (geometrical spreading), for the near points to the source the pressure becomes unrealistically high. Therefore we exclude grid cells closer than 0.5 m from each air gun when calculating the pressure field from that air gun. The active and inactive air guns in the arrays are shown by blue and gray colors, respectively in Figure 2.4.

In the second row of Figure 2.4, cut sections of the figures from the top row are plotted. In the cut sections the pressure distributions inside the cavity cloud are better observed.

2.4.2 Cavity collapse

There are several approaches to model the acoustic pressure generated by cavity collapses. One way is to only consider the collapse of the cavities after they reach their maximum size and neglecting the underlying mechanism from initiation to maximum size growth. The other way, which is our approach in this paper, is to consider cavity generation, growth and subsequent collapse. We assume there are small particles, impurities or tiny bubbles in the sea water as potential nucleation sites. These nucleation sites just help the formation of cavities in the way that cavities attach to these impurities and grow. If there are multiple heterogeneities

in the water - multiple cavities will form - leading to a randomized collapse of several thousand cavities. A microbubble can exist in stable equilibrium if its radius is smaller than the Balke critical radius (Brennen, 2013). Such nucleation sites exist in the seawater with typical radii between 1 and 100 μm (Ceccio and Brennen, 1991; Brennen, 2013). In addition, the collapsing cavities themselves act as nuclei sites for continued generation of cavities and therefore the cavitation rate increases (Ceccio, 1990). As the external pressure around the nucleation site decreases, the cavity starts growing rapidly and subsequently the pressure inside the cavity decreases and molecules of water will be transferred to the cavity as water vapor. Due to rapid growth of the cavity, the pressure inside it falls below the pressure outside the cavity and therefore the cavity shrinks violently and collapses. We assume that the tiny stable bubble with radius R_0 is filled with air – or water vapor – and the initial pressure, P_0 , inside the stable free bubble (no bubble wall motion) is estimated from the following equation: (Woolf, 2001):

$$P_0 = P_{atm} + \rho g z + \frac{2\sigma}{R_0}. \quad (2.1)$$

In the above equation, $\sigma = 0.074 N/m$ is water surface tension (Nayar et al., 2014), ρ is the density of water, z is the depth where free microbubbles exist, g is acceleration of gravity, and P_{atm} is the atmospheric pressure. The response of such a tiny free stable bubble – which act as cavity nucleation site – subjected to external pressure, P , can be estimated from the following bubble dynamics equation (Prosperetti et. al., 1986):

$$\begin{aligned} & \left(1 - \frac{1}{c} \frac{dR}{dt}\right) R \frac{d^2 R}{dt^2} + \frac{4\mu}{\rho c} \frac{d^2 R}{dt^2} = \\ & - \frac{3}{2} \left(1 - \frac{1}{3c} \frac{dR}{dt}\right) \left(\frac{dR}{dt}\right)^2 - \frac{1}{\rho R} \left[2\sigma + 4\mu \frac{dR}{dt}\right] \\ & + \frac{1}{\rho} \left(1 + \frac{1}{c} \frac{dR}{dt}\right) [P_i(t) - P] + \frac{R}{\rho c} \frac{P_i(t)}{dt}. \end{aligned} \quad (2.2)$$

Here, $R(t)$ is the time dependent radius of the cavity, c is sound speed of undisturbed water, and μ is the dynamic viscosity of water. The pressure inside the cavity, $P_i(t)$, is modelled by Van der Waals equation:

$$P_i(t) = P_0 R_0^{3\kappa} (R(t))^{-3\kappa} \quad (2.3)$$

In the above equation, $\kappa = 1$ for isothermal processes, and for adiabatic processes $\kappa = 1.4$.

The magnitude of the actively emitted pressure component from a body with volume oscillations (e.g. breathing sphere, or bubble) at far-field, located at distance r from the sphere center, can be estimated by following equation (Hilgenfeldt et al., 1998; Brennen, 2013; Leighton, 2012) if the dimension of volume is much smaller than the emitted sound wavelength:

$$\begin{aligned} p(t) &= \frac{\rho}{4\pi r} \frac{d^2V}{dt^2} \\ &= \frac{\rho R(t)}{r} \left(2\dot{R}^2(t) + R(t)\ddot{R}(t) \right) \end{aligned} \quad (2.4)$$

The response of a stable microbubble with initial radius $R_0=20 \mu m$ at two different locations in the computational domain around the air gun array are subjected to the pressure changes due to the air gun array as depicted by blue dashed lines in Figure 2.5 (top row). The cavitation radius variations are estimated solving equation 2.2 by means of the Runge-Kutta method of order 5 (ode45 algorithm in MATLAB) and are shown by red solid lines in the top row. Pressure responses from cavitation collapse at $r = 1$ meter from the cavity center are estimated by equation 2.4 and plotted in the second row in Figure 2.5.

The responses of several different cavities at different locations (depths) of the computational domain subjected to the external pressures at those locations are estimated by solving the bubble dynamic equation 2.2. The maximum cavity growth, collapse time, and peak pressure from modeled cavity collapses are extracted from the simulations and plotted as a function of minimum external pressures and depth in Figure 2.6 "a" to "c", respectively. Two trends are observed: first, decreasing the external minimum pressures increases the collapse time and the cavity growth is larger. Second, for the same minimum external pressure, deeper cavities have shorter collapse times and smaller cavity radii. The collapse time increase by the decrease of the hydrostatic pressure is quantitatively in agreement with Rayleigh's (1917) equation:

$$T = 0.915 R_{max} \sqrt{\frac{\rho}{P_h}} \quad (2.5)$$

where T is the collapse time of the cavity, R_{max} is its maximum radius and P_h is the hydrostatic pressure surrounding the cavity.

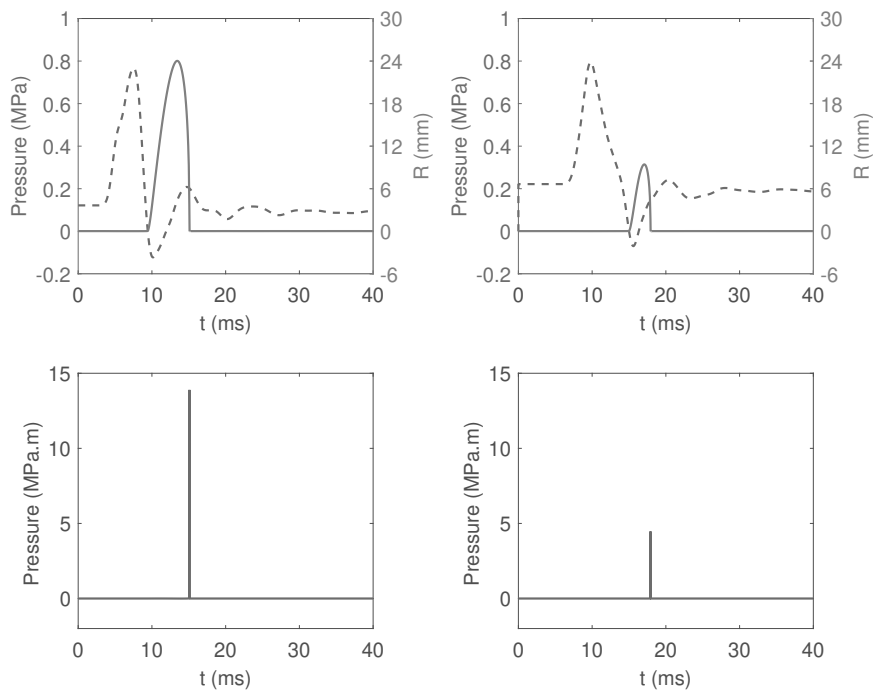


Figure 2.5: Response of a free stable bubble with initial radius ($R_0 = 20\mu m$) located at $(x = 1.2m, y = -0.1m, z = 2.2m)$ subject to simulated external pressure from air-gun arrays at that point (left) and the response of same bubble located at $(x = 1.6m, y = 0.3m, z = 12.4m)$ subject to simulated external pressure from air-gun arrays at that point (right). The external pressures are plotted with blue dashed line. The second row shows the pressure signature at 1 m from the cavity collapse in the first row.

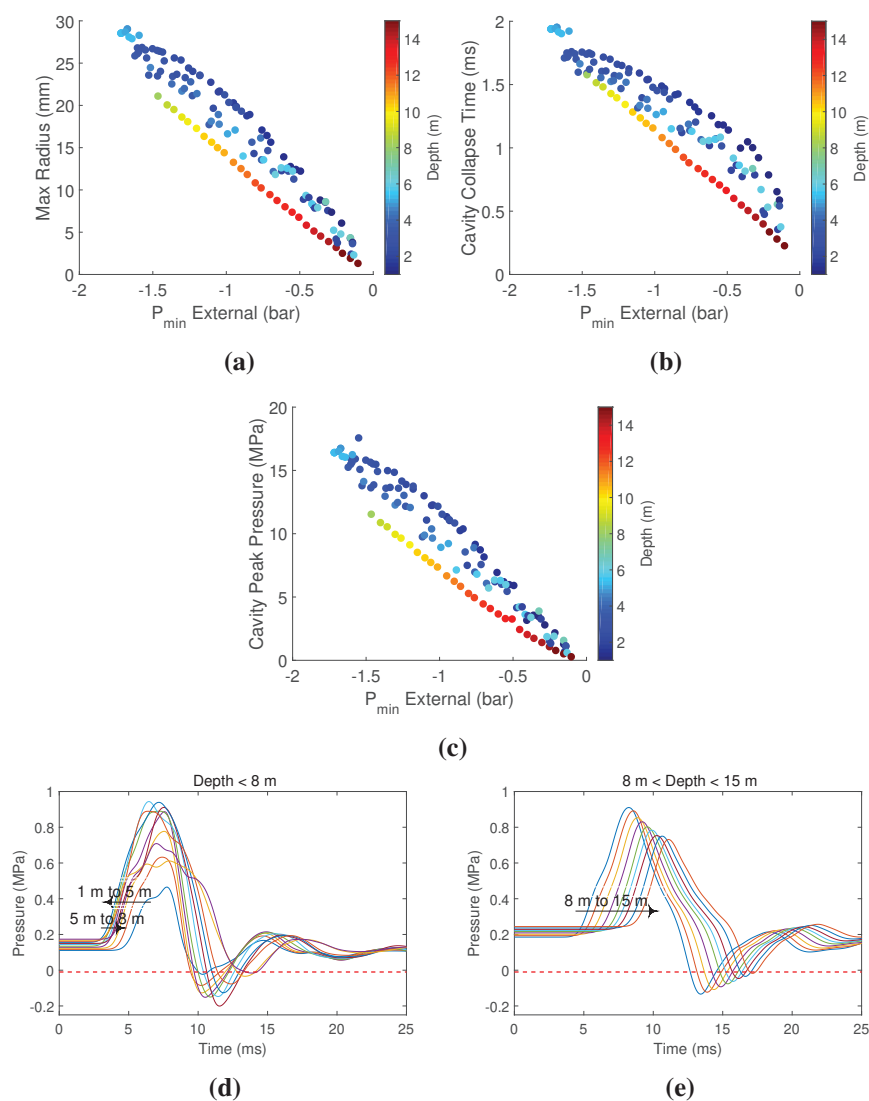


Figure 2.6: Response of a free stable bubble with initial size of $20\mu\text{m}$ at different points in the computational domain around the air-gun array subjected to external pressures from the air-gun array (and hydrostatic pressure) at that point using equation 2.2. a) maximum cavity radius growth vs. minimum external pressures at different points. b) cavity collapse time vs. minimum external pressures at different points. c) cavity peak pressure vs. minimum external pressures at different points. d) Total external pressure at some points located shallower than 8 m. e) Total external pressure at some points located deeper than 8 m. In "d" and "e" the red dashed line shows the -0.1 bar (-0.01MPa) threshold pressure.

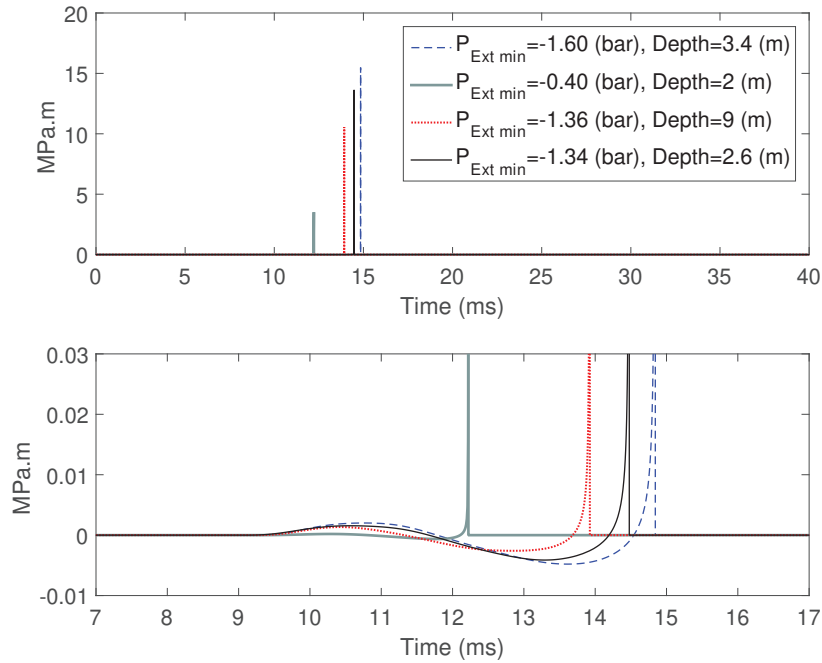


Figure 2.7: Cavity signatures at four different points in the computational domain.

It should be noted that the magnitude of minimum external pressure and the water depth are not the only factors that affect the cavity growth and collapse. Another factor is the width of the minimum external pressure. The total pressures produced by the air gun array are plotted for few points shallower than 8 m in Figure 2.6(d) and for some deeper points in Figure 2.6(e). We observe that for shallow points ($< 8\text{m}$) the shapes of the pressure curves are not similar and their minimum pressure widths are different. However the pressures at deeper points ($> 8\text{m}$) have similar shapes and practically the same width for their "minimum" main valleys. That is why the linear relation that is observed between 8 and 15 meters depth does not persist to the shallower depths (see Figures 2.6 a to c). For four different locations shown as colored dots in the above figures, their corresponding cavity signatures are plotted in Figure 2.7. To be able to compare different cavity growth and collapse signatures, the external pressures (P in equation 2.2) are shifted in a manner to have their minimum pressures at 10 ms. It is observed that the cavity starts growing around 0.4 ms before the external pressure reaches its minimum value. Furthermore, it is seen that for almost the same minimum pressure, the collapse time is shorter for deeper points corresponding to higher hydrostatic pressures.

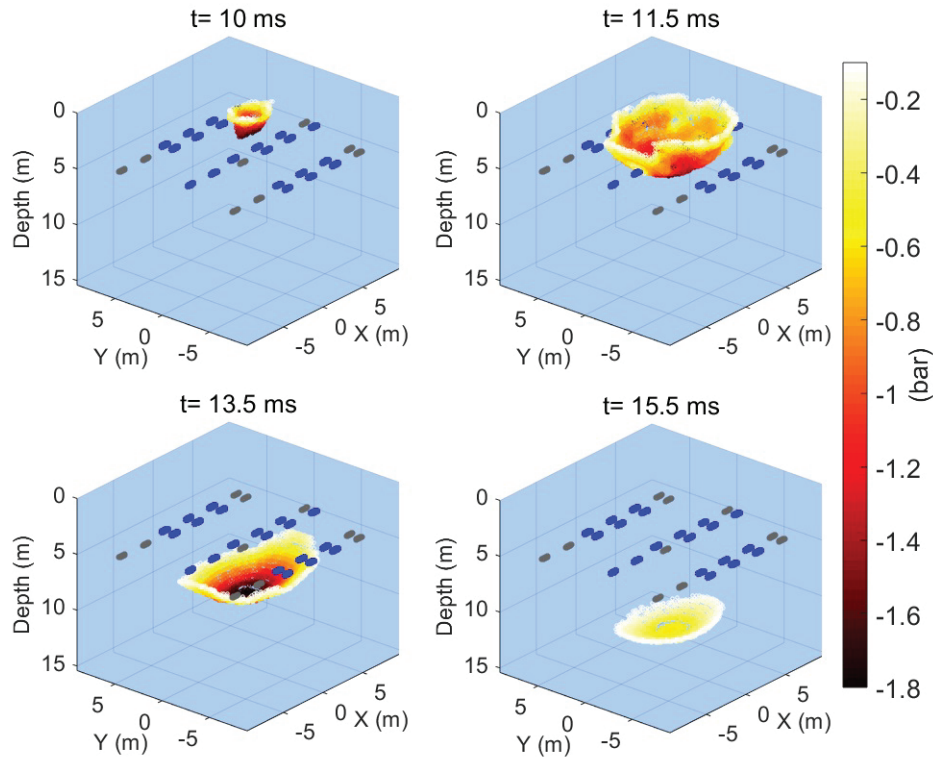


Figure 2.8: The locations in the computational domain which reach their minimum pressure at four instants of time ($t = 10, 11.5, 13.5, 15.5 \text{ ms}$). The plotting threshold was chosen to -0.1 bar .

In Figure 2.4 it is shown when and where the hydrostatic pressure drops below the assumed threshold pressure (-0.1 bar). By solving equation 2.2 and from Figure 2.5 it is observed that having the time when the external pressure reaches its minimum at each point it is required to know when the cavity starts growing and its subsequent collapse at each point within the computational domain. Spatial and temporal distributions of minimum pressures are plotted at four different time instants in Figure 2.8.

2.4.3 Propagation of cavity signatures from source to receiver

In the previous sections the temporal and spatial distribution of pressures less than -0.1 bar (the threshold pressure) and also the pressure signature from cavitation collapses at different depth and for different minimum pressures were calculated. In addition to the shape of individual cavity signatures, relative arrival time of individual signatures affects the measured signal at the receiver. The arrival time of

the signal from each cavity depends on the formation time of cavity denoted by τ , time of collapse T , and the travel time (or distances) from cavity to receiver. The term $1/r$ represents geometrical spreading. In other words, spatial and temporal distributions of cavities affect the shape of measured signal at the receiver. Absorption effects are included in our model since the signal generated by the cavity has a high frequency content. Absorption, γ (Neper/m) is calculated from the equation given by Francois and Garrison (1982). In the model three different dissipation mechanisms are considered: (i) viscosity of pure water which is effective at high frequencies, (ii) relaxation of magnesium sulphate molecules which is dominant at frequencies below 100 kHz, and (iii) relaxation of boric acid molecules which is significant at frequencies below 1 kHz. The effect of the i th cavity bubble recorded by the hydrophone is given by u_i and is obtained by the following formula:

$$u_i(t, r) = \frac{1}{\sqrt{2\pi}} \int_{-\infty}^{+\infty} \left(S_i(f) \cdot e^{-\gamma(f)r_i} \cdot e^{-j2\pi f\tau_i} \cdot \frac{e^{-j\frac{2\pi f}{c}r_i}}{r_i} \right) e^{j2\pi ft} df \quad (2.6)$$

Here $S_i(f)$ is the frequency domain representation of the time signal from the collapse of the i^{th} cavity and $j = \sqrt{-1}$ is the imaginary unit. The distance of the cavity from the hydrophone is r_i and its formation time is τ_i . We have used MATLAB to calculate the inverse Fourier transform in equation 2.6. After having the effect of each cavity, the total effect is obtained by linear superposition, as suggested by Harrison (1952), and denoted by y_t :

$$y_t(t, r) = \sum_{i=1}^N u_i. \quad (2.7)$$

In equation 2.7, N is the number of grid points for which pressure reaches its minimum and is smaller than the assumed threshold for cavity initiation.

2.5 Results

Ghost cavity cloud signals are simulated by considering the aggregate effects of the collapse of individual cavities in the receiver location. The method is summarized by the following steps:

Step 1. Cavities growth initiation times are required. Therefore we need to know at each grid point in the computational domain, at what time the pressure reaches its minimum and whether its magnitude is below assumed threshold pressure (-0.1 bar) for cavity generation. This information is depicted in Figure

2.8 at four time instants. We have such information for every 0.1 ms from the simulation.

Step 2. The cavity signature at each point is selected based on the magnitude of negative pressure obtained in (step 1) and its depth from a cavity signature library (Figure 2.6 and Figure 2.7).

Step 3. Such cavities are propagated from where they are formed to the receiver point. Absorption and geometrical spreading is included in propagation from source to receiver as explained in section III.C.

In the following we have assumed two cases: 1) no interaction between cavities. This is called Model 1. And 2) Pressure interaction between the cavity collapses which is called Model 2. From an implementation point of view, the difference between the two models is in step 2. In Model 1, cavities are selected directly based on the magnitude of minimum pressure in step 1. In the second case, cavity signatures are selected based on a weighted magnitude of minimum pressures given in step 1. The weighting is based on the simple model that as the time passes the pressure from collapses of cavities elevate the minimum pressure given in step 1.

2.5.1 Model 1 - No interaction between cavities

In this case it is assumed that there is no effect from the former cavity collapses on the later ones. Thus, the cavity signature at each point is selected directly based on the minimum pressure at that point and the depth information without further manipulation. The 10 kHz HP filtered simulated ghost cavitation signal for shot 20 together with the far-field signature from air guns array and its LP filtered signal are plotted in Figure 2.9.

2.5.2 Model 2 - With pressure interaction between cavities

The cavity interaction is included based on the assumption that collapses of initial cavities produce intense pressures which increase the hydrostatic pressure around cavities that are formed later. Therefore, the collapse time and growth of the cavities that are formed at later times are reduced. This can be justified by modifying the Rayleigh cavity collapse time equation:

$$T = 0.915R \sqrt{\frac{\rho}{P_h + \sum_{i=1}^N P_i}}. \quad (2.8)$$

The summation of pressures in the denominator of equation 2.8 models the effects

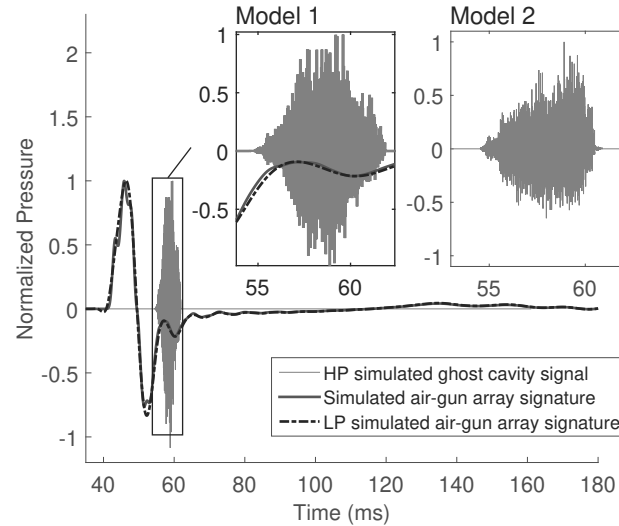


Figure 2.9: Simulated air-gun far-field signature and its LP filtered signature together with the 10 kHz HP filtered simulated ghost cavity signal for shot 20 using model 1. Simulated 10 kHz HP filtered signal for shot 20 by assuming pressure interaction between cavities is also plotted (model 2). All signals are normalized.

of cavity collapses which is analogous to the pressure field interactions in an air gun array (see equation 8 in Ziolkowski et al. (1982)). Therefore, in this part it is assumed that cavities that are generated at earlier time are formed only due to the external pressure from air gun array and are not affected by other cavity collapses. While the cavities that are formed at later times are more and more affected by previous cavities and consequently they grow less, have shorter collapse time and less intense peaks. In this model, at the beginning (during the first 0.5 ms) of ghost cloud formation cavities are selected solely based on the estimated pressure drops from air gun array and as the time passes the collapse time of cavities (and their growth) that are formed later are decreased gradually. Then it is assumed gradually collapse time decreases by 50% and then 80% at the end of process compared to the case without any pressure interaction between cavities. These values for the model are obtained after few trial and errors. The results for 10kHz HP-filtered simulated signal for shot 20 is shown in Figure 2.9.

Using the 5 ms after peak time of LP filtered array signature as reference for ghost cavitation signal (the same reference as in field measured data), normalized cumulative energies of 10 kHz HP filtered signal from field measurement and simulation from Model 1 and 2 for shot 20 are plotted in Figure 2.10 (top) and the absolute

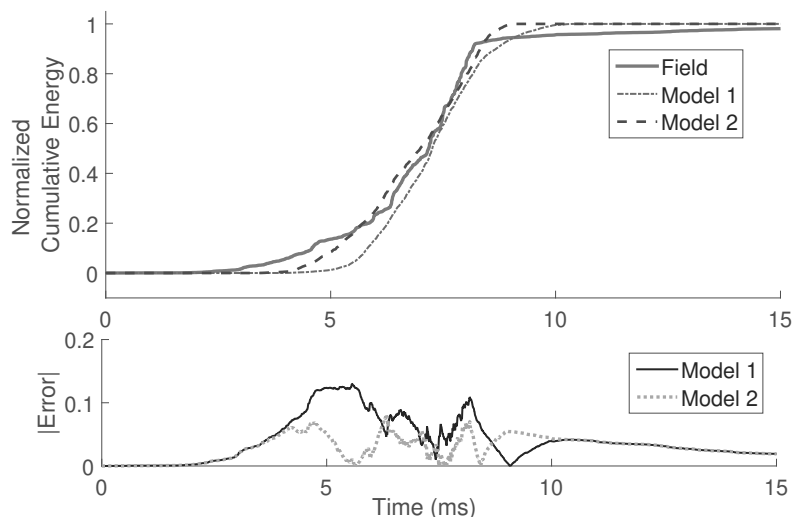


Figure 2.10: Top panel: Normalized cumulative energies of 10kHz HP filtered simulated signal from Model 1 and Model 2. Bottom panel: The absolute value of the difference between normalized cumulative energy curves of field data and the two models.

value of difference between two models is plotted underneath of same figure. It is observed that there is a good match between simulation results and field measurement. However, for Model 1, the shape of HP filtered simulated ghost cavitation signal (Figure 2.9) does not resemble the shape of measured field data. Compared to Model 1, it is observed that Model 2 has better agreement with the field data. The normalized cumulative energy from Model 2 fits well with the field data from around 15% to 90% energy accumulation curve of the field data. In addition, the envelope of simulated signal from Model 2 has skewness which better agrees with the skewness of HP filtered signal's envelopes from field experiment.

Figure 2.11 shows a comparison between normalized HP filtered simulated signals (left) and measured signals (right) for shots 15 to 20.

There is an interesting skewness of the envelope of both the modeled and measured signatures in Figure 2.11, as pointed out by Landrø et al. (2016). There are several factors that must be taken into account to explain this skewness. Those factors include dimensions of the cloud, size and number of cavities, the downward speed of the cavitation cloud (see Figure 2.4) and the relative location of the receiver to the cavitation cloud. Both size and number of cavities are maximum at the shallower depths (< 5 m) and as the cavitation cloud moves downwards, the distance between cavities and receiver decreases and therefore weaker signals that are formed later

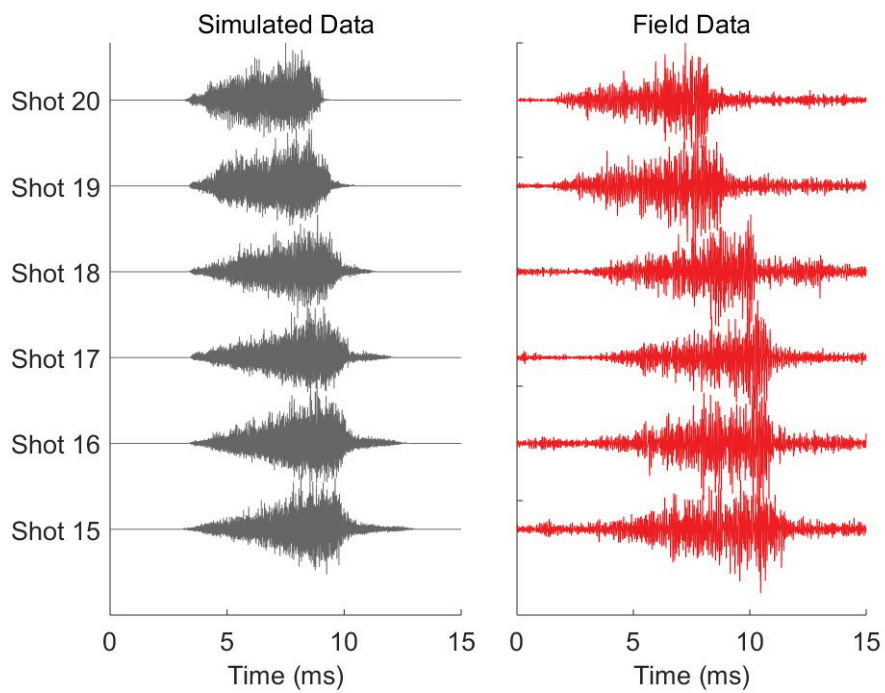


Figure 2.11: Simulated (left) and field experiment (right) 10 kHz HP-filtered signal for different shot numbers 15 to 20 from model 2. The shot receiver configuration is shown in Figure 2.1 (top). The signals are selected 5 ms after the first main peak of LP filtered array signature.

are received by the hydrophone a little earlier than the cavities generated at shallower depths. In addition, the collapse time of each cavity increases linearly with radius (equation 2.5). Hence we see that the signal "swells" to its maximum and then vanishes much more quickly.

The duration of the ghost cavitation signal increases as the incident angle (measured relative to the vertical line) increases. This effect is mainly caused by the finite extension of the cavity cloud. The width of the signal increases from approximately 6 ms for shot 20 to 7.5 ms for shot 15.

2.6 Discussion and conclusions

We have developed a modeling scheme that incorporates the creation of water vapor cavities due to acoustic stimulation by multiple ghost reflections from air guns that are fired simultaneously when marine seismic data are acquired. The first modeling step is to model the low-frequency signal of an air gun array. The theory for this is well known, and we use this first modeling step to determine the spatial and temporal distribution of regions where cavities are likely to occur. When the acoustic signals from several air guns are reflected from the sea surface, simple superposition is used to calculate the pressure at a given water depth. Using this linear superposition principle predicts some regions to have negative absolute pressure values. This means that the linear theory breaks down, and as a simple solution, we assume that cavities are formed when the linear acoustic theory breaks down. By assuming that cavities are formed at locations where this happens, we model multiple cavities. In the current version we assign one cavity to each grid point in the computational domain. In the present examples we have used a grid size of 0.2 m. This is an assumption, and the number of cavities can be increased by decreasing the grid size. The cavity growth and collapse are modeled using the Keller bubble dynamic equations. It is assumed that a cavity starts growing when the pressure around it reaches the minimum value (we used -0.1 bar in our examples). The basic assumption is that there are infinitesimal impurities in the water, which act as nuclei for cavity growth. When the output acoustic signal from one single cavity is modeled, geometrical spreading is included by multiplication of the inverse source-receiver distance. Absorption effects are included by using a simple Q-model, where Q-values are calculated by the equation given by Francois and Garrison (1982). We find that the maximum cavity radius increases close to linearly with the modeled minimum pressure. In addition to this trend, there is a weaker trend related to the depth of the cavity: shallow cavities have a slightly larger maximum radius than the deeper. The cavity collapse time follows Rayleigh's equation. In our modeling we have not included the effect of transmission losses and ray bending due to the presence of a cavity cloud. Especially if

the cloud is dense, such effects might alter our modeling results significantly, both with respect to travel-time and amplitudes. In addition, more sophisticated cavity interaction models will be investigated further in the future. The results indicate a good correspondence between modeled and measured high frequency signals. By correspondence we here mean similar envelope of the chaotic high frequency signal, not details corresponding to the collapse of single cavities. Accounting for interaction between cavities by assuming that the radiated pressure from all other cavities are changing the hydrostatic pressure surrounding one cavity improves this correspondence. The onset time and the duration of the high-frequency cavitation signal fits reasonably well between modeled and measured data. The modeled average maximum cavity radius is 9.8 mm for the initial model and it is 3.9 mm for the model with cavity interaction. In this work we have compared modeled and measured high frequency signals after normalizing. A calibration step could involve a scaling of the modeled signature from individual cavity collapses and/or adjusting the number of cavities. In the current modeling example we used a relatively high number of cavities, assuming that each grid point fulfilling the minimum pressure threshold hosts a cavity. However, there is obviously a tradeoff between the strength of each cavitation signal and the number of cavities. We suggest that our model can be used to design seismic air gun arrays which produce less high-frequency signals.

2.7 Acknowledgment

This research is funded by Research Center for Arctic Petroleum Exploration (AR-CEX) partners, and the Research Council of Norway (grant number 228107). The reviewers are acknowledged for their constructive comments and invaluable suggestions.

Chapter 3

High frequency ghost cavitation —a comparison of two seismic air-gun arrays using numerical modelling¹

Babak Khodabandeloo, Martin Landrø

*Department of Petroleum Engineering and Applied Geophysics,
Norwegian University of Science and Technology (NTNU)
NO-7491 Trondheim, Norway*

3.1 Abstract

Ghost cavitation is probably the mechanism behind the majority of high frequencies (above 5 kHz) generated by seismic air-gun arrays. Such high frequencies are less important in seismic reflection imaging. High frequency sound might impact marine fauna and particularly marine mammals. In this paper the array signatures and high frequency ghost cavitation signals for two different arrays are simulated using numerical modelling. It is observed that one array has slightly more (20%) energy within the seismic frequency band (1-100 Hz) but emits significantly more energy (150%) for frequencies above 5 kHz.

¹Paper Published in *Energy Procedia*, 125, pp.153-160.
DOI: <https://doi.org/10.1016/j.egypro.2017.08.158>

3.2 Introduction

Underwater ocean noise generated by human activities has increased over the last century. Seismic surveys besides shipping, military activities, and pile driving, are one of the major man-made underwater acoustic noise sources (Hildebrand, 2009). Cetaceans use acoustic waves for several essential purposes including finding prey, mating, social interaction, and avoiding predators (Wright et al., 2007). There are widespread and increasing concerns regarding the adverse impacts of anthropogenic underwater acoustics on marine mammals which include physical and physiological effects, acoustic masking, behavioral reactions, and chronic stress effects (Richardson et al., 1995; NRC, 2003; Gordon et al., 2003). There are evidences of both short- and long-term behavioral changes as a result of elevated background noise. Measurements indicate that right whale calls have shifted to higher frequencies within around three decades (Parks et al., 2007) which is related to the increased noise in the frequency band of their calls. Other measurements have shown a correlation between the amount of stress hormones in whales and underwater noise (Rolland et al., 2012). Behavioral disturbances were observed in different marine mammals subjected to the noise from seismic air-guns, and it was more pronounced in smaller species (Stone et al., 2006). During and after the end of exposure to naval sonar signal, the feeding behavior of humpback whales was interrupted (Silve et al., 2016). As a result of operating seismic survey there was observed both increase and decrease in fish catch rates (Løkkeborg et al., 2010). The increase in catch rate is attributed to the elevated swimming activities that can be an indicator of increase stress due to seismic shooting which in the long run may result in reduce in catch rate. To extract the information about geological structure beneath the seabed, marine seismic reflection profiling is used. In marine seismic surveys an active source is used to generate acoustic waves that propagate into the Earth. Acoustics waves reflected at interfaces between layers with different seismic velocities are recorded by hydrophones embedded within long streamers towed behind a seismic vessel or by geophones located at the seabed. Air-gun arrays, marine vibrators and water-guns are the main marine seismic sources (Duren, 1998; Barger and William, 1980). Among them, however, air-gun arrays are by far the most common and efficient seismic sources (Watson, 2016). Air-guns generate impulsive acoustic waves by discharging highly pressurized air into the surrounding water (Caldwell and William, 2000). An air-gun array contains several (typically 12 to 48) individual air-guns. The purpose of using air-gun arrays, instead of a single air-gun, is to increase the source strength, to focus the acoustic pressure signal in the vertical direction, and to damp unwanted bubble oscillations (that occur after the primary acoustic signal) to improve the source signature (Dragoset, 2000). Air-gun arrays generate broad-band acoustic waves from a few Hz up to

tens of kHz (Goold, and Peter, 1998; Landrø et al., 2011). Only low frequencies (< 100 Hz) are useful for deep seismic imaging since they penetrate deeper into the Earth. Even though high frequencies (>1000 Hz) can be used to detect gas leakage from a CO₂ storage site or an oil and gas production field (Landrø et al., 2017), such higher frequencies are mostly considered as waste energies and are filtered out prior to the processing step (Ronen et al., 2015). Considering hearing curves of marine mammals it can be inferred that the emitted high frequencies from air-gun arrays may have negative impact on several cetacean species, as for instance toothed whales (Landrø et al., 2011; Ketten, 2004). There are several underlying mechanisms for high frequency generation related to air-gun arrays. To reduce the high frequencies attributed to steep rise time of pressure waves of each individual air-gun a new air-gun has been designed and tested (Coste, 2014; Gerez, 2015). Interaction between reflected ghost wave and air-gun bubble also generates frequencies between 400 and 600 Hz (King et al., 2015; King, 2015). In air-gun arrays, another underlying mechanism for generating frequencies up to tens of kHz is called ghost cavitation (Landrø et al., 2011). Recording the far-field signals from marine seismic air-gun arrays using broad band hydrophones it was observed that full air-gun arrays signals contain high frequency signal which appears few milliseconds after the ghost signal (Landrø et al., 2013; Landrø et al., 2016). Reflected ghost signals from individual air-guns in the array "add up" and drop the absolute hydrostatic pressure to zero in some locations for a short time. In such regions cavities can grow and their subsequent collapse generates intense noise. Using numerical modelling ghost cavitation hypothesis was further validated (Khodabandeloo et al., 2017). Numerical modelling results indicate that ghost cavitation signal contains low frequencies in addition to the high frequencies (Khodabandeloo and Landrø, 2017). In this paper the array signature and high frequency ghost cavitation signal from two air-gun array configurations are numerically simulated. The array configurations are compared with regard to their useful seismic frequency band and the undesired waste high frequencies generated by ghost cavitation phenomena. It is shown that selection and arrangement of individual air-guns in the array can be optimized to reduce the waste high frequencies without compromising the low frequencies that benefits seismic imaging.

Nomenclature

R	time dependent radius of cavity (m)
t	time (s)
P	external pressure (Pa)
P_i	pressure inside the cavity (Pa)
ρ	water density (kg/m^3)
c	water sound speed (m/s)
σ	water surface tension (N/m)
μ	dynamic viscosity of water ($N \cdot s/m^2$)
$S_i(f)$	frequency domain representation of the time signal from the collapse of i^{th} cavity
γ	absorption (Neper/m)
f	frequency (Hz)
r	distance between cavity and propagation location (m)
u_i	time signal from the collapse of i^{th} cavity
y	ghost cavitation signal
N	number of cavities
E	energy of signal

3.3 Ghost cavitation signal modelling

An air-gun array includes several individual air-guns usually with different air chamber sizes. A full array has usually two to three sub-arrays. Acoustic pressure signal from a single air-gun modelled by the NUCLEUSTM source modelling package (Petroleum Geo-Services) is shown in Figure 3.1. The first peak is the direct arrival primary pulse and the other peaks are formed due to the air bubble oscillations. In an air-gun array the notional source signature from each air-gun is influenced by the acoustic pressure of the other air-guns as well.

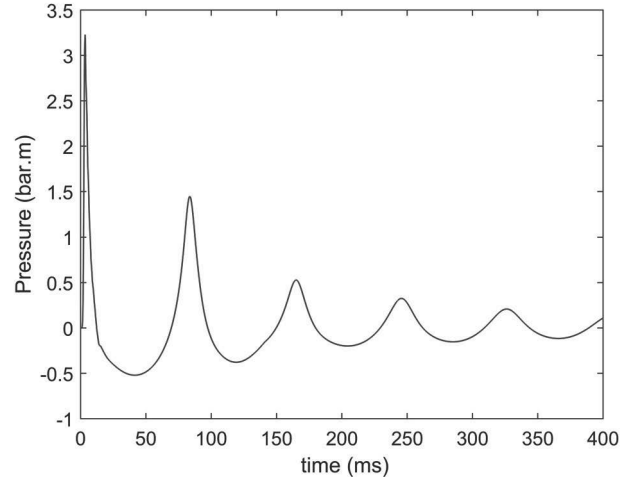


Figure 3.1: Notional source signature of an individual air-gun simulated by NUCLES™ (PGS).

Numerical modelling of the ghost cavitation signal from an air-gun array is explained in (Khodabandloo et al., 2017) and can be summarized in four steps:

Step 1: Spatial and temporal distributions of regions where the pressure drops below certain threshold level. Air-gun modelling is used to find the emitted acoustic pressure from each individual air-gun in the array.

Step 2: Using bubble dynamics equations (Prosperetti and Lezzi, 1986), the cavity growth and its subsequent collapse due to sudden pressure drop is estimated:

$$\begin{aligned}
 & \left(1 - \frac{1}{c} \frac{dR}{dt}\right) R \frac{d^2 R}{dt^2} + \frac{4\mu}{\rho c} \frac{d^2 R}{dt^2} = \\
 & - \frac{3}{2} \left(1 - \frac{1}{3c} \frac{dR}{dt}\right) \left(\frac{dR}{dt}\right)^2 - \frac{1}{\rho R} \left[2\sigma + 4\mu \frac{dR}{dt}\right] \\
 & + \frac{1}{\rho} \left(1 + \frac{1}{c} \frac{dR}{dt}\right) [P_i(t) - P] + \frac{R}{\rho c} \frac{dP_i(t)}{dt}.
 \end{aligned} \tag{3.1}$$

The emitted acoustic pressure due to cavity growth and collapse at the far-field at the distance r from the cavity is estimated by the following equation (Brennen, 2013; Leighton, 2012):

$$P_i(t) = P_0 R_0^{3\kappa} (\dot{R}(t))^{-3\kappa}. \quad (3.2)$$

In the above equation the superposed dot indicates a time derivative.

Step 3: Each individual cavity signature is propagated to the receiver location. Geometrical spreading and absorption are included, as follows:

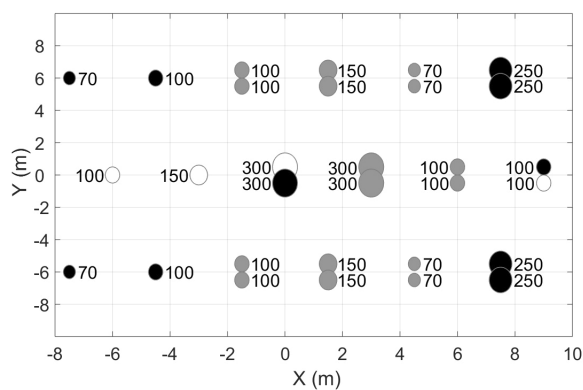
$$u_i(t, r) = \frac{1}{\sqrt{2\pi}} \int_{-\infty}^{+\infty} \left(S_i(f) \cdot e^{-\gamma(f)r_i} \cdot e^{-j2\pi f \tau_i} \cdot \frac{e^{-j\frac{2\pi f}{c} r_i}}{r_i} \right) e^{j2\pi t f} df \quad (3.3)$$

Step 4: The ghost cavitation signal is formed by adding acoustic signatures from individual cavities:

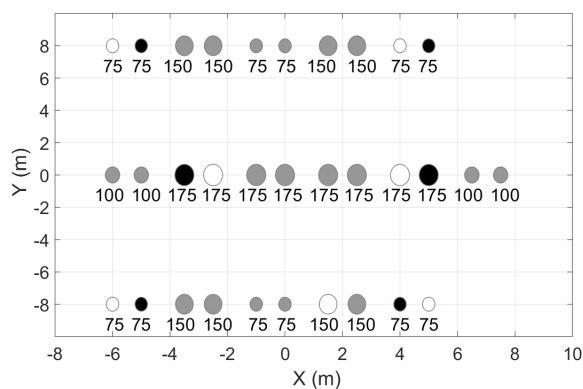
$$y_i(t, r) = \sum_{i=1}^N u_i. \quad (3.4)$$

3.4 Two air-gun arrays configurations

The configuration of two different air-gun arrays is shown in Figure 3.2. Both arrays consist of three sub-arrays. The first air-gun array is shown in Figure 3.2(a) and hereafter is called array 1.



(a)



(b)

Figure 3.2: (Two air-gun array configurations. Circles indicate individual air-guns in the array and the numbers show the air chamber volume of each air-gun. White, gray, and black colors indicate single air-gun, cluster, and inactive air-guns, respectively. (a) Array 1, with 6 meters subarray separation and total volume of 2730 in^3 ; (b) Array 2, with 8 meters subarray separation and total volume of 3250 in^3 .

The distance between the sub-arrays is 6 meters for array 1, and the corresponding separation distance is 8 meters for array 2. The volume of active air-guns for array 1 is 2730 in^3 and 3250 in^3 for array 2.

3.5 Results

For the two array configurations the regions around each array that the pressure drops below the selected threshold pressure (-0.1 bar) are numerically simulated (step 1 in section 2). The results are plotted at four time instants in Figure 3.3

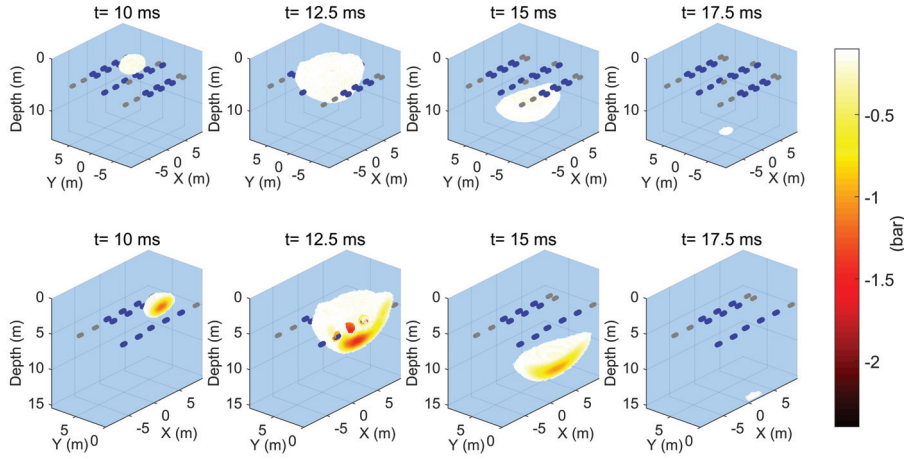


Figure 3.3: Top row: regions where the absolute hydrostatic pressure drops the threshold pressure (-0.1 Bar) at four time instants for array 1. The active air-guns and inactive ones in the array are shown by blue and gray, respectively. Bottom row: cut sections of images shown in the top row.

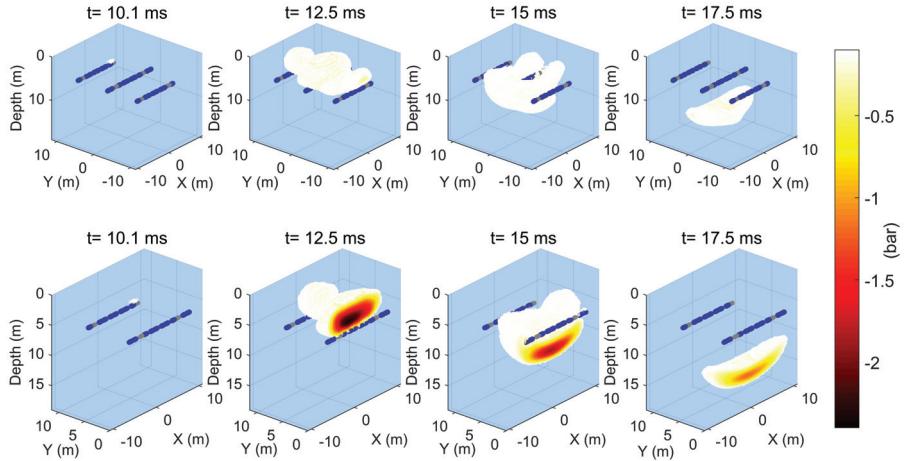
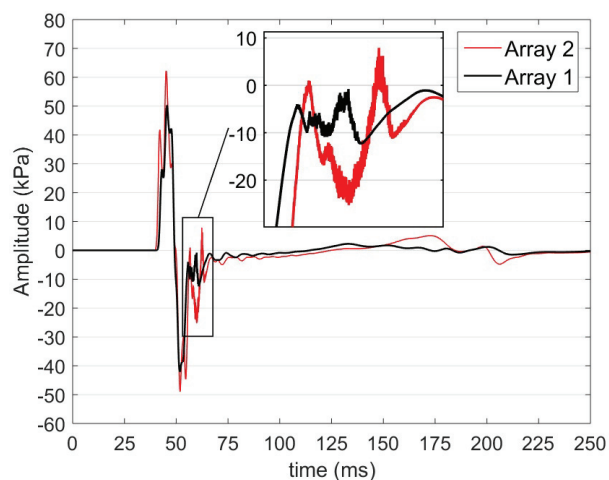


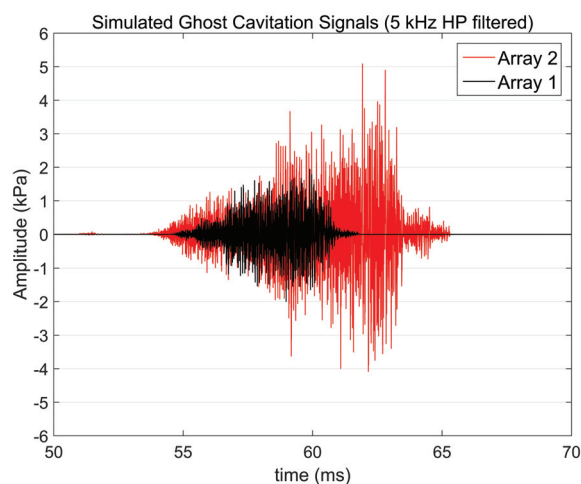
Figure 3.4: Top row: regions where the absolute hydrostatic pressure drops the threshold pressure (-0.1 Bar) at four time instants for array 2. The active air-guns and inactive ones in the array are shown by blue and gray, respectively. Bottom row: cut sections of images shown in the top row.

Thereafter, for both of the array configurations, the array signatures (including the

ghost cavitation signal) are plotted in Figure 3.5(a). These signals are simulated for a location 55 meters vertically below each array and with 40 meters offset. In Figure 3.5(b), 5 kHz high passed (HP) filtered signals are plotted for array 1 and 2. Such high frequencies are generated by the ghost cavitation phenomena. It is seen that the maximum amplitude of the HP filtered signal for array 2 is almost 2.5 times more compared to array 1.



(a)



(b)

Figure 3.5: (a) Computed array signatures for array configurations 1 and 2. No filter applied; (b) 5 kHz HP filtered signals for the same signals shown in (a). Notice the stronger and longer ghost cavitation signal for array 2.

Energy spectrums of both signals shown in Figure 3.5(a) are plotted in Figure 3.6. It is clear that array 2 generates more high frequencies (>5 kHz) while it has only slightly higher energy level in the seismic frequency range. The energy level of array 2 is around 10 dB higher than array 1 in almost the whole frequency range between 5-70 kHz.

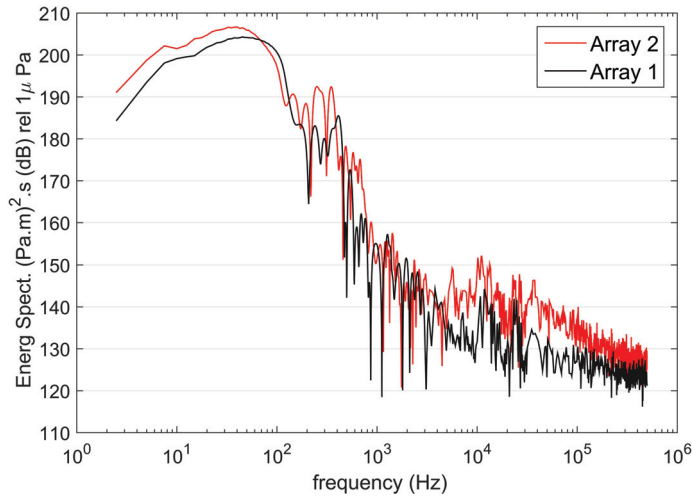


Figure 3.6: Energy spectrum of simulated signals for array 1 and array 2 shown in Figure 3.5(a). Above 3 kHz the graphs are smoothed.

Energies of the signals at different frequency bands for both arrays are compared in Figure 3.7. The energies are used instead of RMS values since for transient signals the RMS will be influenced by the selected time duration. The energy is defined as:

$$E = \sqrt{dt \times \sum_{i=1}^N x_i^2}. \quad (3.5)$$

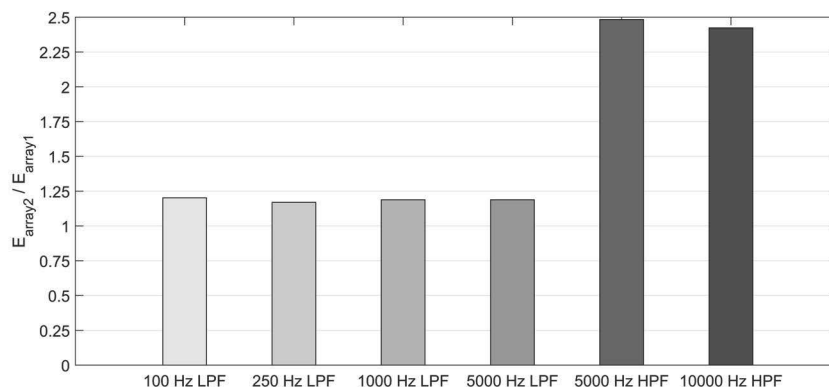


Figure 3.7: Ratio of energy levels for array 1 and 2 at different frequency ranges. (LPF: Low Passed Filtered; HPF: High Passed Filtered).

In Figure 3.7 the energy of both arrays are compared at different frequency ranges. It is observed that the energy of array 2 at low frequencies (<100 Hz) which benefits the deep seismic imaging is around 20

3.6 Discussion and conclusions

Numerical simulation is used to simulate the high frequency ghost cavitation signal as well as the source signature for two different seismic air-gun arrays. Both arrays have three sub-arrays and in one of them the sub-arrays are separated by 6 meters while in the other one the separation distance is 8 meters. Total air chamber volumes for the two arrays are 2730 in³ and 3250 in³, respectively. Even though the sub-array distance in the larger array is more, the air-guns in each of its sub-array are located closer to each other and have more uniform distributions. It is observed that both the peak amplitude and beneficial low frequency (<100 Hz) energy content of the larger array for deep seismic imaging is approximately 20 % more than the smaller array. However, it emits around 150 % more high frequency (> 5 kHz) energy. The duration of the high frequency signal for array 2 is around twice as much compared to array 1. Hence, the smaller array configuration is regarded to be more environmental friendly. We suggest that numerical simulation can be used to select and arrange air-gun arrays in order to reduce the amount of unwanted high-frequency signals.

3.7 Acknowledgements

This research is funded by Research Center for Arctic Petroleum Exploration (AR-CEX) partners, and the Research Council of Norway (Grant No. 228107). Statoil

grant for publication is also gratefully acknowledged.

Chapter 4

Acoustically induced cavity cloud generated by air-gun arrays — comparing video recordings and acoustic data to modeling¹

Babak Khodabandelo

*Department of Geoscience and Petroleum,
Norwegian University of Science and Technology (NTNU)
NO-7491 Trondheim, Norway*

Martin Landrø

*Department of Electronic Systems
Norwegian University of Science and Technology (NTNU)
NO-7491 Trondheim, Norway*

4.1 Abstract

For seismic air-gun arrays, ghost cavitation is assumed to be one of the main mechanisms for high-frequency signal generation. Ghost cavitation signals are weak for seismic frequencies (<300Hz) and do not contribute to seismic reflection profiling. In the current experiment, the ghost cavity cloud is monitored by a high-

¹Paper Published in *the Journal of the Acoustical Society of America*, Volume. 143, Issue 6 (June 2018), 3383-3393. DOI/10.1121/1.5040490

speed video camera using 120 frames per second. This is, as far as we know, the first convincing photographic evidence of ghost-induced cavitation. In addition to video recording, acoustic signals were recorded with a sampling rate of 312.5 kHz using broad-band hydrophones suspended 17 m below the array. The pressure drop around the source array is estimated using air-gun modeling followed by a phenomenological modeling of the growth and collapse of each vapor cavity. The cumulative effect of cavity collapses is modeled based on linear superposition of the acoustic signals generated by individual cavities. The simulated acoustic ghost cavitation signal and the corresponding cavity cloud show good agreement with the field data.

4.2 Introduction

In marine seismic reflection profiling where the geological structure beneath the seabed is delineated, marine seismic sources such as air-guns, water-guns, and marine vibrators are used (Duren, 1988). The objective of such exploration surveys is usually to find hydrocarbon resources. Other applications are academic research and mapping of Earth's subsurface. By far, air-gun arrays have been the most prevalent and efficient marine seismic source (Duren, 1988; Barger and Hamblen, 1980) and still are (Watson, et al. 2016). An air-gun generates acoustic pressure waves from expansion and contraction of an air bubble which is formed by releasing high-pressure air (typically 2000 psi) into the surrounding water within a short time (Caldwell and Dragoset, 2000). Instead of using a single air-gun, several air-guns with different air chamber volumes are arranged in arrays and fired simultaneously to produce and direct an intense pulse towards the seabed (Dragoset, 2000). It is the low-frequency band (<300Hz) that is analyzed in seismic reflection profiling (Caldwell and Dragoset, 2000) and hence ideal air-gun arrays should produce acoustic pressure waves containing all energy concentrated below 300 Hz. However, measurements with broadband hydrophones have revealed that the acoustic signal from air-gun arrays contains frequencies up to tens of kHz (Goold and Fish, 1998; Tashmukhambetov et al. 2008; Landrø et al. 2011; Guan et al 2015). Such high frequencies are much weaker than the low-frequency parts and do not benefit seismic imaging, but they can be used for example to detect targets of size between 0.5 to 20m in the water column (Banda and Blondel, 2016) or for detection of potential gas leakage from an oil and gas production field or a CO₂ storage site (Landrø et al., 2017). These high frequencies might impact cetacean species that are sensitive to acoustic signals in the high-frequency range (10-150 kHz) (Ketten, 2004; Landrø et al., 2011). Several mechanisms are responsible for high-frequency acoustic wave generation by air-gun arrays. The rapid movement of air from the air-gun into the water generates some amount of high frequencies. To reduce these high frequencies, a new air-gun has been designed and tested

(Coste et al., 2014; Gerez et al., 2015) which releases the pressure over a longer time period compared to standard air-guns and hence the signature has a gentler slope and the peak amplitude is reduced (Groenaas et al., 2016). To reduce the high-frequency generation due to the steep rise time of pressure, another solution is to use sources with lower operating pressures and larger volumes (Chelminski, 2015). For example, the tuned pulse source has a large air chamber filled with low-pressure air and generates acoustic pulses with long rise times (Ronen and Chelminski, 2017). King et al. (2015) and King (2015) suggest that the reflected ghost pressure wave from the sea surface interacts with the air-gun bubble and give rise to high frequencies between 400-600 Hz. Another mechanism related to air-gun arrays which generates high frequencies up to tens of kHz is the ghost cavitation phenomena (Landrø et al., 2011). Landrø et al. suggest that a cavity cloud is formed by the hydrostatic pressure drop in some locations around the array: acoustic pressures from individual air-guns in a marine seismic air-gun array are reflected from the water-air interface with negative polarity. Constructive interference of the sea-surface reflected acoustic waves “add up” and the absolute hydrostatic pressure drops close to zero in some regions which results in water vapor cavity growth and subsequent collapses (Landrø et al., 2013; Landrø et al., 2016). This phenomenon was numerically modeled based on air-gun modeling and bubble dynamic equations (Khodabandeloo et al., 2017). Air-gun modeling (Ziolkowski et al., 1982) is used to obtain notional source signatures of individual air-guns in the array. Using linear superposition of the pressure generated by individual air-guns, the temporal and spatial distribution of regions where the pressure is close to or below zero are determined. Afterward, Prosperetti bubble dynamics equations (Prosperetti and Lezzi, 1986) are used to estimate vapor cavity growth and collapse. The signal from collapse of several single vapor cavities within the cloud will also generate a low-frequency response (Khodabandeloo and Landrø, 2017a) in addition to the high frequencies. The strength and energy of the high-frequency ghost cavitation signal can actually be decreased while the energy in the useful frequency band increases. This depends on the configuration of the air-gun array (Khodabandeloo and Landrø, 2017b). Essentially, the ghost cavitation can be reduced by increasing the distance between the guns (Landrø et al., 2016). Liquids are prone to cavity formation and subsequent collapse where they experience pressure drop below the vapor pressure or partial pressure of dissolved gases (Mellen, 1954; Plesset, 1970). Acoustic cavitation is the term used for the vapor cavity induced due to the oscillating pressure when an acoustic wave propagates through a liquid (Frohly et al., 2000; Apfel, 1984). In the case of pure water and in the absence of impurities or cavitation nuclei, there is a very high negative pressure (~ -26 MPa) required to rupture the water and form the cavity (Caupin and Herbert, 2006; Herbert et al., 2006). Availability of cavity nuclei facilitates the

cavity generation (Apfel, 1984; Brennen, 2013). This is shown in a Venturi nozzle experiment (Harrison, 1952) and an experiment by seeding cavities by electrolysis (Arakeri and Shanmuganathan, 1985) where it is observed that undissolved air bubbles with the size of typically $50 \mu m$ are excellent cavitation nuclei sites. It is estimated that microbubbles with the size between $18 \mu m$ to $350 \mu m$ are uniformly distributed down to 36 m depth in seawater at around 6 knots wind speed (Medwin, 1977). Several experiments demonstrate that the collapse of cavity bubbles produce intense noise and damage (Kim et al., 2014; Reisman and Brennen, 1996; Franc and Michel, 1988). In some cases, it is valid to neglect the influence of a bubble on the neighboring bubbles. Then the resulting acoustic signal generated by several bubbles is simply equal to the sum of the acoustic pressure generated by individual cavities (Harrison, 1952). In the case of coherent cavity collapses within the cloud, the noise and damage are greater than expected from a random cumulative effect of individual cavity collapses in the cloud (Wang and Brennen, 1999). It is shown (Arakeri and Shanmuganathan, 1985) that it is possible to predict the noise spectrum generated by a cavity cloud based on single cavity bubble dynamics if the bubble volume fraction or void fraction, α , is small (<0.1). For example, when the void fraction is small, the noise spectrum increases over the whole frequency range by increasing the number of cavities. However, if the number of cavities within a cloud increases beyond a certain limit, the generated noise will decrease (see Figure 6 in (Arakeri and Shanmuganathan, 1985)). This might be caused by the physical overlap of bubbles and distortion in the cavity bubble shapes near their maximum radii. It is shown that interaction of bubbles within the cloud can be neglected if the cloud interaction parameter ($\beta = \alpha_0 (1 - \alpha_0) A_0^2 / R_0^2$) is less than one (Wang and Brennen, 1999; Brennen et al, 1999). In this relation, α_0 is the initial void fraction, A_0 is the initial cloud radius (assuming spherical cloud) and R_0 is the initial bubble radius. For large values of the cloud interaction parameter, the bubble collapse pattern produces an inward acoustic wave and the corresponding shock wave is strengthened as a result of geometric focusing effects (Wang and Brennen, 1999). In the current experiment, the ghost cavitation cloud is visualized from high-speed video recordings of a seismic air-gun array consisting of two subarrays. The video images show the generation of multiple cavities and these images strengthen the ghost cavitation hypothesis. Even though the time resolution is not excellent (8.3 ms between two frames), it is possible to observe the creation and disappearance of the ghost cavity cloud. The shape of the cloud at different stages is also possible to study by looking at several shots since they have slightly different time zero compared to each other. The air-gun firing system is not synchronized with the video recording. The ghost cavity cloud and the corresponding acoustic signal is simulated using the numerical modeling procedure proposed by Khodabandeloo et al. (2017). The cavity clouds observed

by video recordings are compared to modeled cavity clouds. Finally, we compare the measured acoustic signal to the modeled signal.

4.3 The field experiment

The field experiment was conducted in 2011 offshore Congo in water depths between 1500 and 3000 m. The weather condition was good and the sea state was calm during the experiment. The source vessel was moving at a speed less than 2 knots (≈ 3.7 km/h). Field data that are used in this paper are from the source array configuration shown in Figure 4.1. It consists of two sub-arrays where each one includes ten individual air guns. A high-speed underwater camera, with recording speed of 120 frames per second, was mounted on one of the sub-arrays with a view angle as shown in Figure 4.1. A broad-band hydrophone (bandwidth=520 kHz) was suspended 17 m below the source array. There is an uncertainty related to the precise positioning of the hydrophone relative to the source array and most likely it deviates a few meters backward (off the vertical) due to towing effects. Top view of the approximate position of the hydrophone relative to the air-guns is shown in Figure 4.1 (blue triangle).

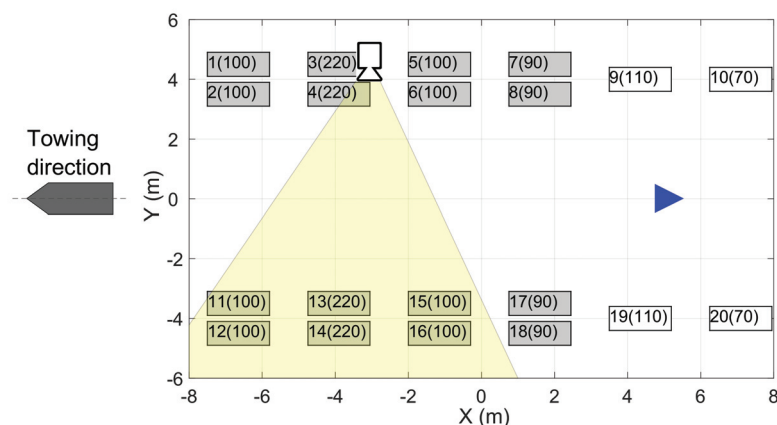


Figure 4.1: Air-gun array configuration used for the field experiment. There are twenty air-guns arranged in two sub-arrays and the air chamber volumes (in cubic inches) are shown next to the gun number within the parentheses. Single air-guns are shown by white rectangles and clustered air-guns by gray. The video camera is mounted on one of the sub-arrays (near guns 3 and 4) and its approximate view angle is shown as a yellow cone. The approximate location of the hydrophone is shown by the blue triangle.

The acoustic signals were recorded using a sampling interval of 0.0032 ms, and no gain was applied. The hydrophone sensitivity is 204 dB re 1 V μ Pa. Measured

signals beyond $\pm 0.5V$ were saturated (clipped). More details of the experimental setup can be found in Landrø et al. (2016).

4.3.1 High-frequency signal measurement

For a source depth of approximately 9 m and a sub-array separation distance of approximately 8 m, a typical measured signal is shown in Figure 4.2 (left). It is observed that some parts of the signal are saturated. For example, saturation occurs between 30-31 ms, 34-35 ms, 36-37.5 ms, and 47.5-48.5 ms. Fortunately, the ghost cavitation signal which is the focus of the experiment is not affected heavily by clipping. The reason is that the ghost cavitation signal arrives with some delay (6-20 ms) after the primary peak (Landrø et al., 2011; Landrø et al., 2013; Khodabandeloo et al., 2017). For the signal shown in Figure 4.2, the ghost cavitation signal is slightly affected by saturation effects for the time interval around 47.5-48.5 ms.

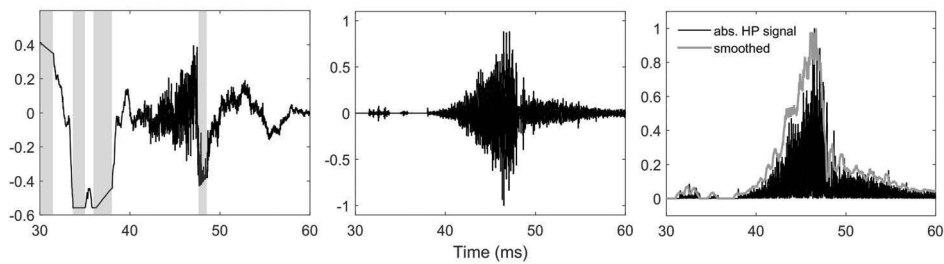


Figure 4.2: Unfiltered measured signal for with a broadband hydrophone suspended around 17 m below the array (left). The saturated parts are indicated by gray vertical ribbons. 10 kHz high-pass filtered (middle). Absolute values of high-pass filtered data and its smoothed envelope (right). The source depth is 9 m and the sub-array crossline separation distance is 8 m.

After applying a 10 kHz high-pass filter to the signals shown to left in Figure 4.2, the result is shown in the middle picture of the same figure and the absolute values of the high-pass filtered signal and the smoothed envelope using a moving average filter are shown to the right. For four different shots, smoothed amplitudes of the 10 kHz high-pass filtered signals are plotted in Figure 4.3. The curves indicate that the pattern and envelope of high-passed filtered ghost cavitation signals are highly repeatable. All the high-pass filtered signals share the same pattern: the energy is accumulated with a smaller rate in the beginning than at the end which causes a fast cessation of the signal at the end.

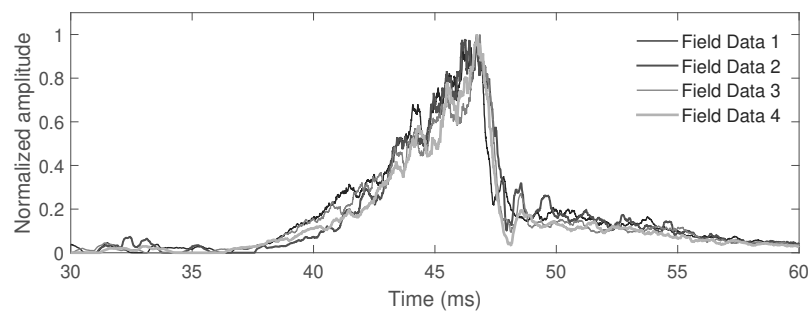
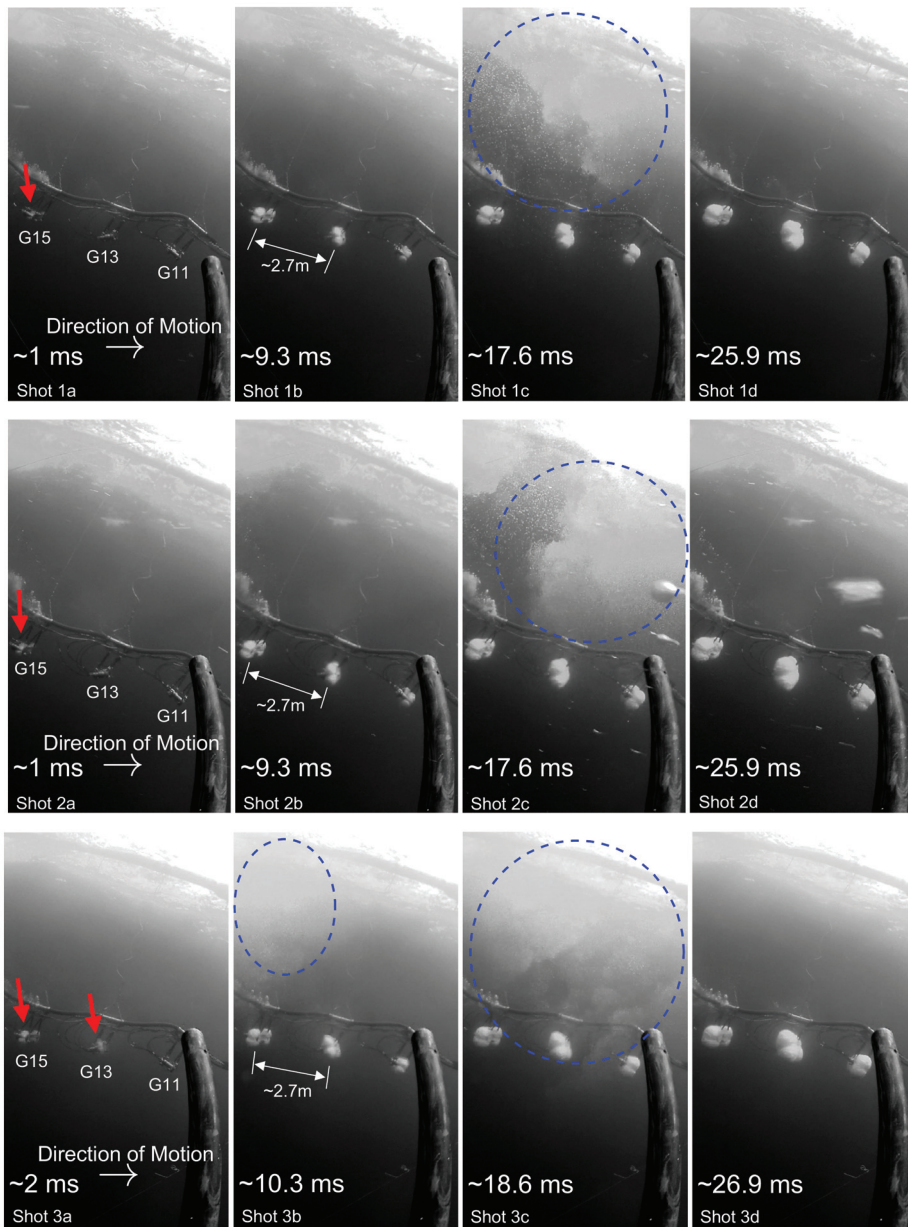


Figure 4.3: Smoothed absolute values of four 10 kHz high-pass filtered measured signals (shots).

4.3.2 Field video recording

Air-guns 11 to 16 (Figure 4.1) are present in the camera frame and four successive recorded frames are shown for four different shots in Figure 4.4. Each row represents frames from one shot. The first image of each row is the first frame for each shot and shows the initial phase as the air escapes through the gun ports. Since the air-gun firing system is not synchronized with the video recording, the images in the first column do not correspond to the same stage after the guns are triggered. If time zero ($t=0$) for each shot is the time when the earliest air-gun is fired (opening of air-gun ports), an approximate time can be estimated for the first frame. In the first frame of the first and second shots (rows) in Figure 4.4 (denoted shot 1a and shot 2a, respectively) air is only observed escaping gun 15 (G15) as indicated by the red arrow. If time zero ($t=0$) for the first source firing is when ports of gun 15 become open, based on the amount of air that has exited from gun 15 in shot 1a, the time instant corresponding to this frame (shot 1a) is estimated to be 1 ms. Using the same method for the other shots, a time instant for the first column is estimated, as shown in Figure 4.4.



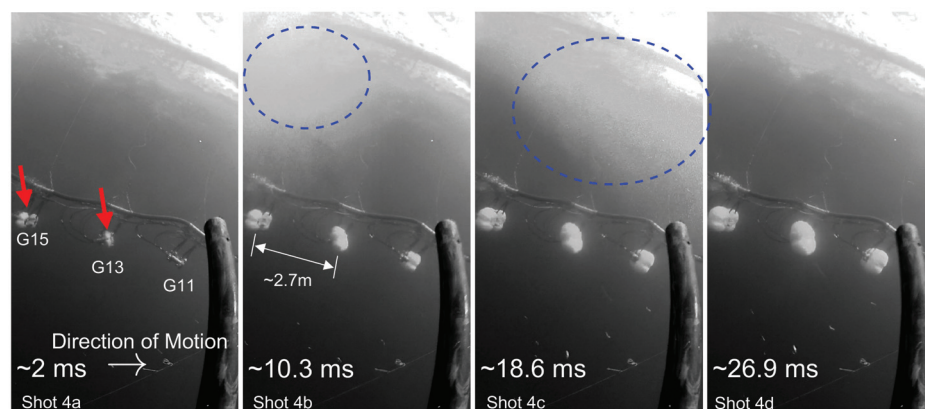


Figure 4.4: Video recording of part of one subarray using a high-speed camera (120 fps) mounted on the other sub-array. Each row represents frames from one firing of the source array; a, b, c, and d refer to successive images from the same shot. Guns 11, 13 and 15 are in the camera frame and indicated by G11, G13, and G15. Red arrows indicate air escaping the air-gun(s) in the first frame of each shot. In shot 1a and shot 2a air is seen exiting gun 15 while no air is seen escaping gun 13 and 11. In shot 3a and shot 4a the air is only observed escaping gun 15 and 13 as indicated by the red arrows. The cavity cloud is observed in shot 1c, shot 2c, shot 3b, shot 3c, shot 4b, shot 4c and indicated by blue dashed ellipses. If zero time is opening of air-gun ports, the associated time to the recorded frame time is assigned depending on amount of air exiting the gun(s) in the first frame: 1 ms for first and second rows (shot 1a and 2a) and 2 ms for third and fourth rows (shot 3a and 4a).

Figure 4.4 shows that the cavity cloud appears in frame three for the two first shots. For the last two shots, the cloud is visible in the 2nd and 3rd frame (shot 3b, c and 4b, c). The cloud disappears in the fourth frame (~ 25.9 or 26.9 ms) for all shots. Despite that the video time resolution is not sufficient to study the detailed evolution of the cavity cloud, it is possible to get an impression of the development by comparing image sequences from several shots as shown in Figure 4.4. The cavity cloud forms somewhere in the middle top of the array and then moves towards the right-hand side of the figures (above G15 and G13) which is in the towing direction.

4.4 Modeling the ghost cavity cloud

The simulation method is summarized in the Appendix and for more details of the simulation technique, we refer to Khodabandeloo et al. (2017). Using the source array shown in Figure 4.1, pressure variations at different locations around the air-gun array are estimated by adding the pressure from each air-gun to the hydrostatic

pressure of the corresponding location. The response of a stable free micro-bubble with an equilibrium radius of $20\ \mu\text{m}$ to the estimated pressure variations is estimated by equation 4.1 in the Appendix. In the simulation, due to the observed delays between air-gun firings in the first image of each row in Figure 4.4, all the air-guns are not fired simultaneously and some of them are fired with some minor delays. We have assumed the guns in each cluster (for example, guns 15 and 16 form one cluster) are fired simultaneously. Furthermore, we assume that the two sub-arrays have same performance which means for example gun 5 and 6 are activated simultaneously with gun 15 and 16. It is the same for guns 3, 4, 13 and 14. Guns 1, 2, 11 and 12 are fired simultaneously as well. The remaining guns which are not in the images, that is guns 17 to 20 and guns 7 to 10 are fired simultaneously with gun 15. For an air-gun, the peak pressure occurs approximately at the time when the air escapes through the ports. For simplicity, we choose the time when the first air is visible at the port opening as time zero. Selecting the time when the modeled pressure of earliest gun(s) reaches its peak value as zero time ($t = 0$) in the simulation, ensures having roughly the same time reference between the simulated and the photographed cavity cloud.

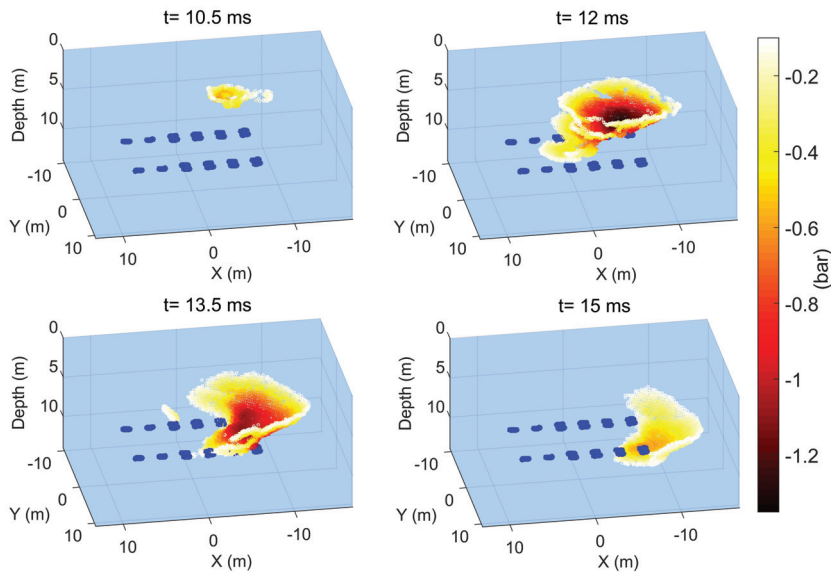


Figure 4.5: Simulated minimum pressure distributions for four time instants ($t=10.5, 12, 13.5, 15$ ms) for the case of firing some guns delayed with respect to the others in the array.

Based on the amount of air released from the guns in the first image in each row in Figure 4.4, we estimated a time delay of 2.5 ms for guns 1, 2, 11, and 12 and a time

delay of 1.5 ms for guns 3,4, 13, and 14. The temporal and spatial distributions of minimum pressures are obtained from air-gun modeling and are shown in Figure 4.5. The computational domain uses a three-dimensional grid with a spatial resolution of 0.2 m and it is assumed that a cavity is formed if the pressure drops below a certain level (-0.1 bar) at that grid location. The temporal sampling interval for the simulations is 0.1 ms.

Cavity lifetimes (growth + collapse times) at different locations are estimated using equation (1), given in the Appendix, are shown as a function of minimum external pressure and depth in Figure 4.6.

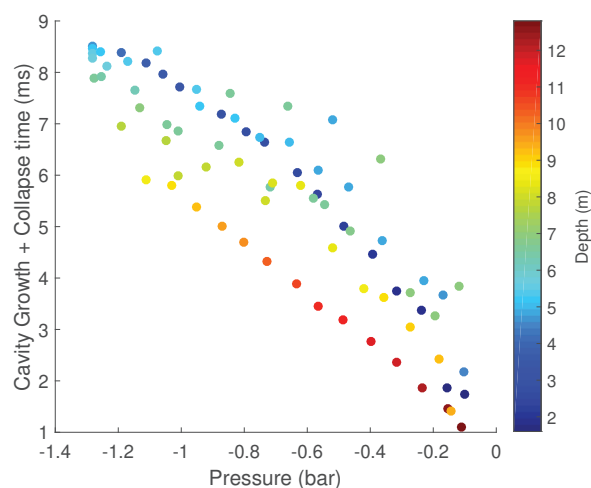


Figure 4.6: Cavity lifetimes (growth + collapse times) at different locations around the array as a function of the minimum pressure of external pressure that each cavity had been exposed to for the case of firing some air-guns with the delay in the array. Bubble dynamic equation 4.1 is solved for each cavity to estimate its lifetime.

The time when the pressure reaches its minimum and fulfills the requirement (< -0.1 bar) for cavity creation is considered as the initiation time for that specific cavity. Having the initiation time (Figure 4.5) and the lifetime of each cavity (Figure 4.6), we know the timing when each cavity appears in the cloud. Modeled cavity clouds for six time instants are shown in Figure 4.7.

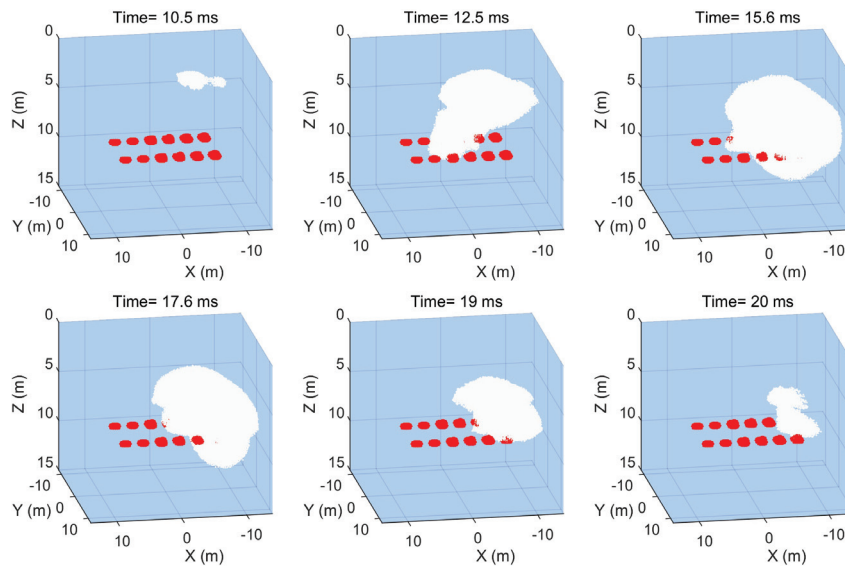


Figure 4.7: Simulated cavity cloud for the case where some air-guns are fired with some delay in the array.

The modeling predicts that a cavity cloud is formed above the source array. Then it moves slightly downwards and to the right (Figure 4.7). The cloud shape and pattern resemble the photographed cavity cloud. Simulation results indicate that the cavity cloud is present for around 10 ms, which means if it is video recorded every 8.3 ms, it will appear at most in two frames which is in agreement with the video recordings shown in Figure 4.4. If all air-guns are fired simultaneously, the modeled cavity cloud will be somewhat different, as shown in Figure 4.8.

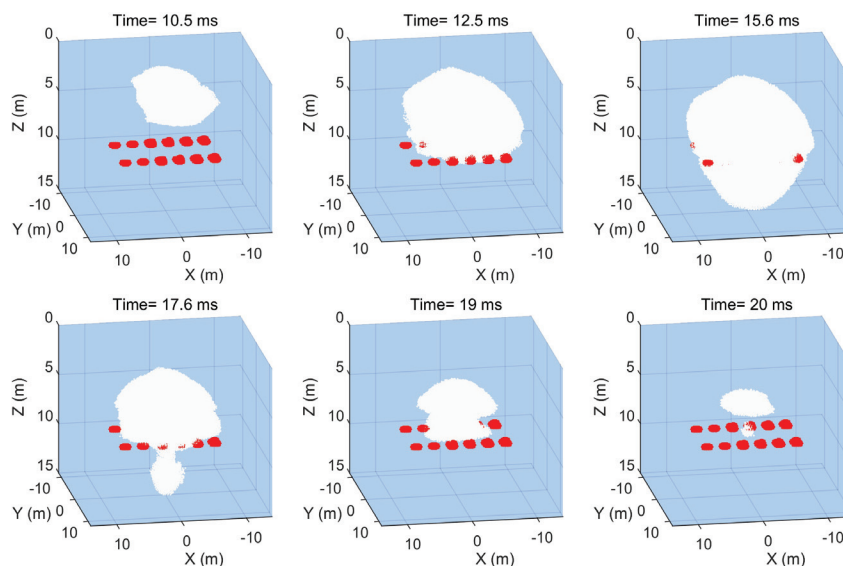


Figure 4.8: Simulated cavity cloud for the case where all air-guns in the array are fired simultaneously.

The cloud is initiated somewhere in the middle top of the array and then moves to both sides and extends downwards. Figure 4.6 and Figure 4.5 will also be different for the case when all guns are fired at the same time.

4.5 Comparison of numerical modeling and field measurements

The simulated cavity cloud assuming relative delays in air-gun firing times (Figure 4.7) better resembles the photographed cavity cloud than assuming that all guns are fired simultaneously (Figure 4.8). To have a closer look at the modeled and photographed cavity cloud, the image from the video recording and the corresponding simulated cavity cloud are shown in Figure 4.9 for a time instant of 17.6 ms. To compare with the photographed cavity cloud, a cut section of the modeled cloud (Figure 4.9; right) is shown to include only one sub-array in the image.

Air-guns 11 to 16 are present in the frame of the camera. The camera frame is approximately shown by the green transparent plane in the modeled cloud shown in Figure 4.9 (right). In our modeling, at each grid point a cavity grows – and subsequently collapses – provided that a minimum pressure threshold is fulfilled at that grid point. Hence, the grid resolution determines the initial number of cavities in the modeling. The actual number of cavities can be determined by cal-

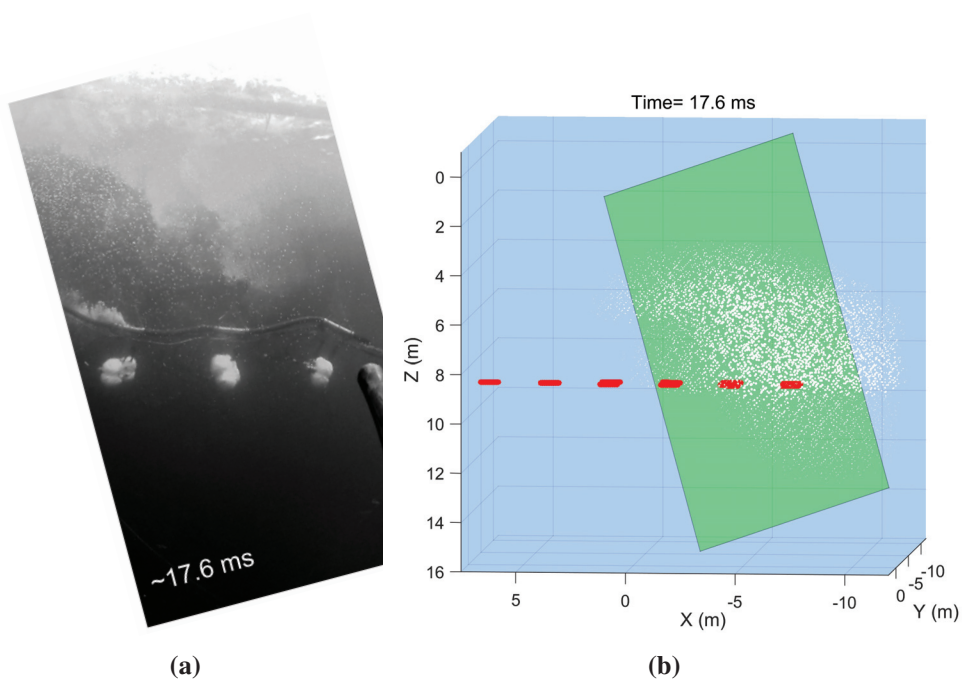


Figure 4.9: Comparison of the cavity cloud observed from video recording and the corresponding numerical modeling. In the modeled cloud, the corresponding frame of the camera is approximately shown by the green plane.

ibrating the model such that the amplitude, energy, or frequency content of the modeled ghost cavitation signals matches the measurements. However, the calibration highly relies on the calculated acoustic pressure signatures from collapses of individual vapor cavities since there is a tradeoff between the strength of each cavitation signal and the number of cavities. The calculated acoustic pressure signature from collapse of individual vapor cavity seems to have a very high peak compared to the experimental results of single cavity collapses (Versluis et al., 2000). One cause might be that the diffusion of dissolved gases (Plesset, 1970; Prosperetti, 2017) is ignored in the bubble dynamic equation. Diffusion adds some permanent gas to the cavity and cushions the collapse (Neppiras, 1984). The other reason might be the interaction between the growing cavity and the pressure fields from other cavity collapses. For a different air-gun array but the same grid resolution as we used here, Khodabandloo and Landrø (2017a) calibrated the model (on a trial and error basis) such that both the amplitude of high-frequency modeled signal and its associated low-frequency part matches the measurements. In that paper we artificially reduced the peak pressure of individual cavity collapse signatures and determined a single scaling factor equal to 0.07 ($\approx 1/14$) that gave a good match for both the amplitude of the modeled high frequency signal and its associated low-frequency part. This means that the assumed number of cavities should be reduced by factor of 14. Therefore, the number of cavities shown in the modeled cloud in Figure 4.9 is reduced compared to the corresponding time (17.6 ms) in Figure 4.7 by a factor of 14. As seen in the front view of the modeled cavity cloud in Figure 4.10, the majority of the cloud is formed midway between the two arrays.

It should be noted that we do not claim that our model is calibrated in a systematic manner, nor is it the scope of this paper. For the current modeling results, we have applied a calibration factor which was obtained for the same modeling scheme using the same grid resolution but based on another field experiment with a different air-gun array configuration (three subarrays instead of two). Applying that calibration factor to the current model, the agreement between the modeled and the photographed cloud was improved. To calibrate the model in a more systematic way, dedicated experiments are required to estimate cavity sizes, the pressure signatures from single cavity collapse, and non-clipped broad-band recorded signals at different locations are needed for more than one or two array configurations.

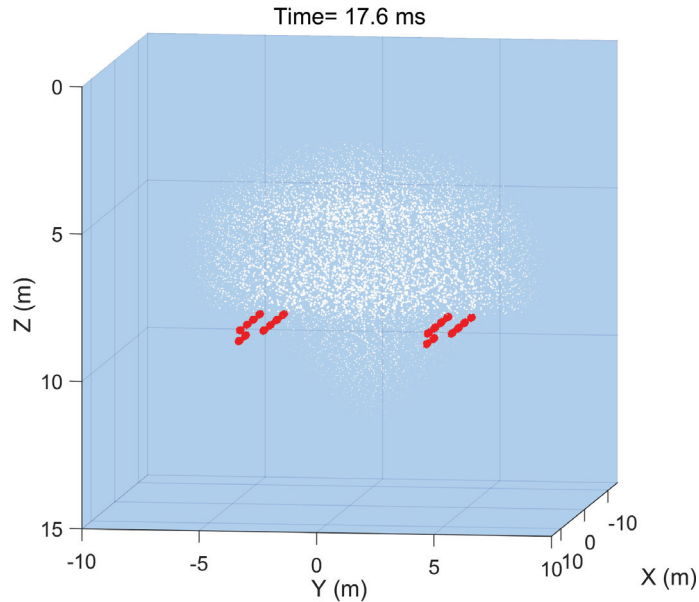


Figure 4.10: Front view of the modeled cavity cloud at 17.6 ms. The number of plotted cavities is reduced by a factor of 14 compared to the number of cavities based on selected grid resolution.

The 10 kHz high-pass filtered measured signal is shown in Figure 4.11 (top). Modeled ghost cavitation acoustic signals are shown in the second and third rows of Figure 4.11. Simulation 1 is the 10 kHz high-pass filtered modeled ghost cavitation signal without including reflection of acoustic pressure of cavities from the sea surface. In simulation 2, reflection of ghost cavities from the sea surface assuming a reflection coefficient of -0.4 is included. For rough sea surface and high frequencies it is reasonable to assume that the reflection coefficient is reduced significantly (Clay and Medwin, 1977, Landrø et al., 2013). Both synthetic and field data show a gradual amplitude increase followed by a rapid decrease. When including the ghost reflections of the ghost cavity signals from the sea surface, the simulated signal predicts the observed long tail after the rapid decrease in the field data (4.11).

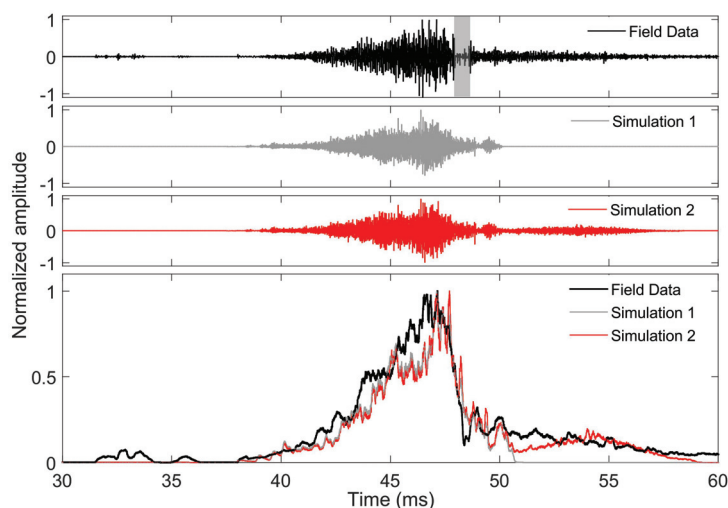


Figure 4.11: 10 kHz high-passed filtered ghost cavitation signal from field measurement (top), simulation 1 (2nd image from top) where the reflection of cavity signatures from sea surface is ignored. In simulation 2 (3rd from top) reflection of cavity signatures from the sea surface with reflection coefficient = -0.4 is included. In the top panel, the gray vertical ribbon indicates part of the signal that is clipped and cannot be compared directly with the modeled signal. Envelopes of absolute values are smoothed using a moving average method (bottom). All curves are normalized to one.

The envelope of absolute values of the field data, simulation 1, and simulation 2 are smoothed using a moving average window and plotted in Figure 4.11 (bottom). It is seen that there is a good agreement between modeled and measured curves regarding their time duration and shape of envelopes.

4.6 Discussion

In the modeled cavity cloud, we have assumed one stable micro-bubble with radius $20 \mu\text{m}$ at each grid point in the computation domain with cell sizes of $0.2\text{m} \times 0.2\text{m} \times 0.2\text{m}$. The void fraction, α_0 , in our example is $0.07 \times (4/3) \pi R_0^3 / 0.2^3 = 2.9 \times 10^{-13}$ where 0.07 is the scaling factor that we discussed in section IV. By void fraction we refer to those stable microbubbles within the sea water acting as cavity nucleation site. Assuming the equivalent spherical cloud radius equal to 5m, then the cloud interaction parameter is estimated by $\beta = \alpha_0 (1 - \alpha_0) A_0^2 / R_0^2 = 0.018$. Considering the values of the void fraction and cloud interaction parameter, the bubble-bubble interaction within the cloud can be neglected (Wang and Brennen, 1999; Brennen et al, 1999; Arakeri and Shanmuganathan, 1985). For an air-gun array the asynchronicity between air-guns is normally less than 1 ms. Weighting

the assigned time delay of each air-gun by its air-chamber volume, the average delay is 0.97 ms in this experiment. Even though the allocated time delays for the air-guns in our modeling seem a bit larger than the expected time delays in an air-gun array, they improve the similarity between the modeled and imaged cavity cloud. Moreover, we do not have access to the detailed firing time delays in the current experiment where the video recordings indicate that actual firing time delays might be slightly higher compared to normal operations.

It should be noted that the shapes of the cloud pattern observed from the video recordings vary from shot to shot which is probably caused by slightly different firing time delays for each shot. However, the recorded high-frequency acoustic signal is highly repeatable. Even though cavity collapse interaction and possible non-linear phenomena, as well as effects of cavitation cloud on acoustic propagation such as reduction in sound speed and increase in attenuation, are ignored, there is a good agreement between the modeled and field data in terms of the time duration and signal envelope shape. However, the model needs further calibration such that – in addition to the time duration, amplitude and shapes – the energy and frequency contents of modeled ghost cavitation signals match the measured. To do so, it would be necessary to record the non-saturated (non-clipped) acoustic signature at several locations for more than one source array.

4.7 Conclusion

The ghost cavity cloud generated by an air-gun array is observed using a high-speed video camera. The photos of the ghost cavity cloud support the hypothesis of source ghost cavitation. From the images it is clearly observed that multiples of cavities appear for a short time interval (10 ms) after the guns are fired. Synthetic modeling predicts an onset time as well as the time duration of the cavitation signal that fits the field observations. Furthermore, the modeled shape and position of the cavity cloud resembles those of the video recordings. There is a good agreement between the field recorded high-frequency acoustic signals and those from the modeling. For future field experiments to better capture the ghost cavitation phenomenon, it is suggested to perform the video recording with higher speed (>480 fps) and use two cameras; one in front of the array and one at the side.

4.8 Appendix: Ghost cavitation modeling

An air-gun array consists of several individual air-guns with different air chamber volumes. The array used for this study consists of 20 air-guns arranged in two sub-arrays as shown in Figure 4.1. Hydrostatic pressure can drop below a certain threshold at some locations around the array as a result of the reflected acoustic pressure of individual air-gun from the sea-surface. The pressure at two different

locations around the array are shown by dashed curves in Figure 4.12. It is seen that the hydrostatic pressure becomes negative based on linear theory from the superposition of pressures from individual air-guns in the array. From the initial part of the pressure curves, it is seen that the one shown in the right graph belongs to a deeper location since it has larger hydrostatic pressure. It is possible to estimate the response of a tiny stable bubble subjected to the external pressure, P , in the following bubble dynamics equation (Prosperetti and Lezzi, 1986):

$$\begin{aligned} & \left(1 - \frac{1}{c} \frac{dR}{dt}\right) R \frac{d^2 R}{dt^2} + \frac{4\mu}{\rho c} \frac{d^2 R}{dt^2} = \\ & - \frac{3}{2} \left(1 - \frac{1}{3c} \frac{dR}{dt}\right) \left(\frac{dR}{dt}\right)^2 - \frac{1}{\rho R} \left[2\sigma + 4\mu \frac{dR}{dt}\right] \\ & + \frac{1}{\rho} \left(1 + \frac{1}{c} \frac{dR}{dt}\right) [P_i(t) - P] + \frac{R}{\rho c} \frac{P_i(t)}{dt}. \end{aligned} \quad (4.1)$$

In the above equation, $R(t)$ denotes the time-dependent cavity radius, c is the sound speed of undisturbed water, $\sigma = 0.074 \text{ N/m}$ is the water surface tension (Nayar et al., 2014), ρ is the density of water, and μ is the dynamic viscosity of water. The pressure inside the cavity is shown by $P_i(t)$ and is modeled by Van der Waals equation. Substituting two pressure time curves given in Figure 4.12 as external pressure in (1) the response of a bubble with initial size of $20 \mu\text{m}$ are estimated by solving the differential equation by means of the Runge-Kutta method of order 5 (“ode45” algorithm in MATLAB) and plotted as solid curves in the same figure. There are microbubbles with the size between $18 \mu\text{m}$ to $350 \mu\text{m}$ uniformly distributed up to 36 m depth in the sea at wind speed of around 6 knots (Medwin, 1977).

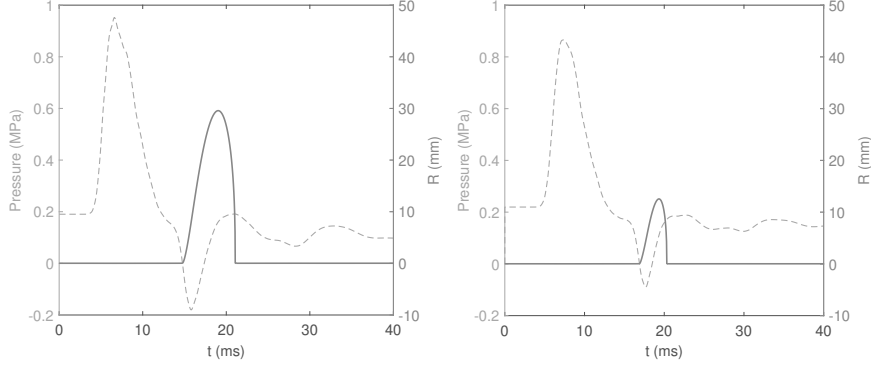


Figure 4.12: Response of a stable micro-bubble (solid curve) to pressure variations (dashed curve) at two different locations estimated from bubble dynamic equation given in (1). Left picture corresponds to a location with smaller depth compared to the right picture as seen from its smaller initial hydrostatic pressure.

Collapses of individual cavities generate acoustic pressure and its signature in the far-field is estimated by (Brennen, 2013; Leighton, 2012):

$$\begin{aligned}
 p(t) &= \frac{\rho}{4\pi r} \frac{d^2V}{dt^2} \\
 &= \frac{\rho R(t)}{r} \left(2\dot{R}^2(t) + R(t)\ddot{R}(t) \right)
 \end{aligned} \tag{4.2}$$

In the above equation, the superposed dot indicates a time derivative. Acoustic pressure signature of individual cavities obtained by (2) is propagated from where it is generated to the receiver location:

$$u_i(t, r) = \frac{1}{\sqrt{2\pi}} \int_{-\infty}^{+\infty} \left(S_i(f) \cdot e^{-\gamma(f)r_i} \cdot e^{-j2\pi f\tau_i} \cdot \frac{e^{-j\frac{2\pi f}{c}r_i}}{r_i} \right) e^{j2\pi f t} df \tag{4.3}$$

For the i th cavity, the distance between cavity source and its measured location is denoted by r_i , and τ_i shows its formation time. In the propagation, geometrical spreading and absorptions are included. $S_i(f)$ is the frequency domain representation of the time signal from the collapse of the i th cavity. γ stands for absorption (Neper/m) and is calculated from the equation given by Francois and Garrison (1982). Adding the pressure signature of individual cavities given in (3), it is possible to simulate the cavitation signal from the cloud of cavities. Detailed modeling steps of the ghost cavity cloud is given in (Khodabandeloo et al., 2017).

4.9 Acknowledgment

This research is funded by Research Center for Arctic Petroleum Exploration (AR-CEX) partners, and the Research Council of Norway (grant number 228107). The reviewers are acknowledged for their constructive comments and invaluable suggestions.

Chapter 5

Characterizing acoustic properties of cavity cloud as a time-dependent effective medium surrounding an air-gun array ¹

Babak Khodabandeloo

*Department of Geoscience and Petroleum,
Norwegian University of Science and Technology (NTNU)
NO-7491 Trondheim, Norway*

Martin Landrø

*Department of Electronic Systems
Norwegian University of Science and Technology (NTNU)
NO-7491 Trondheim, Norway*

5.1 Summary

A ghost cavity cloud consists of many small vapor cavities and appears above and around the air-guns in the source array few milliseconds after the source is fired. Since there are dissolved gases and stable microbubbles in natural seawater, the cavities will likely contain some amount of air in addition to water vapor. They

¹The paper is under review in *Geophysical Journal International*

cavity cloud exists for around 10 ms depending on the size and the configuration of the array. It is well known that increasing the volume fraction of tiny bubbles within the liquid, the sound velocity of the mixture at frequencies below the resonance frequencies of the bubbles gradually drops. Depending on the volume fraction of tiny bubbles, the sound velocity in the mixture can even drop below the sound velocity of individual constituents. Vapor content within the bubbles – or cavities – further reduces the sound velocity. We do not know whether the volume fraction of cavities is high enough to significantly drop the sound velocity, nor do we know whether the far-field acoustic recording is affected even if the sound velocity within the cavity cloud drops substantially. To answer these questions, a modified k-wave – a k-space pseudo-spectral numerical method – is used. Subsequently, the simulation results are compared to recorded field data in order to estimate a potential sound velocity drop within the ghost cavity cloud.

5.2 Introduction

Cavities can be formed underwater when the pressure drops below the vapor pressure or partial pressure of the dissolved gases (Mellen, 1954; Plesset, 1970). Acoustic waves emitted from air-guns in a seismic air-gun array are reflected from the sea surface with opposite polarity. Hence the addition of reflected pressure waves can drop the hydrostatic pressure of water at some locations temporarily which is sufficient for cavity growth and subsequent collapse. This phenomenon was first hypothesized by recording high frequency (> 10 kHz) signals in a seismic air-gun array field measurement (Landrø et al., 2011). It was further analyzed (Landrø et al., 2013) and investigated based on a dedicated field experiment (Landrø et al., 2016). The ghost cavitation phenomenon in an air-gun array is numerically modeled and could successfully predict the recorded high-frequency ghost cavitation signals (Khodabandeloo et al., 2017) and the associated low-frequency component (Khodabandeloo and Landrø, 2017a). Unless the water is fully degassed, the cavities contain some amount of air in addition to the vapor phase (Neppiras, 1984; Prosperetti, 2017). It is well known that even small volume fractions of bubbles in a liquid affect sound speed and attenuation of acoustic wave propagation significantly (Commander and Prosperetti, 1989). For example, adding tiny bubbles with the fraction volume of 0.1% reduces the sound velocity of the mixture with 80%. The primary cause for this effect is that presence of air greatly decreases the compressibility of the bubbly medium while its density is almost unaltered (Kieffer, 1977). Other than the volume fraction of the gas, bubble size distribution and the frequency of the acoustic wave also affects the sound speed in the bubbly liquid. At low frequencies (compared to the resonances of bubbles) the sound velocity is mainly a function of the volume fraction of gas (Wilson and Roy, 2008). Sound velocity in a water-vapor mixture is even smaller than a water-air

mixture for the same volume fraction of vapor and air (Barclay et al., 1969; Fuster and Montel, 2015; Prosperetti, 2015, 2017). Vapor bubbles are much more labile objects compared to gas bubbles since the thermal diffusivity is much larger than mass diffusivity in most liquids including water. Hence, there are fewer and less conclusive experiments on vapor bubbles compared to gas bubbles (Prosperetti, 2017). Propagation of acoustic waves through a bubbly liquid has been studied by several researchers in the last centennial and especially during World War II to utilize underwater acoustics in submarine warfare (Domenico, 1982). The acoustic impedance mismatch between the layer of bubbly water and bubble-free water is exploited in several practical applications. Bubble curtains were deployed to prevent damage to the submerged infrastructures from shock waves due to underwater blasting or explosion (La Prairie, 1955). To mitigate the noise from pile driving activity, a bubble curtain from free rising bubbles was devised to surround the source (Wursig et al., 2000) and to shield a porpoise pool (Lucke et al., 2011). Bubble curtains with irregular shapes were placed at the bounce point of acoustic waves from sea-surface to suppress the multiples (Ross et al., 2005).

The ghost cavity cloud has the potential to locally and temporarily change the medium properties in terms of sound velocity and attenuation. There are two questions in this regard:

1. Whether the cavity cloud changes the sound velocity of water and how much it does.
2. If the cavity cloud changes the sound velocity of water, is the far-field acoustic recording affected by such a short duration and local change in the sound velocity?

An affirmative answer to the second question opens the path to answer the first question by comparing the modeled and recorded far-field signatures. Subsequently, it might be possible to further characterize the ghost cavity cloud with regard to the sound velocity variations, average size and number of cavities.

If the resonances of bubbles within the cloud are much higher than the frequency of the propagating acoustic wave, the cloud can be considered as a uniform medium with effective acoustic properties such as sound speed and attenuation (Leighton, 1994, pp 258-278). The macroscopic properties of an effective medium are linked to the characteristics and relative fractions of its constituent components (Lee et al., 2011). To investigate the acoustic properties of the ghost cavity cloud, we use numerical methods. It is possible to discretize either the second-order acoustic wave equation or a set of coupled equations based on conservation of mass, momentum, and equation of state (Liu, 1998). Discretizing and solving a set of

coupled first order equations makes it easier to include mass and force sources and to include a perfectly matched layer (PML) around the computational domain. PML absorbs the acoustic waves that reach the boundaries of the computational domain and avoids that waves are reflected back. *k*-wave is an efficient MATLAB toolbox which solves three coupled first-order partial differential equations for acoustic wave propagation (Treeby and Cox, 2010; Treeby et al., 2012). It uses *k*-space and pseudo-spectral method for temporal and spatial discretization, respectively. *k*-space pseudo-spectral algorithm is more efficient than many of finite difference and finite element methods because it provides the same degree of accuracy with much coarser grid spacings and larger time steps (Tabei et al., 2002; Cox et al., 2007). In this paper, we numerically study the effects of sound velocity reduction within the ghost cavity cloud on the far-field acoustic measurements using the *k*-wave MATLAB toolbox. Since the ghost cavity cloud appears for only a few milliseconds, it requires a simulation of the acoustic wave propagation within a non-stationary (time-dependent) medium. The ghost cavity cloud is introduced into the numerical model to change locally and temporarily the acoustic sound speed of the medium (water). It is assumed that the resonance frequencies of the gas/vapor cavities within the cloud are higher than the propagating acoustic waves and that the acoustic attenuation of the cloud can be neglected. The simulation results are compared to recorded far-field data and the sound velocity within the ghost cavity cloud is estimated.

5.3 Visualizing ghost cavity cloud

A dedicated field experiment was conducted in 2011 offshore Congo to video-record the ghost cavity cloud. The source array used in the field test was towed at 9m depth and consists of two sub-arrays with 8m horizontal separation. More details are given by Landrø et al. (2016). Part of one of the sub-arrays is video-recorded by a high-speed camera mounted on the other sub-arrays. The recording speed was 120 fps and four successive frames from one source firing are shown in Figure 5.1.

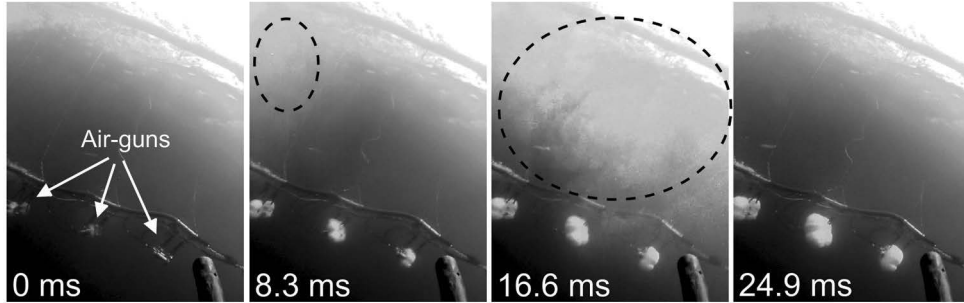


Figure 5.1: Four successive frames from video recordings of one the sub-arrays with recording speed of 120 fps. The first image (0 ms) is the first frame when the air is observed escaping air-guns. Cavity clouds are indicated by dashed ellipse. The distance between two adjacent air-guns is around 2.7 m.

The cavity cloud appears partly in the second and mainly in the third frame after the guns were fired as shown in Figure 5.1. A hydrophone was mounted 17m beneath the array to record the acoustic signals. However, since the recorded acoustic signals in this experiment were saturated in some parts, they are not appropriate to be compared with the modeled signals. Details of the photographed cavity cloud and the recorded acoustic signal is given in (Khodabandeloo and Landrø, 2018).

5.4 Theory: speed of sound in gas/vapor mixture

The sound speed in a fluid medium, c , is defined as $c = \sqrt{K/\rho}$, where K is the bulk modulus (or compressibility) and ρ is the density. Wood (1946) derived these quantities to determine the acoustic propagation sound velocity in two fluid media such as water containing tiny air bubbles. He assumed that the mixture medium is a homogenous medium with a mean density and a mean elasticity and expressed the Wood 's equation to estimate the sound velocity of the mixture as (Wood, 1946. Page 360-363):

$$c_m = \sqrt{\frac{K_m}{\rho_m}} = \sqrt{\frac{K_l K_g}{(\beta K_l + (1 - \beta) K_g) (\beta \rho_g + (1 - \beta) \rho_l)}} \quad (5.1)$$

The volume fraction of the gas phase (or void fraction) is given by $\beta = V_g / (V_l + V_g)$, where V_g and V_l represent the gas and liquid volumes in the mixture, respectively. The above equation is valid for a mixture of any two fluids which do not react chemically. Furthermore, the air-bubbles should be non-resonant. In other words, it is valid for frequencies well below the resonance frequency of the air-bubbles (Silberman, 1957). Wave propagation through a bubbly medium was considered

as a problem of multiple scattering of waves by randomly distributed scatterers (Foldy, 1945). Effective medium is used instead of the complex system of a host medium containing scatterers. Including bubble dynamics and effects of bubble oscillations in the wave propagation through a bubbly medium, the following dispersion relation is derived for the averaged complex wave number of propagating wave in the mixture (Van Wijngaarden, 1972; Commander and Prosperetti 1989):

$$\frac{k_m^2}{\omega^2} = \frac{1}{c_l^2} + 4\pi \int_0^\infty \frac{R_0 f(R_0) dR_0}{\omega_N^2 - \omega^2 + i2\omega} \quad (5.2)$$

In the above equation, k_m is the effective wave number in the mixture, c_l is the sound velocity in the liquid without scatterers, ω_N is the natural frequency of the bubbles, ω is the angular frequency of the propagating wave, σ is the bubble dynamic damping constant, and R_0 is the equilibrium bubble radius. The probabilistic function for the size distribution at bubble equilibrium is given by $f(R_0)$, and $f(R_0)dR_0$ gives the number of bubbles per unit volume with the equilibrium radius between R_0 and $R_0 + dR_0$. In deriving the above equation it is assumed that the gas volume fraction (or void fraction) is small ($\beta \ll 1$). The void fraction can be estimated as (Commander and Prosperetti, 1989):

$$\beta = \frac{4}{3}\pi \int_0^\infty R_0^3 f(R_0) dR_0 \quad (5.3)$$

The wavenumber in equation 5.2 is complex valued and the phase speed of the mixture is obtained as $c_m = \omega/Re(k_m)$. If the frequency of the pressure perturbation is below the resonance frequency of the bubbles, equation 5.2 can be simplified to (Prosperetti, 2015, Equation (4.10)):

$$\frac{1}{c_m^2} = \frac{1}{c_l^2} + \frac{\beta\rho_l}{p_{g0}} \frac{1}{1 - 2\sigma/(3R_0 p_{g0})}, \quad (5.4)$$

where p_{g0} is the equilibrium pressure inside the bubble and σ is water surface tension. In many situations, bubbles in the liquid contain a mixture of gas and vapor. The formed cavities in a gas-free liquid should be vaporous (Neppiras, 1984). However, liquids in most practical situations contain some dissolved gas such as air. The dissolved gas in the liquid diffuses into the vapor cavity (or bubble) as it grows (Plesset, 1970; Prosperetti, 2017). Hence, usually there are some amounts of gas such as air inside the cavities. Furthermore, in many practical situations, microbubbles distributed in the liquid act as cavitation nuclei sites. In the sea water up to depth of 36 m there are uniformly distributed microbubbles with the

size between $18 \mu m$ to $350 \mu m$ when the wind speed is around 6 knots (Medwin, 1977). Vapor content changes the resonance frequency of bubbles and also reduces the speed of wave propagation in the frequency range below the resonance frequency of the bubbles (Fuster and Montel, 2015; Prosperetti, 2015, 2017; Zhang et al., 2017). When the bubbles contain vapor, at the low frequency limits the sound speed in the bubbly liquid is estimated (Fuster and Montel, 2015, Eq. (6.10)) to be:

$$c_m^2 = \frac{c_l^2}{1 + \frac{c_l^2 \beta \rho_l}{(1 + Y_0) p_{g0}}}. \quad (5.5)$$

In equation 5.5, Y_0 is the vapor fraction inside the bubbles with gas/vapor mixture contents. Based on the above formulas the speed of sound at low frequencies in a bubbly liquid with gas/vapor mixture as a function of void fraction is shown in Figure 5.2.

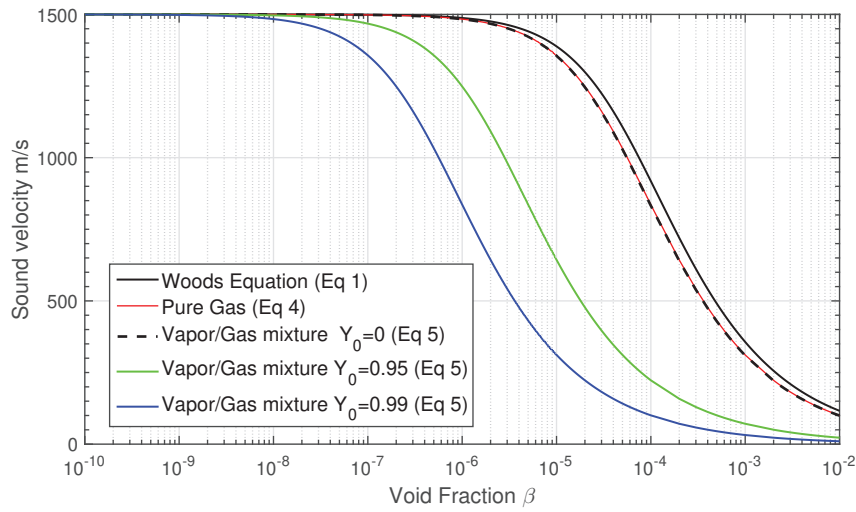
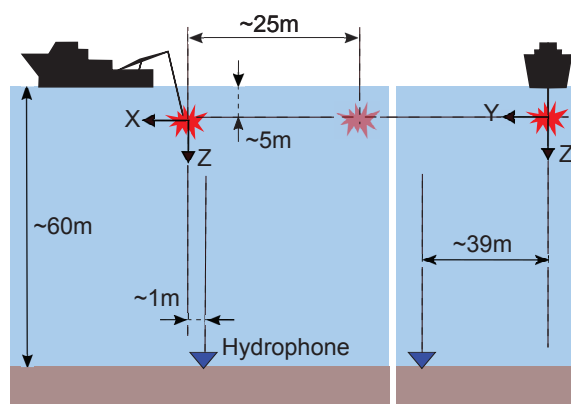


Figure 5.2: Sound velocity of water with gas and gas-vapor bubbles (or cavities) for the frequency range below the resonance frequency of bubbles. Wood's equation and equation 5.4 for gas bubbles have a good agreement. Furthermore equation 5.5 with zero vapor fraction coincides to the curve for water with pure gas bubbles.

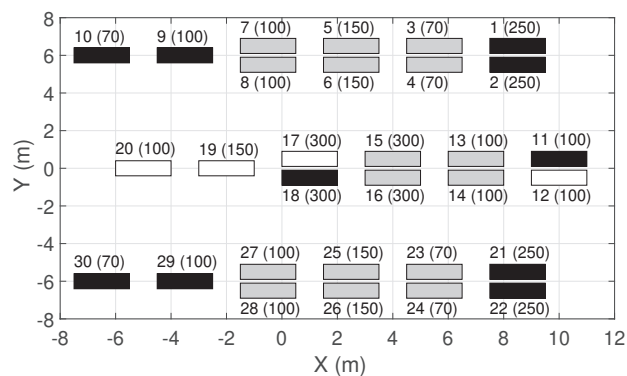
The above estimations are valid for wave propagation within a bubbly medium provided that resonance effects are negligible. That is the propagation frequency should be below all resonance frequencies for uniform bubble size distribution or below the resonance frequency of bubbles with predominant size distribution (Commander and Prosperetti, 1989).

5.5 Field experiment

The field experiment was performed in December 2008 in the Black Sea offshore Turkey in an area with a water depth of around 60 m. The signals were recorded using a stationary hydrophone located at the seabed. The source vessel towed the air-gun array at 5 m depth and sailed along a straight line with approximately 39 m crossline offset with respect to the recording hydrophone. The shot interval was 25 m. The side and front view of this field measurement are schematically shown in Figure 5.3(top). The sea state was calm during the experiment (Landrø et al. 2013). The air-gun array configuration used for the recorded data that we refer to as field data in this paper is shown in Figure 5.3 (bottom). Operating pressure of all the guns was 2000 psi and they were fired simultaneously, according to the plan.



(a)



(b)

Figure 5.3: (Top): Schematic side (xz) and front (yz) view of the field measurement; (Bottom): Air-gun array configuration used in the field experiment. Each air-gun air chamber volume (in^3) is given in the parentheses next to the air-gun number. The single guns are shown by white rectangle. The gray and black rectangles show cluster and inactive air-guns, respectively. In each array, the x -offset between air-guns is 3 m and the y -offset between clusters is 1 m. The x -offset between the air-gun 1 and 11 is 1.5 m.

Aligning x -axis of the Cartesian coordinate system along the sailing line, for the closest distance between shot and the hydrophone, the x -offset is estimated to be around 1 m.

5.6 Numerical implementation of wave propagation in the time-dependent medium – k-wave simulations

5.6.1 Governing equations and K-wave implementation

The simulations are performed using a 3-D computational domain k-wave Toolbox (Treeby and Cox, 2010; Treeby et al., 2012) which is an open source code based on k-space pseudo-spectral method. Instead of solving a single second-order partial differential wave equation, the simulation functions in k-wave solve the three coupled first-order partial differential equations based on conservation of mass, momentum and equation of state relating acoustic pressure to density fluctuations. For the linear and lossless wave propagation the equations are:

Conservation of mass:

$$\frac{\partial \rho'}{\partial t} + \nabla \cdot (\rho_0 \mathbf{v}) = S_M. \quad (5.6)$$

Density fluctuations are denoted by ρ' , the particle velocity vector by \mathbf{v} , the ambient (or equilibrium) density by ρ_0 and the mass source term by S_M which represents the time rate of input mass per unit volume (kg/m^3). Conservation of momentum (Euler equation) yields:

$$\frac{\partial \mathbf{v}}{\partial t} + \frac{1}{\rho_0} \nabla p' = S_F. \quad (5.7)$$

In the above equation S_F is the force source term with units of N/kg or m/s^2 and represents the body forces per unit mass. The equation of state is given as

$$p' = c^2 \rho' \quad (5.8)$$

Equation 5.8 is valid for time-independent sound velocity c . The ghost cavity cloud (see Landrø et al., 2016 and Khodabandeloo et al. 2017) is formed by several cavities that grow and collapse for a short period of time in the vicinity of the seismic air-gun array where the pressure drop is sufficiently large to trigger vapor cavity generation. The acoustic properties of regions where vapor cavities appear might change and therefore the governing wave equations should accommodate a time dependent medium. This means that the equation of state (equation 5.8) should be replaced by an appropriate equation to include a time varying sound speed. For isentropic flow ($Ds/Dt = 0$) the equation of state is (Pierce, 1981, chapter 1; Rienstra and Hirschberg, 2015, pp. 1519, 68–70):

$$p = p(\rho, s) \implies \frac{Dp}{Dt} = \left(\frac{\partial p}{\partial \rho} \right)_s \frac{D\rho}{Dt} \quad (5.9)$$

Where s represents entropy. The above equation can be rewritten as:

$$\frac{\partial p' + p_0}{\partial t} + v' \cdot \nabla(p' + p_0) = c^2 \left(\frac{\partial \rho' + \rho_0}{\partial t} + v' \cdot \nabla(\rho' + \rho_0) \right) \quad (5.10)$$

Ignoring the second order term and taking into account that the presence of cavities might change the sound speed while the change in the ambient density is negligible, equation 5.10 is simplified to the following equation:

$$\frac{\partial p'}{\partial t} = c^2 \frac{\partial \rho'}{\partial t} \quad (5.11)$$

The air-gun array (Figure 5.3) used for the field experiment is almost symmetric around the $y=0$ plane. It is possible to exploit this symmetry to reduce the size of the computational domain by introducing a slight position change for guns 12 and 17. Figure 5.4 shows the source used in the reduced computational domain with $y=0$ plane as a sound hard boundary condition (shown by dashed blue). For practical implementations, guns 12, 17, 19, and 20 are placed on the node in y -direction adjacent to the sound hard boundary plane, not on it. Since the sound hard boundary condition acts as a mirror, the strengths of these air-guns are scaled by 0.5 as indicated in Figure 5.4.

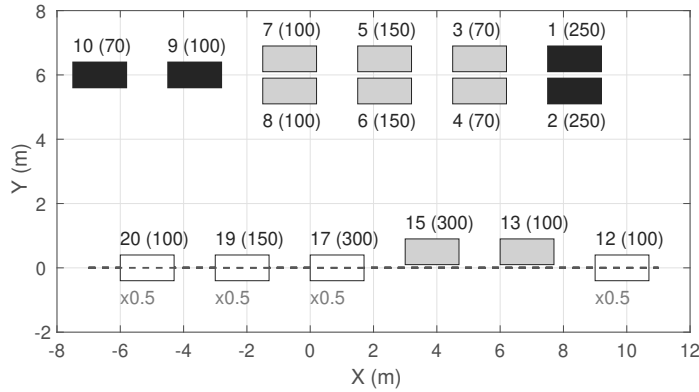


Figure 5.4: The source array configuration used in numerical modeling with half space computational domain exploiting the symmetry of the source array used in the field experiment. Symmetry plane is shown by dashed blue line. Since the symmetry plane is modeled as a sound hard boundary condition, the strength of the single air-guns located on this plane are scaled by 0.5 (See also Figure 5.3 (Right)). In practice the sources are not placed exactly on the sound hard plane; they are placed on the next node in the y -direction. Air-guns 12 and 17 are shifted slightly in the y -direction. The distances between air-guns are given in the caption of Figure 5.3.

The 3D computational domain is shown in Figure 5.5 with grid numbers $N_x = 192$, $N_y = 256$, and $N_z = 384$ in x , y , and z directions, respectively. The grid-point spacing ($\Delta x = \Delta y = \Delta z$) in all dimensions is $0.2m$. Since each air-gun is placed on a grid-point, considering the configuration of the air-gun array given in Figure 5.3 (right), some of the air-guns are shifted $\pm 0.1 m$ to accommodate the grid resolution in Figure 5.4. To observe how the modelled far-field acoustic pressures are influenced by such shifts in the air-gun positions, the simulated far-field acoustic pressure from the source shown in Figure 5.4 using k-wave and the one from full air-gun array (shown in Figure 5.3 (Right)) modeled by NUCLEUSTM are plotted in Figure 5.6 (a), i.e. line (i) and (iv), respectively. In both models, there is no sea-floor below the hydrophone. It is observed that the slight shifts in the air-gun positions have negligible effect on the far-field signature. Sound velocity of water is selected as $1500 m/s$ and the density is $1000 kg/m^3$.

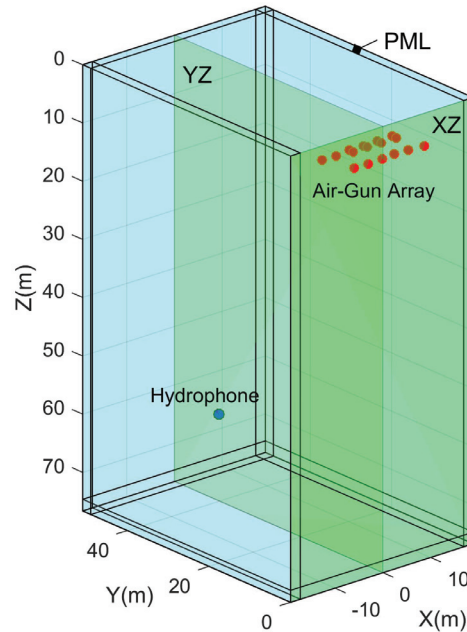


Figure 5.5: The computational domain for k-wave method. The source array and receiver (hydrophone) are shown. The ($Y=0$) plane is the pressure sound hard boundary condition and plane ($Z=0$) is the pressure release boundary condition. The boundaries are surrounded by a perfectly matched layer (PMLs).

The time step for iteratively solving the equations 5.2, 5.6, and 5.11 based on k-space pseudo-spectral method is obtained using Courant–Friedrichs–Lewy (CFL) number equal to 0.3, where $\Delta t = CFL \cdot \Delta x / c_{max}$ (Treeby et al., 2012). c_{max} is the maximum value of the sound speed in the medium. Based on the selected parameters the time step is $40\mu s$ and the maximum supported frequency is 3.75 kHz. The acoustic pressure emitted from each air gun in the array is modeled by the NUCLEUSTM source modeling package from Petroleum Geo-Services (PGS) and the output from this modeling is used as the mass source term in 5.6. The finest time resolution of the modelled source signatures by NUCLEUSTM is 0.5 ms. Therefore, the source signatures were interpolated using a piecewise cubic Hermite interpolating polynomial MATLAB function to have the time intervals of $40\mu s$, which is required by k-wave. To prevent the reflections from the edge

of the simulation region, the computational domain is surrounded by a Perfectly Matched Layer (PML) with 10 grid points thickness at each side as shown in Figure 5.5. Using first order coupled equations is convenient for PML implementation (Treeby and Cox, 2010). The $Z=0$ plane is the pressure release boundary condition simulating the sea-surface. To exploit the symmetry of the problem and solve it in the reduced computational domain, the $Y=0$ plane is the pressure sound hard boundary condition.

5.6.2 Effects of layered sea-floor on the recorded pressure

In Figure 5.6 (a), line (i) shows the simulated acoustic pressure at the hydrophone location using k-wave for the case when there is no sea-floor (i.e. in Figure 5.6(b), $\rho_1=\rho_2=\rho_3=1000 \text{ kg/m}^3$ and $c_1=c_2=c_3=1500 \text{ m/s}$). It is seen that the amplitude of simulated acoustic pressure is smaller than the amplitude of field recorded pressure while their shape has reasonable agreement. In Figure 5.6 (a), line (ii) shows the simulated far-field acoustic pressure for the case when a one-layer sea-floor is included beneath the hydrophone. It seems reasonable to select the density and sound velocity of the sea-floor sediments as 1600 kg/m^3 and 1600 m/s , respectively (Hamilton, 1978; Nobes et al., 1986). Therefore, in this case $\rho_1=1000 \text{ kg/m}^3$, $\rho_2=\rho_3=1600 \text{ kg/m}^3$ and $c_1=1500 \text{ m/s}$, $c_2=c_3=1600 \text{ m/s}$. Compared to the previous case, the amplitude of the simulated signal is increased and the match between the simulated and field recorded far-field pressure signatures is improved. Even though adding one-layer sea-floor beneath the hydrophone increases the amplitude of the simulated acoustic pressure at the hydrophone location, its shape is unaffected compared to the no sea-floor case as seen by plotting the normalized pressure signatures of these two cases in Figure 5.6 (c). However, the influence of sea-floor should appear 80 ms after the main peak. This 80 ms ($= 2 \times 60/1500 \text{ s}$) is the required time the reflected pressure from sea-floor reaches the sea-surface and is reflected back to the hydrophone. To see the effects of layered sea-floor on the recorded signal by the hydrophone on the sea-floor, it is assumed that 8 m below the sea-floor there is a change in acoustic properties of the medium. The density of the layer 8 m below the sea-floor is assumed to be 1700 kg/m^3 and its sound velocity is 1700 m/s . That is, for the two-layer sea-floor: $\rho_1=1000 \text{ kg/m}^3$, $\rho_2=1600 \text{ kg/m}^3$, $\rho_3=1700 \text{ kg/m}^3$, $c_1=1500 \text{ m/s}$, $c_2=1600 \text{ m/s}$, and $c_3=1700 \text{ m/s}$.

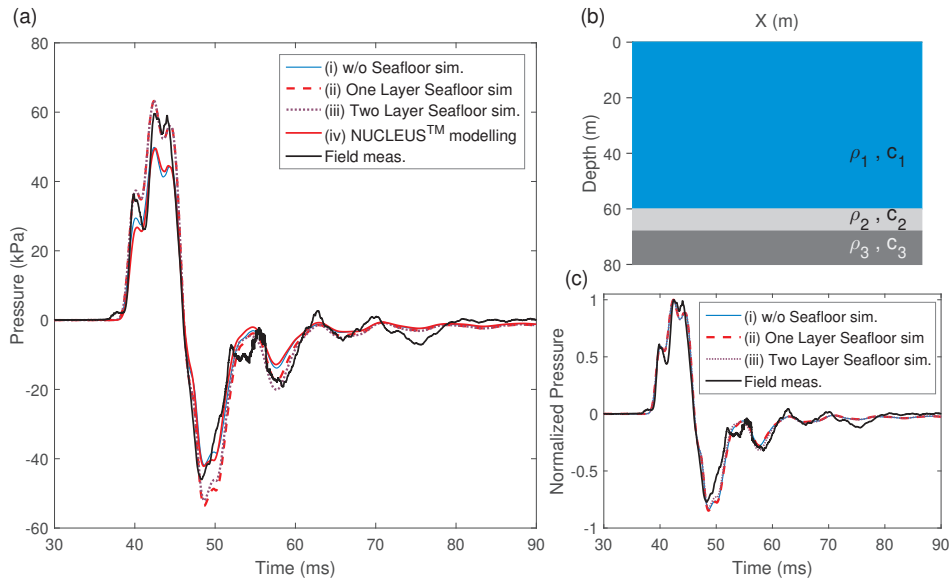


Figure 5.6: (a): Field recorded acoustic pressure signature is plotted together with the simulated far-field for different simulation scenarios (i) without sea-floor, (ii) one-layer sea-floor, and (iii) two-layer sea-floor. The scenarios depend on the selected values for density and sound velocities of layers shown in (b). i) no sea-floor: $\rho_1=\rho_2=\rho_3=1000 \text{ kg/m}^3$ and $c_1=c_2=c_3=1500 \text{ m/s}$, ii) one-layer sea-floor: $\rho_1=1000 \text{ kg/m}^3$, $\rho_2=\rho_3=1600 \text{ kg/m}^3$ and $c_1=1500 \text{ m/s}$, $c_2=c_3=1600 \text{ m/s}$, iii) two-layers sea-floor: $\rho_1=1000 \text{ kg/m}^3$, $\rho_2=1600 \text{ kg/m}^3$, $\rho_3=1700 \text{ kg/m}^3$, $c_1=1500 \text{ m/s}$, $c_2=1600 \text{ m/s}$, and $c_3=1700 \text{ m/s}$. Pressure signature simulated by NUCLEUS™ for the full air-gun array when there is no sea-floor is plotted (line (iv)). The normalized simulated far-field pressure signatures for different scenarios are plotted together with the normalized field recorded pressure signature in the Sub-figure (c). There is no reflection from the bottom of the third layer.

For the given two-layer sea-floor, the simulated acoustic pressure is plotted by line (iii) in Figure 5.6 (a) and its normalized version is plotted in Figure 5.6 (c). It is seen that the two-layer sea-floor has small effect on the simulated signal. By selecting appropriate values for the density and sound velocity of sea-floor, it is possible to have the same amplitude of the simulated pressure signature as the field recorded one. Therefore, we have scaled the signals to have the same amplitude as field recorded pressure signature for the nearest hydrophone and plotted in Figure 5.7 (left) for the cases without sea-floor and with two-layer sea-floor. Using the same scaling for the model, the simulated pressure signatures of these two cases are plotted for the next two shots in Figure 5.7 middle and right.

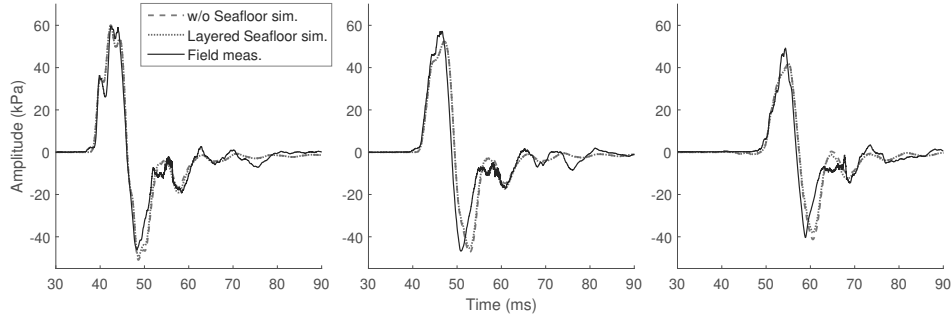


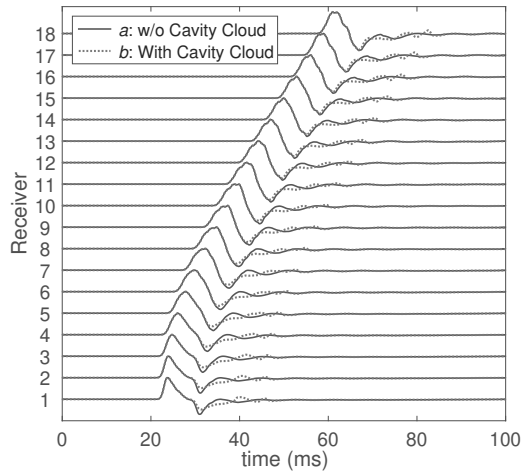
Figure 5.7: Comparison of simulation results without sea-floor, with a simple two layers sea-bed and the field measurements for three shot-receivers: (Left) closest shot receiver when the air-gun array has passed ($x=1.2$ m); (Middle) next shot after closest shot-receiver. The air-gun array is 26.2 m after the hydrophone ($x=26.2$ m); (Right) air-gun array is 51.2 m after the hydrophone ($x=51.2$ m).

The simulation results indicate that including a layered sea-floor with selected acoustic properties has an insignificant effect on the recorded pressure by the hydrophone located at the sea-floor. The selected acoustic properties seem to be realistic since the simulation in the paper refers to areas with the presence of typical sea-floor sediments.

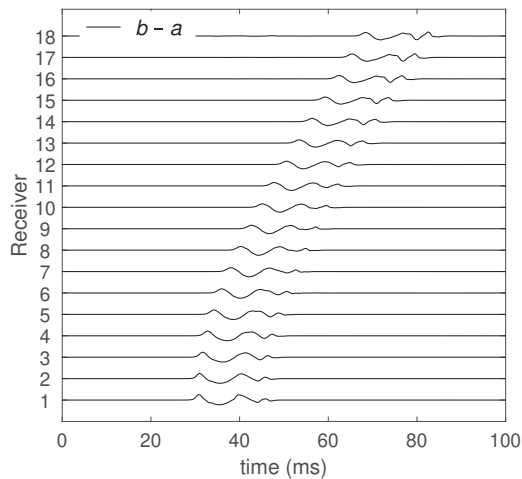
5.6.3 Effects of local time-dependent medium around the source array

We assume a ghost-induced cavity cloud being represented by an ellipsoid with dimensions ($R_x = 6m$, $R_y = 5m$, $R_z = 3.5m$) centered one meter above the center of an air-gun array. The array configuration is shown in Figure 5.3 (bottom) and it is towed at 5 m depth. In this section we want to numerically study the effects of temporarily sound velocity drop within the ellipsoid on the received acoustic pressure by a receiver array beneath the source. In this example, we assume that the sound velocity within the ellipsoid drops to 500 m/s 11 ms after the air-gun array is fired and raises back to 1500 m/s 8 ms later. The array consists of 18 receivers and are arranged along a line 30 m below the source array in the x-direction with 5 m spacing between two successive receivers. This means that the x-offset between array center and the first receiver is zero and it is 85 m for the eighteenth receiver. The received acoustic signals by 18 receivers in a stationary medium (i.e. no change in the medium properties) and in a time-dependent medium are modeled and plotted after normalization by solid blue and red dashed lines, respectively in Figure 5.8 (top). The difference between these two simulated signals for each receiver is shown in Figure 5.8 (bottom) without normalization. This figure shows the net effect of the sound velocity drop within the ellipsoid on

the recorded acoustic pressure by the receiver array.



(a)



(b)

Figure 5.8: (Top) Modeled acoustic pressure received by an array at different receivers without (solid blue) and with (dashed red) temporary sound velocity drop within an ellipsoid around the source array. The ellipsoid dimensions are ($R_x = 6m$, $R_y = 5m$, $R_z = 3.5m$) and is centered at ($C_x = 0$, $C_y = 0$, $C_z = 4m$) ($C_x=0$, $C_y=0$, $C_z=4$ m). All curves are normalized to one. (Bottom) Difference between the blue and red curves shown in the left. These are the effects of temporarily sound velocity drop within the ellipsoid.

For the given source array, the assumed ellipsoid dimension, and the assumed

sound velocity drop within the cloud for the given time duration, the amplitude of pressure fluctuations is between 16-25 % of the array signature peak amplitude at different receiver locations. It is observed that in both figures the arrival time of acoustic waves has the expected hyperbola shape.

5.7 Results

Two different methodologies are used to include the effects of vapor cavities in the numerical simulation of recorded pressure from a seismic air-gun array. (1) Vapor cavities temporarily drop the sound velocity within a fixed ellipsoid, and (2) the pressure field around the air-gun array is modeled based on air-gun array modeling and sound velocity drops at those regions where pressure drop fulfills the requirements for cavity generations. The obtained results based on these two methodologies are presented in the following sections.

5.7.1 Cavity cloud as a fixed ellipsoid

An ellipsoid with dimensions ($R_x = 6m$, $R_y = 5m$, $R_z = 3.5m$) centered at ($C_x = 0$, $C_y = 0$, $C_z = 4m$) fixed in the space is shown in Figure 5.9 (top) representing the collection of cavities as an effective medium. For the given array configuration (Figure 5.3), the cavity cloud appears ~ 10 ms after the air-guns are fired (Figure 5.4 in Khodabandeloo et. al., 2017) and considering 4-5 ms average cavity lifetime, it lasts for around ~ 8 ms. Since the air-gun signatures modeled by NUCLEUSTM are zero for around $\sim 1-2$ ms before they are fired, the sound velocity of the ellipsoid drops between 12 to 20 ms to have the correct cavity cloud timings relative to the air-gun firing. Using a step function to change the sound velocity causes numerical instabilities. Therefore, the sound velocity drop and subsequent rise occur within a short time with a sigmoidal shape function. Such a sound velocity drop for four different values is shown in Figure 5.9 (bottom). As seen for one of the cases shown by the dashed blue line the sound velocity within the cloud does not change and remains at 1500 m/s in the simulation.

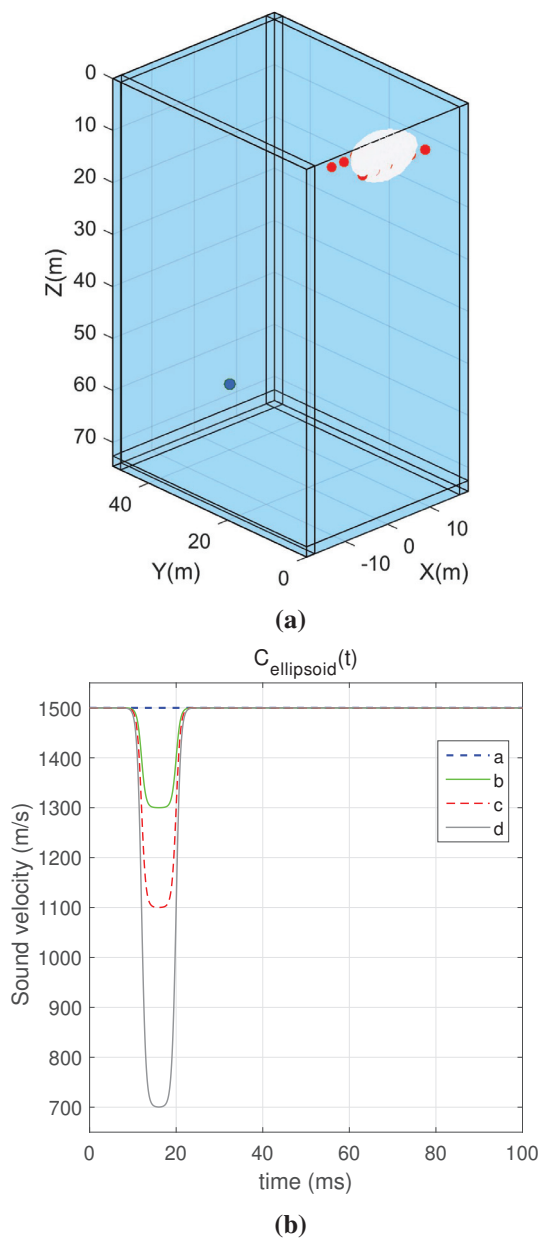


Figure 5.9: (Top) The air-gun array is shown by red dots and the receiver by a blue dot. The fixed ellipsoid ($R_x=6$, $R_y=5$, $R_z=3.5$) centered at $(C_x=0, C_y=0, C_z=4)$ resembling collection of cavities is shown in white near the source. (Bottom) The sound speed of the ellipsoid as a function of time for four different values. For case "a" sound velocity within the ellipsoid is constant and equal to that of water (1500 m/s). For "b", "c", and "d" the sound velocity is 1500 m/s before ~ 10 ms and after ~ 22 ms but between ~ 10 to ~ 22 ms drops to 1300, 1100, and 700 m/s, respectively.

The modeled pressure field snapshots at planes $Y=0$ (XZ plane) and $X=0$ (YZ plane) (Figure 5.5) at six time instants are shown for the case in which there is no sound velocity change in the ellipsoid (Figure 5.10) and when the sound velocity drops to 700 m/s (Figure 5.11).

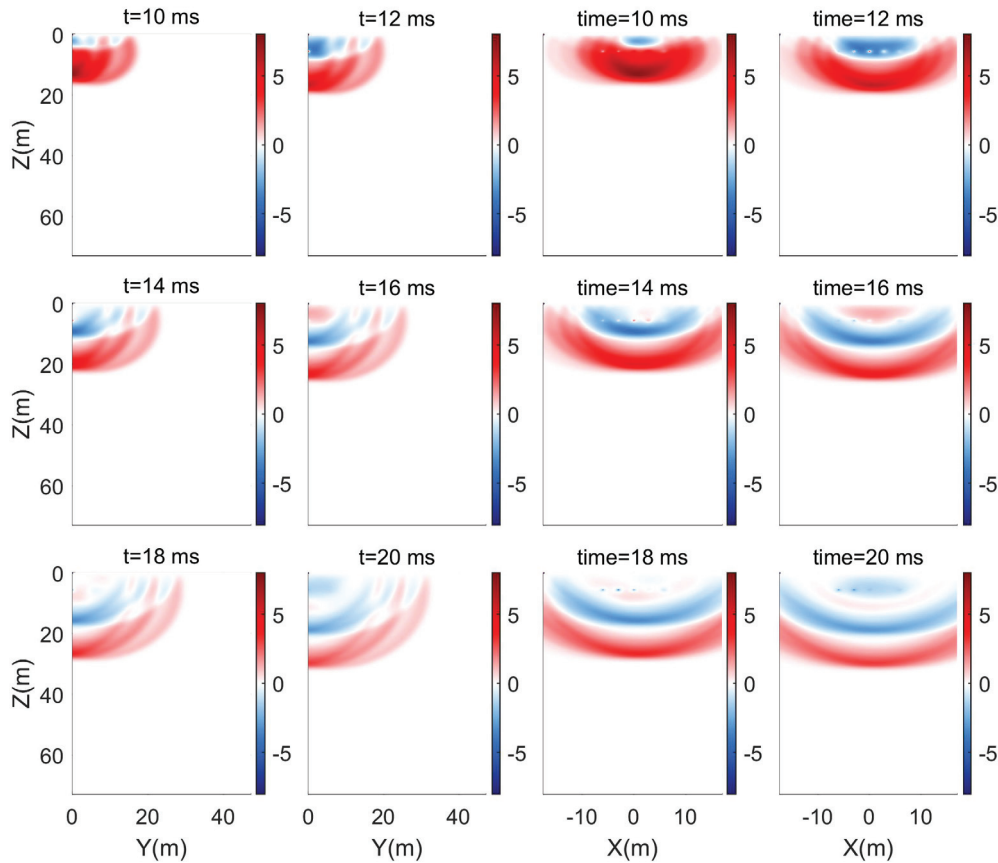


Figure 5.10: Pressure field at six time instants on YZ and XZ planes (see Figure 5.5) for the case when the sound velocity within the ellipsoid remains the same as water. The color-bar shows the acoustic pressure in bar.

The color bar shows the acoustic pressure in bar. The red and blue colors represent positive and negative pressures, respectively. It is seen that the positive pressure reflected from the sea-surface becomes negative. Furthermore, the directionality of the air-gun array is observed which directs more acoustic energy downwards than horizontally. In this figure, the sound velocity of the whole computational domain is 1500 m/s and it is time-independent. If the sound velocity within the ellipsoid

drops, then part of the incident wave will be reflected with opposite polarity. The pressure fields for this case are shown in Figure 5.11 where the ellipsoid sound velocity drops to 700 m/s for times between 12 and 20 ms (which corresponds to ~ 10 to ~ 18 ms after the array is fired). The effects of local change in the medium are observed as pressure field differences between Figure 5.10 and Figure 5.11 for the time interval between 14 and 20 ms.

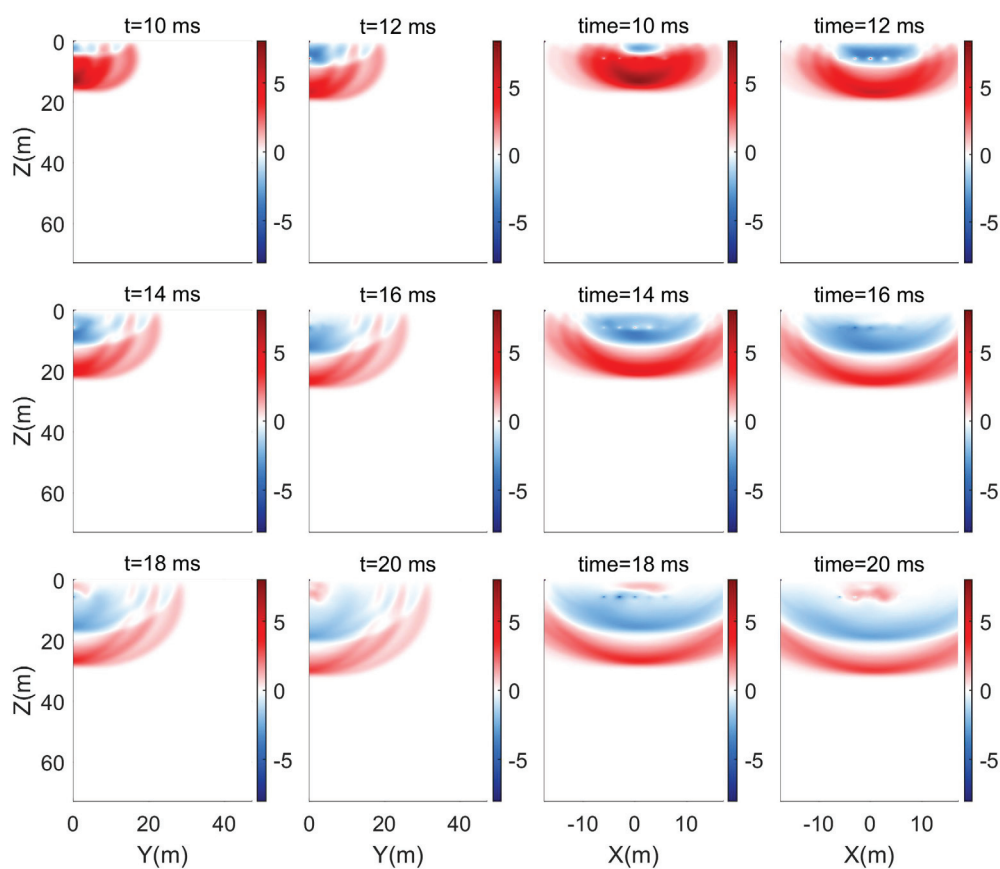


Figure 5.11: Pressure field at six time instants on YZ and XZ planes (see Figure 5.5) for the case when the sound velocity within the ellipsoid drops to 700 m/s for a short time as shown by gray solid line in Figure 5.9 (bottom). The color-bar shows the acoustic pressure in bar.

To see the effects of the sound velocity reduction within the ellipsoid on the pressure fields, the difference between the pressures shown in Figure 5.10 and Figure 5.11 are plotted in Figure 5.12.

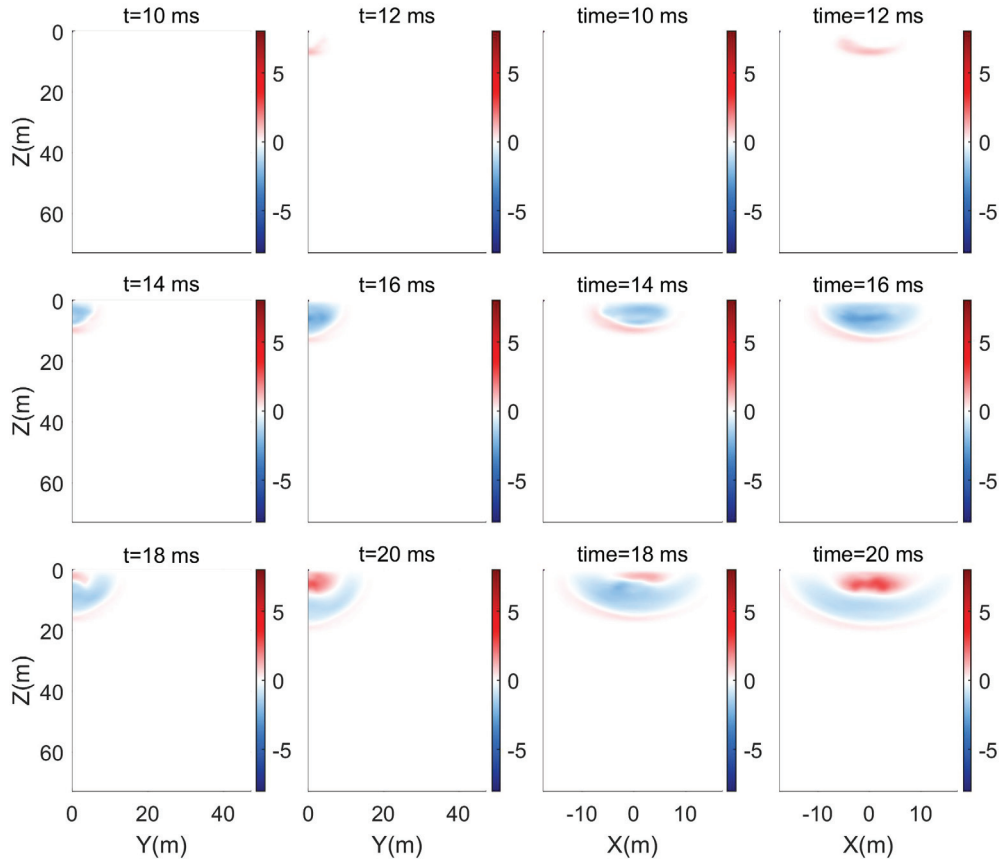


Figure 5.12: Difference between Pressure fields on YZ and XZ planes shown in Figure 5.10 and Figure 5.11.

In addition to changing the sound velocity within the ellipsoid to 700 m/s, it was also changed to 1100 and 1300 m/s and the received acoustic pressure was simulated. The simulation results are plotted in Figure 5.13 together with the recorded field experiment.

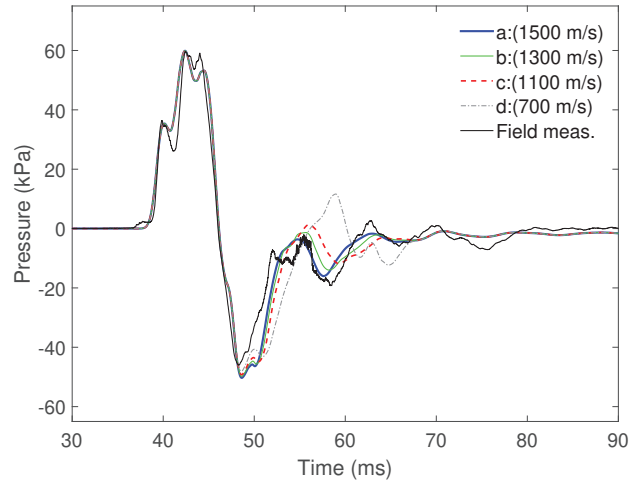


Figure 5.13: The simulated pressure at receiver location for the case when sound velocity within the ellipsoid shown in Figure 5.9 (top) remains the same as water (1500 m/s) (a), drops to 1300 m/s (b), 1100 m/s (c), 700 m/s (d). The recorded pressure in the field experiment is also shown by a solid black line.

The blue solid line is for the case when the ghost cavity cloud does not change the sound velocity of the medium. It has the best agreement with the recorded field measurement signal shown by black color. It is seen that reducing the sound velocity within the ellipsoid deteriorate the match between simulated and measured field data. Further reducing the sound velocity makes the correspondence poorer. We will elaborate on this observation in the discussion.

5.7.2 Cavity cloud modeling based on modeled pressure values

In this section, unlike the previous section where the cavity cloud was considered to be a fixed ellipsoid, it is assumed that cavities will grow at regions where the pressure (hydrostatic + acoustic pressure) drops below -0.1 bar. It should be noted that pressure values below zero are physically impossible. However, the air gun modeling software is based on the linear superposition of the ghost signals created by all the guns in the array, and hence the software will predict unphysical pressure values. We can use these artificial negative pressure values as constraints to predict the regions where cavity creation is likely to occur. The case where sound velocity within the cavity cloud drops to 900 m/s is shown in Figure 5.14 at four time instants. It is observed that the shape of cloud changes over time. To prevent numerical instabilities, the sudden change in the medium properties should be avoided. Therefore, the implementation of this case is more demanding than

modeling cavity cloud as fixed ellipsoid as shown in the previous section.

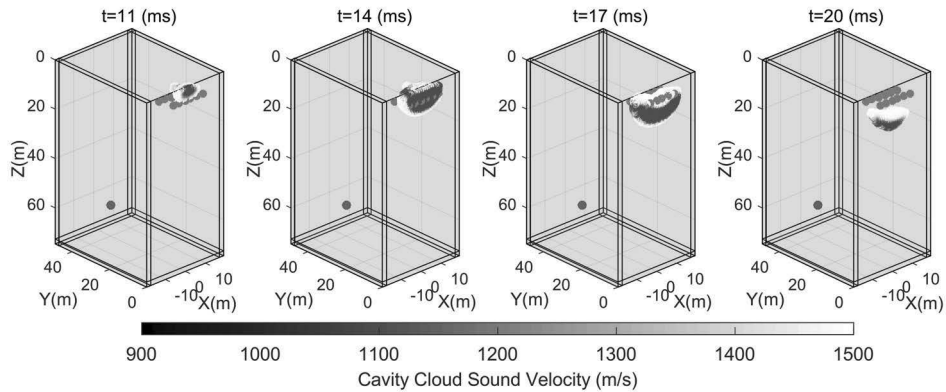


Figure 5.14: Modeled cavity cloud at four time instants where the pressure drops below -0.1 bar. In this case it is assumed that the sound velocity within the cavity cloud reduces to 900 m/s.

The regions which contain cavities are then considered as a time-variant effective medium with acoustic properties different from the host medium. That is the sound speed of grid points which satisfy the conditions for cavity growth is temporarily reduced to a certain level. The sound velocity reduction occurs within a short transition time using a sigmoidal shape function. Different values are assigned to sound velocity of the cavity cloud: 1300 m/s, 1100 m/s, 900 m/s and no sound velocity drop. For the case where the sound velocity of the cavity cloud drops to 900 m/s, Figure 5.15 shows the pressure field for six time instants at the $Y=0$ plane (XZ) and $X=0$ plane (YZ).

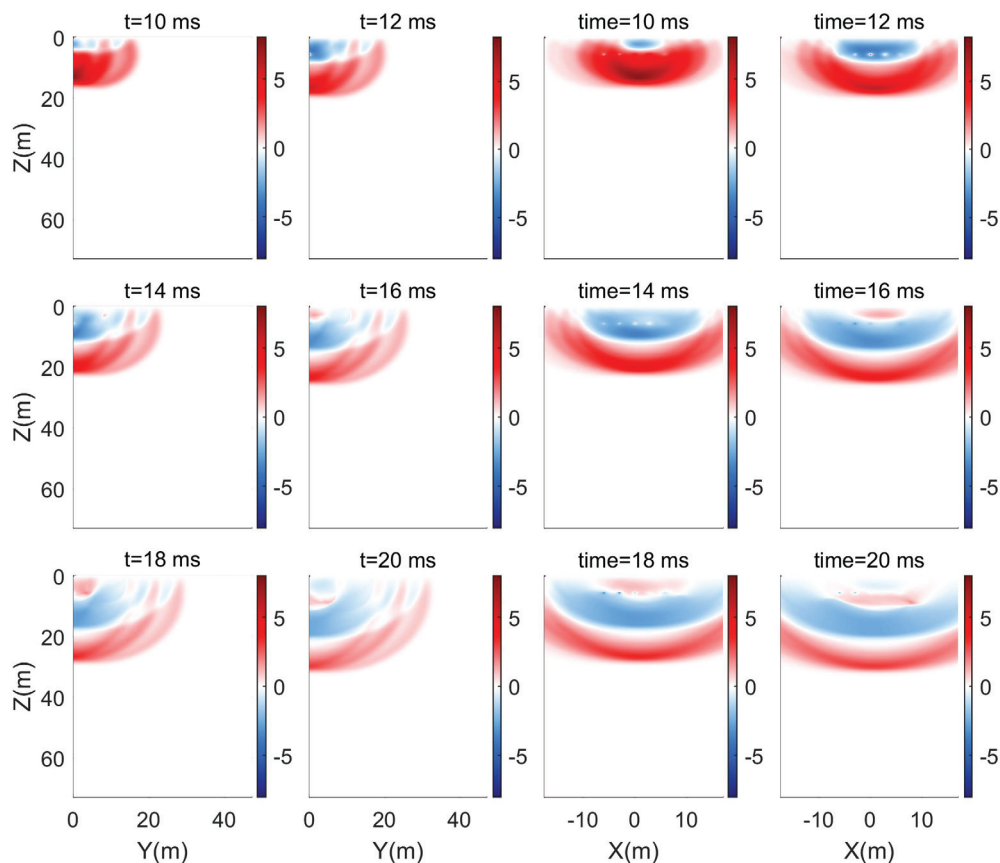


Figure 5.15: Pressure field at six-time instants on YZ and XZ planes (see Figure 5.5) for the case when sound velocity within the cavity cloud drops to 900 m/s. The cavity cloud forms at locations where the pressure (hydrostatic + acoustic pressure) falls below -0.1 bar and diminishes when the pressure increases above this threshold.

Since the medium properties change differently compared to the fixed ellipsoid case, the pressure fields in this case (Figure 5.15) are different compared to the previous cases as was shown in Figure 5.10 and Figure 5.11. The simulated acoustic pressure at the receiver point for different values of sound velocities within the cavity cloud are shown in Figure 5.16. As for the previous case, including the sound velocity drop within the cavity cloud worsens the match between simulated and field measurements. The possible explanations for this observation are given in the discussion section.

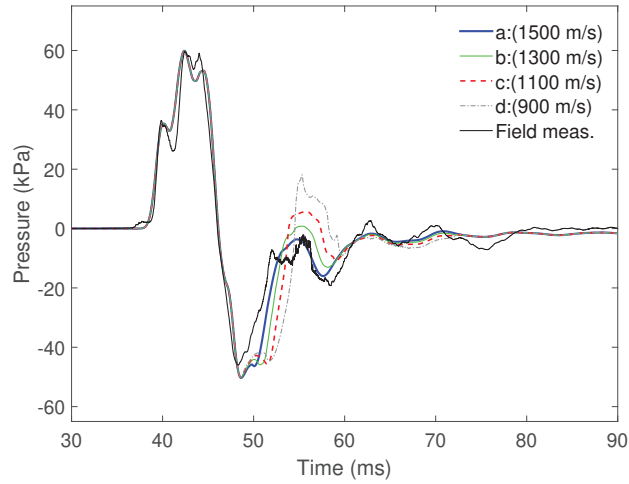


Figure 5.16: The simulated pressure at receiver location for different values of sound velocity within the cavity cloud. The cavity cloud forms at locations that the pressure drops below -0.1 bar and diminishes when the pressure increases above this threshold. Sound velocity values within the cavity cloud drops to: 1500 m/s (the cavity cloud has no diffraction effect), (b) 1300 m/s, (c) 1100 m/s, and (d) 900 m/s. The recorded pressure in the field experiment is shown by a solid black line.

5.7.3 Including ghost cavitation signal in the modeling

Simulations show that the signal due to collapse of multiple cavities within the cavity cloud contains low frequencies in addition to the high frequencies (Khodabandeloo and Landrø, 2017a,b). The ghost cavitation signal is simulated (Khodabandeloo et al., 2017, Khodabandeloo and Landrø, 2017a) and plotted by purple dashed-dotted line in Figure 5.17 and the rest of the curves are resulted from adding this signal to the curves in Figure 5.13.

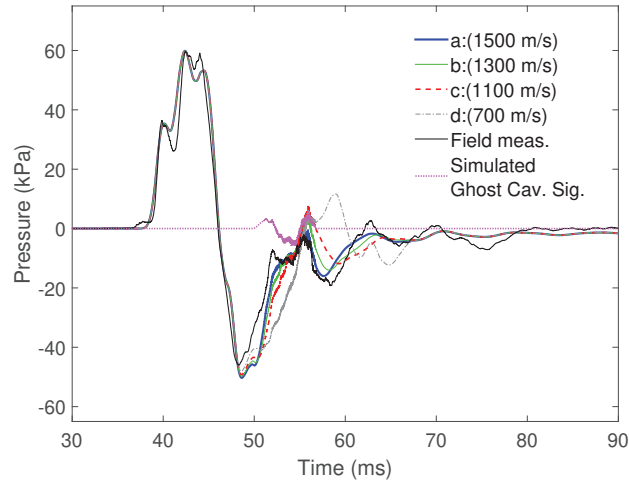


Figure 5.17: The simulated pressure at receiver location + simulated ghost cavitation signal for the case when sound velocity within the ellipsoid shown in Figure 5.9 (top) remains same as water (1500 m/s) (a), drops to 1300 m/s (b), 1100 m/s (c), 700 m/s (d). The recorded pressure in the field experiment is also shown by solid black line.

It is observed that adding the effects of ghost cavitation signal to the far-field array signatures best matches for the case when sound velocity of cavity cloud – represented by ellipsoid – is same as the surrounding water. There will be a poorer correspondence between the simulation and field data when the sound velocity within the ellipsoid is decreased. The same conclusion will be drawn if we add the simulated ghost cavitation signal to curves plotted in Figure 5.16. That means that the drop of the sound velocity within the cavity cloud deteriorates the correspondence between simulated far-field and field recorded signatures.

5.8 Discussion

The cavity cloud is modeled as an effective medium with smaller sound velocity than water or air. Attenuation is not included within the cavity cloud. For 1% void fraction, ($\beta = 0.01$), in the frequency range of our problem the attenuation is around 1 dB/m (Zhang et al., 2017). In our case, as is discussed below, the void fraction is 4 to 5 orders of magnitude lower. Due to this fact and considering that the size of the cloud is not exceeding a few meters, the attenuation effects of cavity cloud is expected to be negligible and therefore it is ignored in our modeling.

Simulation results indicate that even 10-15% decrease in the sound velocity of medium for a short time in a small part of the medium around the air-gun array slightly affects the far-field recorded acoustic pressure. Comparing the simulation

results to the field measurements suggests that the acoustic properties within the ghost cavity could not be significantly different from those of the surrounding water. Based on the effects of sound reduction in low-frequency region for gas-vapor cavities as seen in Figure 5.2 one possibility is that the volume fraction of vapor cavities is less than $\sim 10^{-7}$ for a vapor fraction equal to 0.99, while it is less than $\sim 5 \times 10^{-7}$ for vapor fraction equal to 0.95. In the ghost cavitation modeling with the same grid resolution as we used here, the initial number of cavities were scaled by the factor of 0.07 (Khodabandeloo and Landrø, 2017a) to match the measured field data. Then for a vapor fraction $Y_0 = 0.99$ the mean cavity radiuses must be $r = (0.2^3 \cdot 10^{-7} / (0.07 \cdot \pi \cdot 4/3))^{1/3} = 1.4 \text{ mm}$ to have the volume fraction less than $\sim 10^{-7}$ and for $Y_0 = 0.95$ it must be 2.4 mm to have the volume fraction less than $\sim 5 \times 10^{-7}$.

It is possible to roughly estimate the upper bound for the number of cavities (N_{\max}) and the volume fraction of vapour cavities based on the amount of the acoustic energy on a plane located horizontally at depth z_0 (Figure 5.19), shown by $E_a|_{z_0}$, that can induce cavitation. It can be estimated using the following formula for the acoustic energy created by the down-going wave that has been reflected at the free surface:

$$E_a|_{z_0} = \int_A \int_{t_1}^{t_2} \frac{P^2((x, y, z = z_0), t)}{\rho_0 c} dt dA \quad (5.12)$$

In the above formula, $P^2((x, y, z = z_0), t)$ is the portion of acoustic pressure on a plane at depth z_0 that has potential to induce cavities. That is amount of the acoustic pressure which drops the pressure below the assumed threshold pressure (e.g. -0.1 bar). The time interval of the integration, t_1 and t_2 are the time when the P drops below the threshold limit for cavitation generation and the area on the plane where the pressure is low enough for cavity generations is given by A . For the array configuration given in this paper, the maximum amount of E_a is found at the depth of 3.8 meters and is estimated to be 1194 Joules. The pressure values that drop below the threshold on the assumed plane at depth $z_0=3.8\text{m}$ are shown in Figure 5.18 at four time instants.

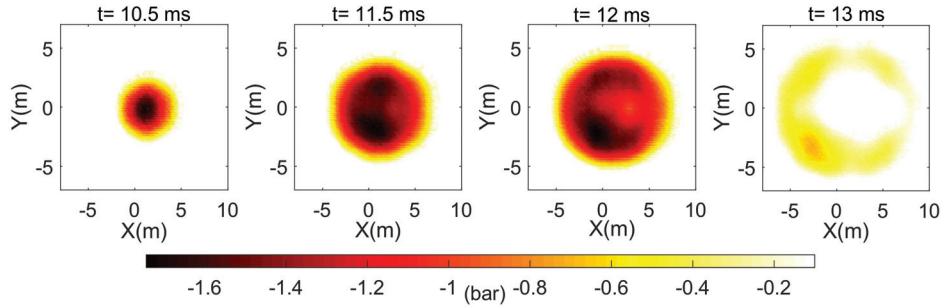


Figure 5.18: Pressure values at four time instants that drop below -0.1 bar (i.e. the assumed threshold pressure for cavity generation) on a horizontal plane located at depth $z_0=3.8$ m (shown schematically by green in Figure 5.19)

The maximum number of cavities N_{\max} , can be estimated as:

$$N_{\max} = \frac{E_a}{p_h V} \quad (5.13)$$

Where p_h is the hydrostatic pressure at the assumed depth ($=3.8$ m), and V is the average volume of each cavity. Assuming the average radius of cavities as 5 mm, and a cloud as an ellipsoid with dimensions of $R_x=6$ m, $R_y=5$ m, $R_z=3.5$ m, $N_{\max} = 16623$, and the corresponding maximum volume fraction of vapour cavities is estimated to be $\sim 2 \times 10^{-5}$. If we assume that most of the acoustic energy is maintained, it means that the number of cavities in reality is probably significantly less than this. We emphasize that this is a rough estimation for the maximum possible volume fraction of vapor cavities within the cloud. It is observed that the estimated volume fractions from the far-field acoustic recordings given in this paper, are below this limit which is a confirmation of the results.

The array studied in the example in this paper produces less than half of ghost cavitation compared to another array with almost same seismic energy but different air-gun arrangement (Khodabandeloo and Landrø, 2017b). Hence, for the arrays with stronger ghost cavity cloud than the one in our example, sound velocity reduction within the cloud can be a source of deviation between modeled and measured source array signature after the reflected ghost occurs.

To characterize the acoustic properties of a cavity cloud we suggest an experiment which is schematically shown in Figure 5.19. Two acoustic transducers, one well above and the other beneath the air-guns, are required to generate harmonic pressure waves. A hydrophone is required to be mounted below the acoustic transducer 2 to receive the generated acoustic wave by the transducers.

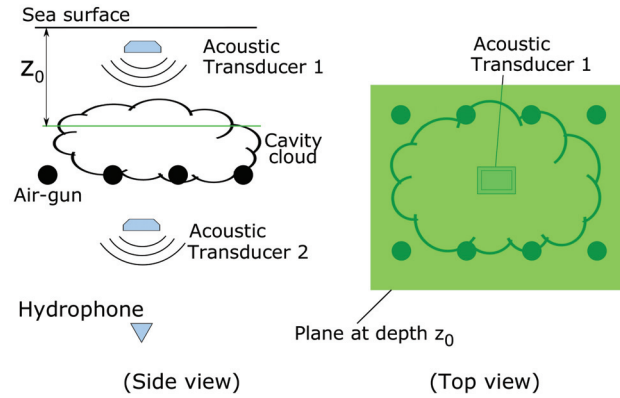


Figure 5.19: The schematic of proposed test setup to characterize the acoustic properties of ghost cavity cloud. (left) side view of the test setup and (right) top view. The green plane located at depth z_0 is for explanation of Equation 5.12.

In the first set of experiments, while transducer 2 is inactive, transducer 1 should generate a harmonic wave with a frequency above the seismic frequency band. This allows to use filters to separate the acoustic signal from the transducer from the air-gun(s) pressure signal received by the hydrophone. The transducer should generate harmonic wave continuously for several, e.g. 20, air-gun shots. In the second set of experiments, the only difference is that transducer 2 is active and generates a harmonic wave as in the first set of experiments while transducer 1 is inactive. The second set of experiments are required to investigate the possible effects of air-gun pressure field on the transducers. For example, we may observe that in the first experiment the amplitude of the received harmonic wave by the hydrophone weakens when the ghost cavity cloud is expected and recovers afterward. This can be due to either the reflection of acoustic waves reaching the cavity cloud or the impact of air-gun pressure waves on the performance of the transducer. The second experiments help to remove these uncertainties. Since the air-guns generate strong acoustic waves, to avoid the saturation of received signals one solution is to have the hydrophone far enough below the air-guns.

5.9 Conclusion

Effects of sound velocity drop within the ghost cavitation cloud on the far-field recorded acoustic pressure is numerically simulated. The modeled cavity cloud appears around 10 ms after the air-gun array is fired and lasts for around 9 ms. This is confirmed by high-speed video recording. Wave propagation in a non-stationary (time-dependent) medium is modeled using k-wave which is a k-space

pseudo-spectral numerical method to solve the acoustic wave equation. Few modifications are applied to the source code to accommodate the time-dependent sound velocity of the medium. Modeling results are compared to the recorded field data. When there is no sound velocity drop within the cavity cloud, there is a good correspondence between the simulation results and the recorded field data. It is observed that if sound velocity within the cavity cloud drops below 1200 m/s, the correspondence between the modeled acoustic signature and field measurement worsens. Simulation results show that a 40% reduction of the water sound velocity within the cavity cloud affects the acoustic far-field pressure significantly.

5.10 Acknowledgment

This research is funded by Research Center for Arctic Petroleum Exploration (AR-CEX) partners, and the Research Council of Norway (Grant No. 228107). Authors thank Statoil and CGG for funding the experiments for video recording the ghost cavity cloud and permission to present them. ML acknowledges financial support to the ROSE project at NTNU from the Norwegian Research Council (Grant No. 228400).

Chapter 6

Concluding Remarks

The main objective of this doctoral work has been to investigate the underlying mechanism(s) for high-frequency (>10 kHz) acoustic signal generated by marine seismic air-gun arrays. Ghost cavitation was hypothesized to be the main source of such high-frequencies. Ghost cavitation consists of several acoustically induced cavities which are formed due to the pressure drop as a result of reflected pressure waves, i.e. ghost, from the sea surface. Reducing the waste high-frequency emissions from seismic air-gun arrays can benefit the marine environment by reducing the seismic survey impacts on marine mammals with sensitive high-frequency hearing. Having a reliable technique for ghost cavitation will be a useful tool to find solutions to reduce such high frequencies.

In paper 1 (chapter 2), A synthetic modeling scheme for simulation of acoustically induced cavitation in seismic air-gun arrays was developed. The model was validated by comparing the simulation results to field recorded acoustic signals. The locations around the array where the pressure drops below certain level were estimated based on superposition of pressure fields from the air-guns in the array. At each grid-point where the pressure drop was sufficient for cavity formation, it is assumed that only one cavity grows and collapses governed by Prosperetti bubble dynamics equation. The interaction between the pressure fields from collapse of neighboring cavities was disregarded. However, a good agreement between the onset and duration of the high-frequency modeled and measured signals was observed. Same as what was observed in the field measurement, time duration of high-frequency simulated signal increases by increasing the incident angle (with respect to vertical). The correspondence between the envelope shape of simulated and measured high-pass filtered signal was improved by including a simple

model for effects of pressure fields from former cavity collapses. Since the cavitation generates high-frequencies, our modeling technique is computationally less expensive than finite difference or finite element to model cavity collapse and its propagations.

In paper 2 (chapter 3), using the numerical modeling scheme, high-frequency emissions caused by ghost cavitation for two different air-gun arrays were compared. Both arrays consist of three sub-arrays. Sum of the air-chamber volumes of the air-guns in one of them was 2730 in³ and the distance between the sub-arrays was 6m. The total air-chamber volumes for the second array was 3250 in³ and the distance between sub-arrays is 8m. Array with larger volume is expected to have stronger ghost cavitation. On the other hand, array with larger sub-array distance should generate weaker ghost cavitation. The numerical results indicate the second array generates around 150% more high-frequencies (>5 kHz) while its energy in the seismic band is only around 20% more than the smaller array. It was observed that in both arrays the signals due to ghost cavitation contain some low-frequency components.

In paper 3 (chapter 4), in a field experiment ghost cavitation was recorded by a high-speed video camera which provides an undebatable evidence of the phenomena. To the best of our knowledge it is the first convincing photography of the ghost cavitation cloud. The ghost cavitation modeling scheme was tested to see whether it can predict the observed patterns of imaged cavity cloud. It was observed that the modeled cavity cloud resembles the general features and patterns of the imaged cloud as well as its onset time and duration. In addition, the resulting high-pass filtered signal from simulation was compared to the measured one in the field experiment. They had a very similar envelope shape and duration. The agreement between simulated and recorded high-pass filtered signals was further improved when the cavity reflections from the sea surface were included in the modeling by a reflection factor of -0.4.

In paper 4 (chapter 5), sound velocity within the cavity cloud was investigated using a k-space pseudo-spectral numerical method. It is well known that presence of vapor cavities – or bubbles – within a liquid has potential to change the sound velocity of the host medium significantly. If frequency of the propagating wave is below the resonance frequency of the cavities or bubbles, the speed of sound decreases in the medium. Since the cavities appear for a short period of time, the wave propagation takes place in a time-dependent non-stationary medium. Numerical results indicate that if the cavities change the water sound velocity more than 40%, it impacts the array signature significantly after the direct peak arrival. This can adversely affect the seismic imaging. However, for the array configuration and corresponding field data set that we studied, it was concluded that sound velocity

drop within the cloud should be less than 10-15% for the studied array.

Possible extension of the doctoral work presented here are the followings:

- The developed synthetic numerical scheme for ghost cavitation signal modeling must be calibrated such that the amplitude, frequency contents, and energy of modeled signals match those from field measurements. In order to achieve this purpose, I believe the first step is to tune the bubble dynamic equation such that the modeled signature from single cavity collapse matches the one from experiment.
- In our model, interactions between cavities is ignored. It should be investigated to what extent they interact and how much the interaction impacts the resulting signal.
- Ghost cavity modeling scheme should be used to estimate the amount of high-frequency signal due to ghost cavitation in eSource arrays. High-frequency emission by individual eSource is reduced by regulating the air release from air-gun ports and increasing the raise time. Despite the peak pressure of the resulting pulse is decreased, the pulse width is increased. Consequently the possibility of overlap with other eSources in the array is increased.
- Further dedicated field experiments are required to see the effects of array configuration on the amount of ghost cavitation signal. The broad-band hydrophones are required at several locations to record the acoustic signals without clippings. The results from these experiments are crucial in calibrating the ghost cavitation modeling scheme.
- Using high-speed cameras (> 480 fps) to record the ghost cavity cloud from two to three different angles. For example, from front and side view.
- To devise an experimental setup to measure the sound speed within the cavity cloud.

Appendix A

Effects of Ghost Cavitation Cloud on Near-field Hydrophones Measurements in the Seismic Air Gun Arrays ¹

Babak Khodabandeloo, Martin Landrø

*Department of Petroleum Engineering and Applied Geophysics,
Norwegian University of Science and Technology (NTNU)
NO-7491 Trondheim, Norway*

A.1 Abstract

Air gun arrays are the most common marine seismic sources and knowledge of their directional source signature is essential in several reflection seismology areas. Having the far-field signatures for different angles, it is possible to get higher quality seismic images by removing the source signature variation effects. It is challenging to measure far-field source signatures directly and therefore other methods are developed to estimate directional far-field signatures. Using near-field measurements for calculation of far-field signatures is a common technique. This method requires pressure measurements near each air gun in the array. On the other hand acoustic pressures of individual air guns reflected from sea surface can drop the hydrostatic pressure around the array and generate underwater vapor cavities. In

¹Paper Published at the 79th EAGE Conference and Exhibition 2017

this paper numerical simulation which is validated by field data is used to show the effects of several cavity collapses on the hydrophones used for near field measurements. Including other source of pressure fluctuations than the air guns and ghost signals, it is possible to better estimate the notional source signatures and eventually having better far-field array source signature computation.

A.2 Introduction

In reflection seismology knowledge of seismic source signature is essential in several areas. Some examples are: seismic inversion, time-lapse seismic, AVO (Amplitude versus offset) analysis (Amundsen, 2000). In addition, since it is possible to increase the signal to noise ratio through processing and subsequently extend the usable seismic frequency range, far-field signature estimation of seismic air-gun arrays is important (Williams and Pollatos, 2012).

Direct measurement of far-field marine source signatures is difficult and very costly. Hence other techniques are deployed to estimate the source signatures (Behura and Snieder, 2013). One of them is to compute the signature from near-field measurements using set of hydrophones placed close to the air-guns in the array (Ziolkowski et al., 1982). Such measurements provide us with the so called notional source signatures (Laws et al., 1998). To determine the notional source signatures, there should be at least same number of independent nearfield pressure measurements as the number of individual air-guns in the array (Parkes et al., 1984). Stability and reliability of farfield source signature computation from near-field measurements for different single subarray and full array was discussed by Landro et al. (1991). In the cases where stability was the issue, it was suggested to place the hydrophones closer to the guns.

Landrø (2011) reported that air-gun arrays produce substantial high frequencies compared to the single air-gun or single sub-array. Such high frequencies were attributed to ghost cavitation cloud (Landrø et al., 2011, 2013, 2016). Radiated pressures from air-guns in the array when reflected from water-air interface can drop the hydrostatic pressure at some regions in the water below zero depending on the air-gun array configuration. In those regions cavities are formed and their collapses generate high frequencies appearing with some delay after the main peak of array signature.

In this paper we use numerical simulation to show that the signal due to the ghost cavitation cloud, besides the high frequencies, also contains low frequencies. Ghost cavitation cloud affects the measured signals by hydrophones near the air-guns in the array which are used for notional source signature estimation. For the array size and configuration in our example the ghost signal generates pressure

fluctuations which appears few milliseconds after the main peak and has a duration of around 8 ms. Its magnitude is up to 20

A.3 Spatial and temporal distribution of pressure drops

Cavities can be formed due to pressure drop in liquids (Frohly et al., 2000). In seismic air-gun arrays, the reflected acoustic pressures of individual air-guns from sea surface can reduce the hydrostatic pressure below zero at some regions. Using the air-gun array same as the field experiment which was conducted in 2008 (Landro et al., 2013), the regions where hydrostatic pressure drops below -0.1 bar are plotted in three different time instants in Figure A.1. In the field experiment the source array with 2730 in³ air volume was towed by a shooting vessel in a straight line above the stationary hydrophone located at the seabed at the depth of around 55 m. The source was fired every 25 m. In the array there are both single and cluster guns. There are 10 inactive guns (spare) and are shown by dark blue while the active air-guns are shown by red.

A.4 Cavity collapse simulations

We assume that at each point in the computational domain when the hydrostatic pressure reaches its minimum and is below certain limit (e.g. -0.1 bar) a cavity grows and subsequently collapses. Pressure signature of such cavity collapse is calculated solving the bubble dynamic equation (Equation 2 and 3 in Versluis et al., 2000). The calculated peak pressure from single cavity collapse seems to be too high compared to the measured one in an experiment (Versluis et al., 2000) and hence we have reduced the peak pressures of cavity signatures by multiplying by 0.04. This scaling provides us with consistent scaling to fit the simulated and measured signals. Four different cavity collapse signatures obtained by solving bubble dynamics equations are shown in Figure A.2.

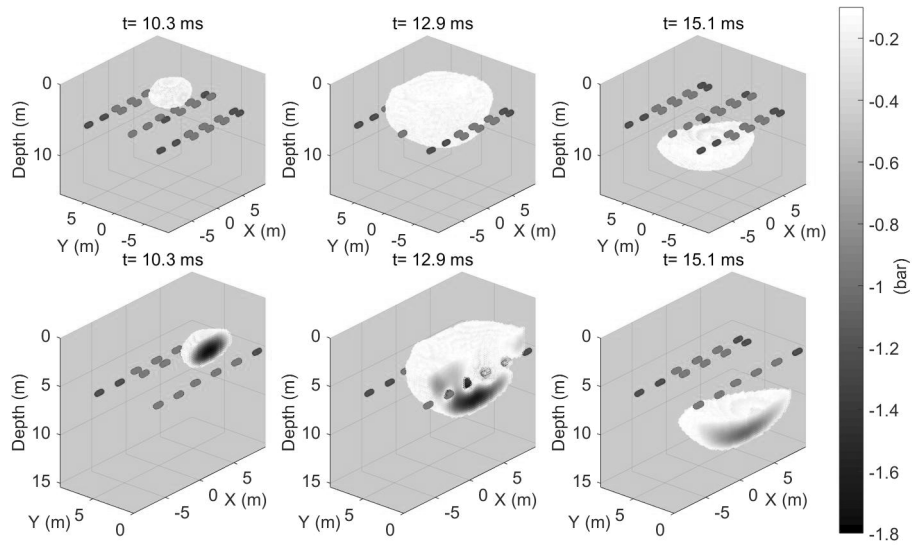


Figure A.1: Top row: Spatial and temporal distribution of regions where the total hydrostatic pressure drops below -0.1 bar. Bottom row: cut section (y-direction) of top row.

Having time, location and signatures of cavity collapses from previous steps, it is possible to estimate the measured signal from several cavity collapses at any desired location by propagating the cavity signatures to the measurement point. Having the source-receiver distance geometrical spreading is considered. Absorption effects were also considered by estimating the attenuation coefficient from the formula given by Francois and Garrison (1982).

A.5 Comparison of simulated and field measured signals

The model was tuned to fit the field measurement. Using 0.07 as scale factor for the simulated data both the 10 kHz high frequency and raw simulated ghost cavitation signal fits reasonably with the measured signal in the field experiment. The result for unfiltered data is shown in Figure A.3.

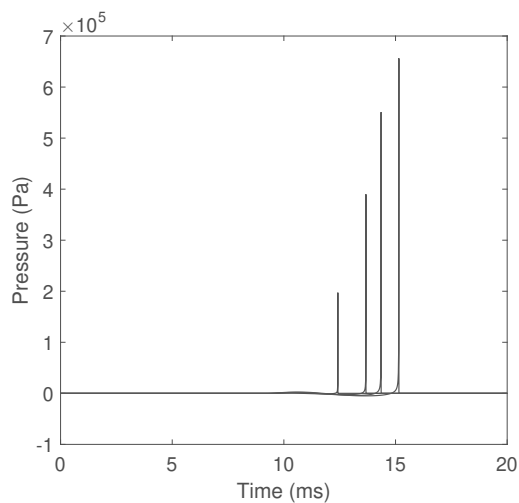


Figure A.2: Four different cavity collapse signatures estimated by solving the bubble dynamics equations subjected to external pressure drops at different points in the computational domain. The peak pressure is scaled by 0.04.

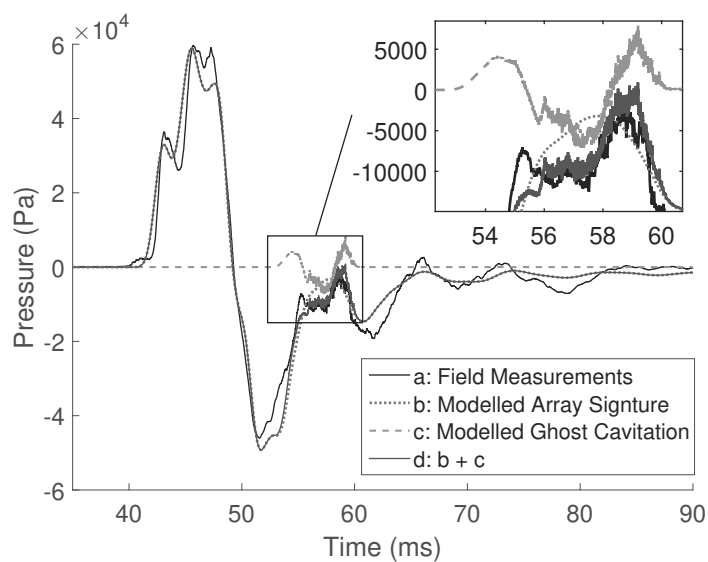


Figure A.3: Comparison of field measurement and the computed array signature and ghost cavitation signal for the same configuration as field setup. Considering ghost cavitation signal improves the fit between simulation and field measurement as shown in the rectangle in the figure.

It is observed that inclusion of ghost cavitation cloud effects together with the array signature improves the agreement between the modeled and field measured data.

A.6 Nearfield hydrophone signals simulation

In the field experiment there was no near field hydrophone to measure the acoustic pressure in the array. To see the possible effects of ghost cavitation cloud on the hydrophones measuring acoustic pressure near the air-guns in the arrays we have used our model which is validated by field experiment as discussed in the previous sections (see Figure A.3). Having the tuned model, signal at nearfield hydrophones are simulated with and without ghost cavitation cloud. The results for nearfield hydrophone located at the distance of 1 meter above air gun number 16 are plotted in Figure A.4 for 125 kHz sampling rate and 500 Hz low passed filtered signals. Air-gun number 16 is the one in the middle of the array that we have used in our example. It is observed that with 125kHz sampling rate, there will be a intense peak in the nearfield hydrophone due to collapse of possible cavities in the vicinity of hydrophone. However in many measurement systems a 2ms sampling is used and the low passed filtered signals (cutoff frequency=500 Hz) are given in figure A.4 (right). It is observed that the low passed filtered signal of ghost cavitation cloud has same magnitude as the ghost signal of the array for the hydrophone in the middle of array and is up to 20 % of array signature main peak. The ratio of rms value of modelled ghost cavitation signal to the array signature for the first 22 ms is equal to 19.8

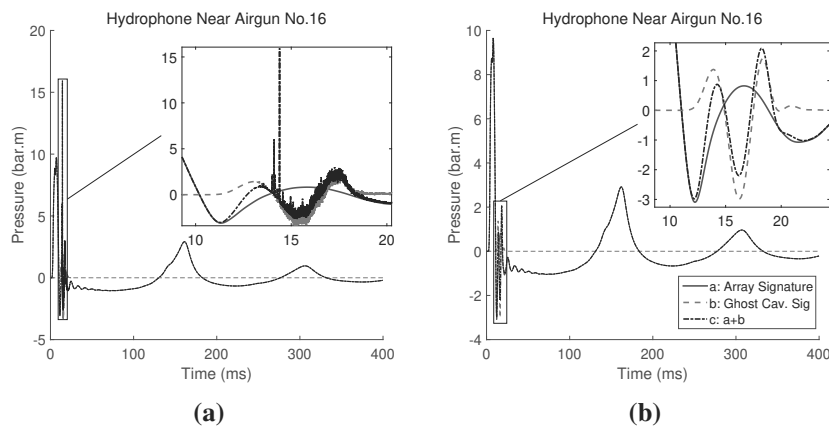


Figure A.4: Simulated signals at hydrophone considered 1 meter above air-gun No 16 which is the air-gun in the middle of the array. The array signature (solid blue), ghost cavitation signal (dashed red), and their combination (dashed dotted black) are plotted. 125 kHz sampling frequency (left) and 500 Hz Low Passed filtered (Right) signals.

A.7 Conclusions

Measurement of far-field source signatures is difficult but crucial in several reflection seismology areas. Instead of direct measurement of source signatures, other techniques are developed. One of them is to calculate the far-field source signature from near field measurements. On the other hand it is known that air-gun arrays generate high frequencies which are ascribed to ghost cavitation cloud. Collapse of several underwater vapor cavities produces intense high frequencies. In this paper by comparing the simulated data and field measured signals it was shown that ghost cavitation signal contains low frequencies as well. The model was then adjusted to match the field measurement. Using the tuned model, it was observed that ghost cavitation cloud possibly impacts the nearfield hydrophone measurements. Cavity collapse near the hydrophones may produce intense peak pressure measured by the hydrophones. However when using typical 2 ms sampling in seismic data acquisition systems, such intense peaks are not recorded while low frequency is still considerable. In our example, simulation results show a low frequency component which has magnitude of up to 20 % compared to the main peak of the array. The ratio of rms value of modelled ghost cavitation signal to the array signature for the first 22 ms is equal to 19.8 %. Our model indicates that ghost cavitation cloud signal has low frequency contents and could distort the notional source signature estimation after the main peak. Including effects of ghost cavitation cloud on the near-field hydrophones slightly improves accuracy of notional source signature estimations which means better far-field array signature computation. However, for the available data we do not have near-field measurements to confirm the hypothesis.

A.8 Acknowledgements

This research is funded by Research Center for Arctic Petroleum Exploration (AR-CEX) partners, and the Research Council of Norway (grant number 228107).

References

- Abadi, S.H., Tolstoy, M. and Wilcock, W.S., 2017. Estimating the location of baleen whale calls using dual streamers to support mitigation procedures in seismic reflection surveys. *PloS one*, **12**(2), p.e0171115.
- Abma, R. and Ross, A., 2013, January. Popcorn shooting: Sparse inversion and the distribution of airgun array energy over time. In 2013 SEG Annual Meeting. Society of Exploration Geophysicists.
- Abma, R. and Ross, A., 2015, December. Practical aspects of the popcorn source method. In 2015 SEG Annual Meeting. Society of Exploration Geophysicists.
- Abma, R., Howe, D., Foster, M., Ahmed, I., Tanis, M., Zhang, Q., Arogunmati, A. and Alexander, G., 2015. Independent simultaneous source acquisition and processing. *Geophysics*, **80**(6), pp.WD37-WD44.
- Amundsen, L., 2000. Linear inversion for source signatures from ministreamer data. *The Leading Edge*, **19**(1), pp.40-43.
- Apfel, R. E. (1984). Acoustic cavitation inception, *Ultrasonics* **22**(4), 167-173.
- Arakeri, V. H., and Shanmuganathan, V. (1985). On the evidence for the effect of bubble interference on cavitation noise, *Journal of Fluid Mechanics*, **159**, 131-150.
- Askeland, B., Hobæk, H., and Mjelde, R., (2007). 2007. Marine seismics with a pulsed combustion source and Pseudo Noise codes. *Marine Geophysical Researches*, **28**(2), pp.109-117.
- Banda, N. and Blondel, P., 2016, Identifying mid-water targets using the higher frequencies emitted by seismic sources of opportunity, In *Oceans'16 MTS/IEEE Monterey* (pp. 1-7). IEEE.

References

- Barclay, F.I., Ledwedge, T.J., and Cornfield, G.C., 1969. Some Experiments on Sonic Velocity in Two-Phase One-Component Mixtures and Some Thoughts on the Nature of Two-Phase Critical Flow, In Proceedings of the Institution of Mechanical Engineers, **184**(3C) 185-91.
- Barger, J.E. and Hamblen, W.R., 1980. The air gun impulsive underwater transducer. The Journal of the Acoustical Society of America, **68**(4), pp.1038-1045.
- Barlow, J. and Gisiner, R., 2006. Mitigating, monitoring and assessing the effects of anthropogenic sound on beaked whales. Journal of Cetacean Research and Management, **7**(3), pp.239-249.
- Bataller, A., Kappus, B., Camara, C. and Putterman, S., 2014. Collision time measurements in a sonoluminescing microplasma with a large plasma parameter. Physical review letters, **113**(2), p.024301.
- Behura, J. and Snieder, R., 2013. Virtual real source: Source signature estimation using seismic interferometry. Geophysics, **78**(5), pp.Q57-Q68.
- Berkhout, A.G., 2008. Changing the mindset in seismic data acquisition. The Leading Edge, **27**(7), pp.924-938.
- Bingham, G. (Ed.), 2011. Status and applications of acoustic mitigation and monitoring systems for marine mammals: Workshop proceedings; November 17-19, 2009, Boston, Massachusetts OCS Study BOEMRE 2011-002, New Orleans, LA. U.S. Dept. of the Interior, Bureau of Ocean Energy Management, Regulation, and Enforcement, Gulf of Mexico OCS Region
- Bojarski, N.N., 1982. The k-space formulation of the scattering problem in the time domain. The Journal of the Acoustical Society of America, **72**(2), pp.570-584.
- Botteldooren, D., 1995. Finite-difference time-domain simulation of low-frequency room acoustic problems. The Journal of the Acoustical Society of America, **98**(6), pp.3302-3308.
- Bouyoucos, J. V., 1975. Hydroacoustic transduction, J. Acoust. Soc. Am., **57**(6), 1341-1351.
- Branstetter, B.K., St. Leger, J., Acton, D., Stewart, J., Houser, D., Finneran, J.J. and Jenkins, K., 2017. Killer whale (*Orcinus orca*) behavioral audiograms. The Journal of the Acoustical Society of America, **141**(4), pp.2387-2398.
- Breitzke, M. and Bohlen, T., 2010. Modelling sound propagation in the Southern Ocean to estimate the acoustic impact of seismic research surveys on marine

- mammals. *Geophysical Journal International*, **181**(2), pp.818-846.
- Brennen, C. E. 2013. *Cavitation and Bubble Dynamics* (Cambridge University Press, London).
- Brennen, C., Colonius, T., Wang, Y.C. and Preston, A., 1999. Cloud cavitation phenomena. *The National Academy of Sciences*, pp.239-253.
- Brennen, C.E., 2005. *Fundamentals of multiphase flow*, Cambridge university press.
- Caldwell, J. and Dragoset, W., 2000. A brief overview of seismic air-gun arrays, *The Leading Edge*, **19**(8), pp.898-902.
- Caupin, F. and Herbert, E., 2006. Cavitation in water: a review, *Comptes Rendus Physique*, **7**(9), 1000-1017.
- Ceccio, S.L., 1990. Observations of the dynamics and acoustics of travelling bubble cavitation, PhD thesis, California Institute of Technology Pasadena, California.
- Ceccio, S.L. and Brennen, C.E., 1991. Observations of the dynamics and acoustics of travelling bubble cavitation. *Journal of Fluid Mechanics*, **233**, pp.633-660.
- Chang, W.F. and McMechan, G.A., 1989. Absorbing boundary conditions for 3-D acoustic and elastic finite-difference calculations. *Bulletin of the Seismological Society of America*, **79**(1), pp.211-218.
- Chelminski, S., 2015. Device for marine seismic explorations for deposits, U.S. patent 8,971,152 B2 (February 23, 2014.)
- Chew, L.W., Klaseboer, E., Ohl, S.W. and Khoo, B.C., 2011. Interaction of two differently sized oscillating bubbles in a free field. *Physical Review E*, **84**(6), p.066307.
- Clay, C. S., and H. Medwin, 1977. *Acoustical oceanography: Principles and applications*: John Wiley & Sons
- Commander, K.W. and Prosperetti, A., 1989. Linear pressure waves in bubbly liquids: Comparison between theory and experiments. *The Journal of the Acoustical Society of America*, **85**(2), 732-746.
- Compton, R., Goodwin, L., Handy, R. and Abbott, V., 2008. A critical examination of worldwide guidelines for minimising the disturbance to marine mammals during seismic surveys. *Marine Policy*, **32**(3), pp.255-262.

References

- Cook, M.L., Varela, R.A., Goldstein, J.D., McCulloch, S.D., Bossart, G.D., Finneran, J.J., Houser, D. and Mann, D.A., 2006. Beaked whale auditory evoked potential hearing measurements. *Journal of Comparative Physiology A*, **192**(5), pp.489-495.
- Coste, E., Gerez, D., Groenaas, H., Hopperstad, J. F., Larsen, O. P., Laws, R., Norton, J., Padula, M., and Wolfstirn, M., 2014. Attenuated highfrequency emission from a new design of air-gun, in 84th Annual International Meeting, SEG, Expanded Abstracts, pp. 132-137.
- Cox, B.T., Kara, S., Arridge, S.R. and Beard, P.C., 2007. k-space propagation models for acoustically heterogeneous media: Application to biomedical photoacoustics. *The Journal of the Acoustical Society of America*, **121**(6), pp.3453-3464.
- Domenico, S.N., 1982. Acoustic wave propagation in air-bubble curtains in water, Part I: History and theory. *Geophysics*, **47**(3), 345-353.
- Dragoset, B. 2000. Introduction to air guns and air-gun arrays, *Leading Edge* **19**(8), 892-897.
- Dragoset, W.H., 1988. Marine vibrators and the Doppler effect. *Geophysics*, **53**(11), pp.1388-1398.
- Dragoset, W.H., 1990. Air-gun array specs: a tutorial. *The Leading Edge*, **9**(1), pp.24-32.
- Duren, R. E. 1988. A theory for marine source arrays, *Geophysics*, **53**(5), 650-658.
- Dyndo, M., Wisniewska, D. M., Rojano-Donate, L., and Madsen, P. T. 2015. Harbour porpoises react to low levels of high frequency vessel noise. *Scientific reports*, **5**, 11083
- Erbe, C. and Farmer, D. M., 2000. A software model to estimate zones of impact on marine mammals around anthropogenic noise, *The Journal of the Acoustical Society of America*, **108**(3), 1327-1331.
- Erbe, C., Reichmuth, C., Cunningham, K., Lucke, K. and Dooling, R., 2016. Communication masking in marine mammals: A review and research strategy. *Marine pollution bulletin*, **103**(1-2), pp.15-38.
- Finneran, J.J., Schlundt, C.E., Dear, R., Carder, D.A. and Ridgway, S.H., 2002. Temporary shift in masked hearing thresholds in odontocetes after exposure to single underwater impulses from a seismic watergun. *The Journal of the Acoustical Society of America*, **111**(6), pp.2929-2940.

- Finneran, J. J. and Schlundt, C. E. 2009. Auditory weighting functions and frequency-dependent effects of sound in bottlenose dolphins (*Tursiops truncatus*), in 2009 ONR Marine Mammal Program Review (Alexandria, VA)
- Finneran, J.J. 2010. Auditory weighting functions and frequency-dependent effects of sound in bottlenose dolphins (*Tursiops truncatus*),(Office of Naval Research (ONR), Washington, DC)
- Finneran, J.J. and Schlundt, C.E., 2011. Subjective loudness level measurements and equal loudness contours in a bottlenose dolphin (*Tursiops truncatus*). *The Journal of the Acoustical Society of America*, **130**(5), pp.3124-3136.
- Finneran, J.J. and Jenkins, A.K., 2012. Criteria and thresholds for US Navy acoustic and explosive effects analysis. SPACE AND NAVAL WARFARE SYSTEMS CENTER PACIFIC SAN DIEGO CA.
- Finneran, J.J., 2015. Noise-induced hearing loss in marine mammals: A review of temporary threshold shift studies from 1996 to 2015. *The Journal of the Acoustical Society of America*, **138**(3), pp.1702-1726.
- Franc, J.P. and Michel, J.M., 1988. Unsteady attached cavitation on an oscillating hydrofoil. *Journal of Fluid Mechanics*, **193**, pp.171-189.
- Francois, R.E. and Garrison, G.R., 1982. Sound absorption based on ocean measurements. Part II: Boric acid contribution and equation for total absorption. *The Journal of the Acoustical Society of America*, **72**(6), pp.1879-1890.
- Frohly, J., Labouret, S., Bruneel, C., Looten-Baquet, I. and Torguet, R., 2000. Ultrasonic cavitation monitoring by acoustic noise power measurement. *The Journal of the Acoustical Society of America*, **108**(5), pp.2012-2020.
- Fuster, D. and Montel, F., 2015. Mass transfer effects on linear wave propagation in diluted bubbly liquids. *Journal of Fluid Mechanics*, **779**, pp.598-621.
- Gerez, D., Groenaas, H., Larsen, O. P., Wolfstirn, M., and Padula, M., 2015, December. Controlling air-gun output to optimize seismic content while reducing unnecessary high-frequency emissions, In 2015 SEG Annual Meeting. Society of Exploration Geophysicists.
- Gisiner, R.C., 2016. Sound and marine seismic surveys. *Acoustics Today*, **12**(4), pp.9-18.
- Goldbogen, J.A., Southall, B.L., DeRuiter, S.L., Calambokidis, J., Friedlaender, A.S., Hazen, E.L., Falcone, E.A., Schorr, G.S., Douglas, A., Moretti, D.J. and Kyburg, C., 2013. Blue whales respond to simulated mid-frequency military

References

- sonar. Proceedings of the Royal Society B: Biological Sciences, **280**(1765), p.20130657.
- Goold, J.C. and Fish, P.J., 1998. Broadband spectra of seismic survey air-gun emissions, with reference to dolphin auditory thresholds. The Journal of the Acoustical Society of America, **103**(4), pp.2177-2184.
- Gordon, J. and Steiner, L., 1992. Ventilation and dive patterns in sperm whales, *Physeter macrocephalus*, in the Azores. Report of the International Whaling Commission, **42**, pp.561-565.
- Gordon, J., Gillespie, D., Potter, J., Frantzis, A., Simmonds, M.P., Swift, R. and Thompson, D., 2003. A review of the effects of seismic surveys on marine mammals. Marine Technology Society Journal, **37**(4), pp.16-34.
- Groenaas, H., Gerez, D., Larsen, O.P., and Padula, M., 2016. On the anatomy of the air-gun signature, in SEG Technical Program Expanded Abstracts (pp. 46-50). Society of Exploration Geophysicists.
- Guan, S., Vignola, J., Judge, J. and Turo, D., 2015. Airgun inter-pulse noise field during a seismic survey in an Arctic ultra shallow marine environment. The Journal of the Acoustical Society of America, **138**(6), pp.3447-3457.
- Hadi, M.F. and Picket-May, M., 1997. A modified FDTD (2, 4) scheme for modeling electrically large structures with high-phase accuracy. IEEE Transactions on Antennas and Propagation, **45**(2), pp.254-264.
- Hamilton, E.L., 1978. Sound velocity–density relations in sea–floor sediments and rocks. The Journal of the Acoustical Society of America, **63**(2), pp.366-377.
- Hampson, G., J. Stefani, and F. Herkenhoff, 2008, Acquisition using simultaneous sources: Leading Edge, **27**, 918-923.
- Hanssen, A., Mjølhus, E., DuBois, D.F. and Rose, H.A., 1992. Numerical test of the weak turbulence approximation to ionospheric Langmuir turbulence. Journal of Geophysical Research: Space Physics, **97**(A8), pp.12073-12091.
- Harrison, M., 1952. An experimental study of single bubble cavitation noise. The Journal of the Acoustical Society of America, **24**(6), pp.776-782.
- Herbert, E., Balibar, S. and Caupin, F., 2006. Cavitation pressure in water. Physical Review E, **74**(4), p.041603.
- HESS Team, 1999. High Energy Seismic Survey review process and interim operational guidelines for marine surveys offshore Southern California. Rep. from

- High Energy Seismic Survey Team for Calif. State Lands Commis. and Minerals Manage. Serv., Camarillo, CA. 39 p.+ Appendices. Rep. from High Energy Seismic Survey Team for Calif. State Lands Commis. and Minerals Manage. Serv., Camarillo, CA.
- Hildebrand, J. A. 2009. Anthropogenic and natural sources of ambient noise in the ocean, *Marine Ecology Progress Series* **395**, 5-20. (doi:10.3354/meps08353)
- Hilgenfeldt, S., Lohse, D. and Zomack, M., 1998. Response of bubbles to diagnostic ultrasound: a unifying theoretical approach, *Eur. Phys. J. B-Condensed Matter and Complex Systems*, **4**(2), pp.247-255.
- Houser, D.S., Yost, W., Burkard, R., Finneran, J.J., Reichmuth, C. and Mulsow, J., 2017. A review of the history, development and application of auditory weighting functions in humans and marine mammals. *The Journal of the Acoustical Society of America*, **141**(3), pp.1371-1413.
- Isojunno, S., Cure, C., Kvadsheim, P.H., Lam, F.P.A., Tyack, P.L., Wensveen, P.J., and Miller, P.J.O.M. (2016). Sperm whales reduce foraging effort during exposure to 1-2 kHz sonar and killer whale sounds. *Ecological Applications*, **26**(1), 77-93.
- Johnson, S.R., Richardson, W.J., Yazvenko, S.B., Blokhin, S.A., Gailey, G., Jenkerson, M.R., Meier, S.K., Melton, H.R., Newcomer, M.W., Perlov, A.S. and Rutenko, S.A., 2007. A western gray whale mitigation and monitoring program for a 3-D seismic survey, Sakhalin Island, Russia. *Environmental Monitoring and Assessment*, **134**(1-3), p.1
- Joint Nature Conservation Committee 2017. Guidelines for minimizing the risk of injury to marine mammals from geophysical surveys, Aberdeen, Scotland, UK
- Joint Nature Conservation Committee, 2004. Guidelines for minimising acoustic disturbance to marine mammals from seismic surveys. Joint Nature Conservation Committee, Aberdeen, Scotland, UK.
- Kastelein, R.A., Gransier, R., Hoek, L. and Olthuis, J., 2012. Temporary threshold shifts and recovery in a harbor porpoise (*Phocoena phocoena*) after octave-band noise at 4 kHz. *The Journal of the Acoustical Society of America*, **132**(5), pp.3525-3537.
- Kastelein, R.A., Hoek, L., de Jong, C.A. and Wensveen, P.J., 2010. The effect of signal duration on the underwater detection thresholds of a harbor porpoise (*Phocoena phocoena*) for single frequency-modulated tonal signals between 0.25 and 160 kHz. *The Journal of the Acoustical Society of America*, **128**(5),

References

pp.3211-3222

- Ketten, D.R., 2004. Marine mammal auditory systems: A summary of audiometric and anatomical data and implications for underwater acoustic impacts, *Polarforschung* **72**(2-3), 79-92.
- Khodabandloo, B. and Landrø, M., 2017a, June. Effects of Ghost Cavity cloud on Near-field Hydrophones Measurements in the Seismic Air Gun Arrays. In 79th EAGE Conference and Exhibition 2017., Paper Tu A4 09
- Khodabandloo, B. and Landrø, M., 2017b. High frequency ghost cavitation—a comparison of two seismic air-gun arrays using numerical modelling. *Energy Procedia*, **125**, 153-160.
- Khodabandloo, B., Landrø, M. and Hanssen, A., 2017. Acoustic generation of underwater cavities—Comparing modeled and measured acoustic signals generated by seismic air gun arrays. *The Journal of the Acoustical Society of America*, **141**(4), pp.2661-2672.
- Khodabandloo, B. and Landrø, M., 2018. Acoustically induced cavity cloud generated by air-gun arrays – Comparing video recordings and acoustic data to modeling. *The Journal of the Acoustical Society of America*, **143**(6), pp.3383-3393.
- Kieffer, S.W., 1977. Sound speed in liquid–gas mixtures: Water–air and water–steam. *Journal of Geophysical research*, **82**(20), pp.2895-2904.
- Kim, K.H., Chahine, G., Franc, J.P., and Karimi, A. (Eds.), 2014. *Advanced experimental and numerical techniques for cavitation erosion prediction* (Vol. 106). (Springer Dordrecht Heidelberg New York London), DOI 10.1007/978-94-017-8539-6
- King, J.R.C., Ziolkowski, A. M., and Ruffert, M., 2015a. Boundary conditions for simulations of oscillating bubbles using the non-linear acoustic approximation, *Journal of Computational Physics* , **284**, 273-290.
- King, J. R., 2015b. Air-gun bubble-ghost interactions, *Geophysics*, **80**(6), T223-T234.
- La Prairie, A.J.C., *Method of Blasting*: U.S. Patent No. 2699117, 1955.
- Landrø, M., Strandenes, S. and Vaage, S., 1991. Use of near-field measurements to compute far-field marine source signatures-Evaluation of the method. *First break*, **9**(8), pp.375-385.

- Landrø, M., and Amundsen, L. 2010. Marine seismic sources part 1: Air-guns for non experts. *Geo ExPro* **7**, pp 32-34.
- Landrø, M., Amundsen, L., and Barker, D., 2011. High-frequency signals from air-gun arrays, *Geophysics*, **76**(4), Q19-Q27.
- Landrø, M., Amundsen, L., and Langhammer, J., 2013. Repeatability issues of high-frequency signals emitted by air-gun arrays, *Geophysics*, **78**(6), P19-P27.
- Landrø, M., Ni, Y., and Amundsen, L. 2016. Reducing high-frequency ghost cavitation signals from marine air-gun arrays, *Geophysics* **81**(3), P33-P46.
- Landrø, M., Hansteen, F., and Amundsen, L., 2017. Detecting gas leakage using high-frequency signals generated by air-gun arrays, *Geophysics* **82**(2) A7-A12.
- Lauterborn, W. and Hentschel, W., 1985. Cavitation bubble dynamics studied by high speed photography and holography: part one, *Ultrasonics*, **23**(6), pp.260-268.
- Lawrence, E.K., Austin, R.F., Alan, B.C. and James, V.S., 2000. *Fundamentals of acoustics*. New Yorks: John wileys, c2000, chapter 7
- Laws, R., Landrø, M. and Amundsen, L., 1998. An experimental comparison of three direct methods of marine source signature estimation. *Geophysical prospecting*, **46**(4), pp.353-389.
- Lee, K.M., Hinojosa, K.T., Wochner, M.S., Argo, T.F., Wilson, P.S. and Mercier, R.S., 2011. Sound propagation in water containing large tethered spherical encapsulated gas bubbles with resonance frequencies in the 50 Hz to 100 Hz range. *The Journal of the Acoustical Society of America*, **130**(5), pp.3325-3332.
- Leighton T.G., 1994. *The Acoustic Bubble* (Academic, San Diego, 1994), pp 258-278.
- Leighton, T., 2012. *The Acoustic Bubble* (Academic Press, New York)
- Lewis, T., Gillespie, D., Gordon, J. and Chappell, O., 2000. Acoustic cetacean monitoring 1996 to 1999: towards the development of an automated system.
- Li, F., Cai, J., Huai, X. and Liu, B., 2013. Interaction mechanism of double bubbles in hydrodynamic cavitation. *Journal of Thermal Science*, **22**(3), pp.242-249.
- Liu, Q.H., 1997. The PSTD algorithm: A time-domain method requiring only two cells per wavelength. *Microwave and optical technology letters*, **15**(3), pp.158-165.

References

- Liu, Q.H., 1998. The pseudospectral time-domain (PSTD) algorithm for acoustic waves in absorptive media. *IEEE transactions on ultrasonics, ferroelectrics, and frequency control*, **45**(4), pp.1044-1055.
- Løkkeborg, S., E. Ona, A. Vold, H. Pena, A. Salthaug, B. Totland, J. T. øvredal, J. Dalen, and N. O. Handegard, Effects of seismic surveys on fish distribution and catch rates of gillnets and longlines in Vesterålen in summer 2009. *Fisken og Havet No 2*, The Institute of Marine Research (2010).
- Long, A. and TENGHAMN, R., 2018. Marine Vibrator Concepts for Modern Seismic Challenges. *ASEG Extended Abstracts*, 2018(1), pp.1-4.
- Lucke, K., Lepper, P.A., Blanchet, M.A. and Siebert, U., 2011. The use of an air bubble curtain to reduce the received sound levels for harbor porpoises (*Phocoena phocoena*). *The Journal of the Acoustical Society of America*, **130**(5), pp.3406-3412.
- Lucke, K., Siebert, U., Lepper, P.A. and Blanchet, M.A., 2009. Temporary shift in masked hearing thresholds in a harbor porpoise (*Phocoena phocoena*) after exposure to seismic airgun stimuli. *The Journal of the Acoustical Society of America*, **125**(6), pp.4060-4070.
- Madsen, P.T., 2005. Marine mammals and noise: Problems with root mean square sound pressure levels for transients. *The Journal of the Acoustical Society of America*, **117**(6), pp.3952-3957.
- Madsen, P.T., Johnson, M., Miller, P.J.O., Aguilar Soto, N., Lynch, J. and Tyack, P.L., 2006. Quantitative measures of air-gun pulses recorded on sperm whales (*Physeter macrocephalus*) using acoustic tags during controlled exposure experiments. *The Journal of the Acoustical Society of America*, **120**(4), pp.2366-2379.
- Mast, T.D., Souriau, L.P., Liu, D.L., Tabei, M., Nachman, A.I. and Waag, R.C., 2001. A k-space method for large-scale models of wave propagation in tissue. *IEEE transactions on ultrasonics, ferroelectrics, and frequency control*, **48**(2), pp.341-354.
- McCauley, R.D., Fewtrell, J., Duncan, A.J., Jenner, C., Jenner, M.N., Penrose, J.D., Prince, R.I., Adhitya, A., Murdoch, J. and McCabe, K., 2000. *Marine seismic surveys: analysis and propagation of air gun signals and effects of air gun exposure on humpback whales, sea turtles, fishes and squid* (Vol. 163). Perth, Australia: Curtin University of Technology, Project CMST.

- McNamara, W.B., Didenko, Y.T. and Suslick, K.S., 1999. Sonoluminescence temperatures during multi-bubble cavitation, *Nature*, **401**(6755), pp.772-775.
- Medwin, H., 1977. In situ acoustic measurements of microbubbles at sea. *Journal of Geophysical Research*, **82**(6), pp.971-976.
- Mellen, R.H., 1954. Ultrasonic spectrum of cavitation noise in water. *The Journal of the Acoustical Society of America*, **26**(3), pp.356-360.
- Miller, P.J., Kvadsheim, P.H., Lam, F.P.A., Wensveen, P.J., Antunes, R., Alves, A.C., Visser, F., Kleivane, L., Tyack, P.L. and Sivle, L.D., 2012. The severity of behavioral changes observed during experimental exposures of killer (*Orcinus orca*), long-finned pilot (*Globicephala melas*), and sperm (*Physeter macrocephalus*) whales to naval sonar. *Aquatic Mammals*, **38**(4), p.362.
- Miller, P.J., Kvadsheim, P.H., Lam, F.P.A., Tyack, P.L., Curé, C., DeRuiter, S.L., Kleivane, L., Sivle, L.D., van IJsselmuide, S.P., Visser, F. and Wensveen, P.J., 2015. First indications that northern bottlenose whales are sensitive to behavioural disturbance from anthropogenic noise. *Royal Society open science*, **2**(6), p.140484.
- Mjøllhus, E., Hanssen, A., and DuBois, D.F., 1995. Radiation from electromagnetically driven Langmuir turbulence, *Journal of Geophysical Research*, **100**(A9), pp.17-527.
- Mooney, T.A., Nachtigall, P.E., Breese, M., Vlachos, S. and Au, W.W., 2009. Predicting temporary threshold shifts in a bottlenose dolphin (*Tursiops truncatus*): The effects of noise level and duration. *The Journal of the Acoustical Society of America*, **125**(3), pp.1816-1826.
- Mooney, T.A., Yamato, M. and Branstetter, B.K., 2012. Hearing in cetaceans: from natural history to experimental biology. In *Advances in marine biology* (Vol. 63, pp. 197-246). Academic Press.
- Moore, I., Dragoset, B., Ommundsen, T., Wilson, D., Eke, D. and Ward, C., 2008, January. Simultaneous source separation using dithered sources. In 2008 SEG Annual Meeting. Society of Exploration Geophysicists.
- Morozov, A.K. and Webb, D.C., 2007. Underwater tunable organ-pipe sound source. *The Journal of the Acoustical Society of America*, **122**(2), pp.777-785.
- Mougenot, J.M., Griswold, S., Jenkerson, M. and Abma, R., 2017. Next-generation marine seismic sources: A report from the SEG 2015 postconvention workshop. *The Leading Edge*, **36**(7), pp.598-603.

References

- Mueller, M. B., D. F. Halliday, D.-J. van Manen, and J. O. A. Robertsson, 2015, The benefit of encoded source sequences for simultaneous source separation: *Geophysics*, **80**, V133-V143.
- Muller, M.B., 2016. Encoding techniques for marine seismic sources & their applications (Doctoral dissertation, ETH Zurich).
- Mulsow, J., Schlundt, C.E., Brandt, L. and Finneran, J.J., 2015. Equal latency contours for bottlenose dolphins (*Tursiops truncatus*) and California sea lions (*Zalophus californianus*). *The Journal of the Acoustical Society of America*, **138**(5), pp.2678-2691.
- Nachtigall, P.E., Yuen, M.M., Mooney, T.A. and Taylor, K.A., 2005. Hearing measurements from a stranded infant Risso's dolphin, *Grampus griseus*. *Journal of Experimental Biology*, **138**(21), pp.4181-4188.
- National Marine Fisheries Service. 2016. Technical Guidance for Assessing the Effects of Anthropogenic Sound on Marine Mammal Hearing: Underwater Acoustic Thresholds for Onset of Permanent and Temporary Threshold Shifts. U.S. Dept. of Commer., NOAA. NOAA Technical Memorandum NMFS-OPR-55, 178 p.
- National Research Council (NRC), 2003. *Ocean Noise and Marine Mammals* (National Academic Press, Washington, DC), pp. 83-108.
- Nayar, K.G., Panchanathan, D., McKinley, G.H. and Lienhard, J.H., 2014. Surface tension of seawater. *Journal of Physical and Chemical Reference Data*, **43**(4), p.043103.
- Nedwell, J.R., Turnpenney, A.W.H., Lovell, J., Parvin, S.J., Workman, R., Spinks, J.A.L. and Howell, D., 2007. A validation of the dBht as a measure of the behavioural and auditory effects of underwater noise. Subacoustech Report Reference: 534R1231, Published by Department for Business, Enterprise and Regulatory Reform.
- Neppiras, E.A., 1984. Acoustic cavitation series: part one: Acoustic cavitation: an introduction. *Ultrasonics*, **22**(1), 25-28.
- Nobes, D.C., Villinger, H., Davis, E.E. and Law, L.K., 1986. Estimation of marine sediment bulk physical properties at depth from seafloor geophysical measurements. *Journal of Geophysical Research: Solid Earth*, **91**(B14), pp.14033-14043.
- Norton, M. P. and Karczub, D. G., 2003. *Fundamentals of noise and vibration analysis for engineers*, Cambridge University Press.

- Nowacek, D.P., Thorne, L.H., Johnston, D.W. and Tyack, P.L., 2007. Responses of cetaceans to anthropogenic noise. *Mammal Review*, **37**(2), pp.81-115.
<http://dx.doi.org/10.1111/j.1365-2907.2007.00104.x>.
- Nowacek, D.P., Bröker, K., Donovan, G., Gailey, G., Racca, R., Reeves, R.R., Vedenev, A.I., Weller, D.W. and Southall, B.L., 2013. Responsible practices for minimizing and monitoring environmental impacts of marine seismic surveys with an emphasis on marine mammals. *Aquatic Mammals*, **39**(4), p.356.
- Ozasa, H., Mikada, H., Sato, F., Murakami, F., Takekawa, J. and Asakawa, E., 2015, May. Development of hydraulic low frequency marine seismic vibrator. In *The 19th International Symposium on Recent Advances in Exploration Geophysics (RAEG 2015)*.
- Parkes, G. E., and Hatton, L. 1986. *The Marine Seismic Source*, 1st ed. Springer Science+Business Media, Dordrecht, The Netherlands. doi:10.1007/978-94-017-3385-4.
- Parkes, G.E., Ziolkowski, A., Hatton, L. and Haugland, T., 1984. The signature of an air gun array: Computation from near-field measurements including interactions-practical considerations. *Geophysics*, **49**(2), pp.105-111.
- Parks, S.E., Clark, C.W. and Tyack, P.L., 2007. Short-and long-term changes in right whale calling behavior: the potential effects of noise on acoustic communication. *The Journal of the Acoustical Society of America*, **122**(6), pp.3725-3731.
- Parsons, E.C.M., Dolman, S.J., Jasny, M., Rose, N.A., Simmonds, M.P. and Wright, A.J., 2009. A critique of the UK's JNCC seismic survey guidelines for minimising acoustic disturbance to marine mammals: Best practise?. *Marine Pollution Bulletin*, **58**(5), pp.643-651.
- Pecseli, H.L., 2012. *Waves and oscillations in plasmas*, CRC Press.
- Pierce, A.D. and Beyer, R.T., 1990. *Acoustics: An Introduction to Its Physical Principles and Applications*. 1989 Edition. Chapter 4.
- Pierce, A.D., 1989. *Acoustics: an introduction to its physical principles and applications*. Acoustical Society of America, Huntington Quadrangle Melville, NY.
- Plesset, M.S., 1970. Effect of dissolved gases on cavitation in liquids (No. 85-55), California Institute of Technology, Pasadena Division of Engineering and Applied Science.

References

- Popov, V.V., Supin, A.Y., Rozhnov, V.V., Nechaev, D.I. and Sysueva, E.V., 2014. The limits of applicability of the sound exposure level (SEL) metric to temporal threshold shifts (TTS) in beluga whales, *Delphinapterus leucas*. *Journal of Experimental Biology*, **217**(10), pp.1804-1810
- Pramik, B., Bell, M.L., Grier, A. and Lindsay, A., 2015, December. Field testing the aquavib: An alternate marine seismic source. In 2015 SEG Annual Meeting. Society of Exploration Geophysicists.
- Prosperetti A., 2015. The speed of sound in a gas–vapour bubbly liquid. *Interface Focus* 5: 20150024. <http://dx.doi.org/10.1098/rsfs.2015.0024>
- Prosperetti, A. and Lezzi, A., 1986. Bubble dynamics in a compressible liquid. Part 1. First-order theory. *Journal of Fluid Mechanics*, **168**, pp.457-478.
- Prosperetti, A., 2017. Vapor bubbles. *Annual Review of Fluid Mechanics*, **49**, pp.221-248.
- Rayleigh, L., 1917. On the pressure developed in a liquid during the collapse of a spherical cavity: *Philosophical Magazine Series 6*, **34**, 94–98.
- Reisman, G.E., and Brennen, C.E., 1996. Pressure Pulses Generated by Cloud Cavitation, ASME Symposium on Cavitation and Gas-Liquid Flows in Fluid Machinery and Devices, San Diego, California, FED **236**, pp. 319-328.
- Reisman, G.E., Wang, Y.C. and Brennen, C.E., 1998. Observations of shock waves in cloud cavitation. *Journal of Fluid Mechanics*, **355**, pp.255-283.
- Richardson, W.J., Greene, C.R., Jr., Malme, C.I., and Thomson, D.H., 1995. *Marine mammals and noise*, New York: Academic Press.
- Rienstra, S. W., and Hirschberg, A., 2015. *An Introduction to Acoustics*, Eindhoven Univ. of Technology, Eindhoven, pp. 15-19, 68-70
- Robertsson, J. O. A., D. van Manen, and R. Laws, 2008, Seismic data acquisition and source-side derivatives generation and application: U.S. Patent 7,492,665 B2.
- Rolland, R.M., Parks, S.E., Hunt, K.E., Castellote, M., Corkeron, P.J., Nowacek, D.P., Wasser, S.K. and Kraus, S.D., 2012. Evidence that ship noise increases stress in right whales. *Proceedings of the Royal Society of London B: Biological Sciences*, **279**(1737), pp.2363-2368.
- Ronen, S. and Chelminski, S., 2017. Tuned Pulse Source—a new low frequency seismic source. In SEG Technical Program Expanded Abstracts 2017(pp. 6085-6088). Society of Exploration Geophysicists.

- Ronen, S., Denny, S., Telling, R., Chelminski, S., Young, J., Darling, D. and Murphy, S., 2015, December. Reducing ocean noise in offshore seismic surveys using low-pressure sources and swarms of motorized unmanned surface vessels. In 2015 SEG Annual Meeting. Society of Exploration Geophysicists.
- Ross, D., 1976. Mechanics of underwater noise. Pergamon Press, New York.
- Ross, W.S., Lee, P.J., Heiney, S.E., Young, J.V., Drake, E.N., TENGHAMN, R. and Stenzel, A., 2005. Mitigating seismic noise with an acoustic blanket – the promise and the challenge. *The Leading Edge*, **24**(3), 303-313.
- Russell, D., DuBois, D.F. and Rose, H.A., 1986. Collapsing-caviton turbulence in one dimension. *Physical review letters*, **56**(8), p.838.
- Silberman, E., 1957. Sound velocity and attenuation in bubbly mixtures measured in standing wave tubes. *The journal of the Acoustical Society of America*, **29**(8), pp.925-933.
- Sivle, L.D., Wensveen, P.J., Kvasdheim, P., Lam, F.P.A., Visser, F., Curè, C., Harris, C.M., Tyack, P.L. and Miller, P., 2016. Naval sonar disrupts foraging behaviour in humpback whales. *Marine Ecology Progress Series*. pp 211-220.
- Sornmo, O., Bernhardsson, B., Kröling, O., Gunnarsson, P. and TENGHAMN, R., 2016. Frequency-domain iterative learning control of a marine vibrator. *Control Engineering Practice*, **47**, pp.70-80.
- Southall, B.L., Bowles, A.E., Ellison, W.T., Finneran, J.J., Gentry, R.L., Greene, C.R., Jr., Kastak, D., Ketten, D.R., Miller, J.H., Nachtigall, P.E., Richardson, W.J., Thomas, J.A., and Tyack, P.L., 2007. Marine mammal noise exposure criteria: initial scientific recommendations, *Aquatic Mammals* **33**, 411-521
- Southall, B.L., Bowles, A.E., Ellison, W.T., Finneran, J.J., Gentry, R.L., Greene, C. R., Jr., Kastak, D., Ketten, D.R., Miller, J.H., Nachtigall, P. E., and Richardson, W.J., 2008. Marine mammal noise-exposure criteria: Initial scientific recommendations, *Bioacoustics* **17**(1-3), 273-275
- Spence, J., 2009. Seismic survey noise under examination, *Offshore*, **69**(5).
- Spence, J., Fischer, R., Bahtiarian, M., Boroditsky, L., Jones, N., Dempsey, R., and Life, M., 2007. Review of existing and future potential treatments for reducing underwater sound from oil and gas industry activities, NCE Report, 07-001.
- Stone, C.J. and Tasker, M.L., 2006. The effects of seismic airguns on cetaceans in UK waters. *Journal of Cetacean Research and Management*, **8**(3), p.255.

References

- Tabei, M., Mast, T.D. and Waag, R.C., 2002. A k-space method for coupled first-order acoustic propagation equations. *The Journal of the Acoustical Society of America*, **111**(1), pp.53-63.
- Tabti, H., Høy, T., Wright, A., Barker, D. and Drossaert, F., 2017, June. Shot by Shot Source Wave Field Estimation. In 79th EAGE Conference and Exhibition 2017.
- Tashmukhambetov, A.M., Ioup, G.E., Ioup, J.W., Sidorovskaia, N.A. and Newcomb, J.J., 2008. Three-dimensional seismic array characterization study: Experiment and modeling. *The Journal of the Acoustical Society of America*, **123**(6), pp.4094-4108.
- Tenghamn, R., 2006. An electrical marine vibrator with a flextensional shell. *Exploration Geophysics*, **37**(4), pp.286-291.
- Tenghamn, S.R.L., Pgs Geophysical As, 2013. Marine acoustic vibrator having enhanced low-frequency amplitude. U.S. Patent 8,446,798
- Tougaard, J. and Dähne, M., 2017. Why is auditory frequency weighting so important in regulation of underwater noise?. *The Journal of the Acoustical Society of America*, **142**(4), pp.EL415-EL420.
- Tougaard, J., Wright, A.J. and Madsen, P.T., 2015. Cetacean noise criteria revisited in the light of proposed exposure limits for harbour porpoises. *Marine pollution bulletin*, **90**(1-2), pp.196-208
- Treeby, B.E. and Cox, B.T., 2010. k-Wave: MATLAB toolbox for the simulation and reconstruction of photoacoustic wave fields. *Journal of biomedical optics*, **15**(2), p.021314.
- Treeby, B.E., Jaros, J., Rendell, A.P. and Cox, B.T., 2012. Modeling nonlinear ultrasound propagation in heterogeneous media with power law absorption using ak-space pseudospectral method. *The Journal of the Acoustical Society of America*, **131**(6), pp.4324-4336.
- Verfuss, U.K., Gillespie, D., Gordon, J., Marques, T.A., Miller, B., Plunkett, R., Theriault, J.A., Tollit, D.J., Zitterbart, D.P., Hubert, P. and Thomas, L., 2018. Comparing methods suitable for monitoring marine mammals in low visibility conditions during seismic surveys. *Marine Pollution Bulletin*, **126**, pp.1-18.
- Versluis, M., Schmitz, B., von der Heydt, A., and Lohse, D., 2000. How snapping shrimp snap: through cavitating bubbles, *Science*, **289**(5487), 2114-2117.

- Wang, S., 1996. Finite-difference time-domain approach to underwater acoustic scattering problems. *The Journal of the Acoustical Society of America*, **99**(4), pp.1924-1931.
- Wang, Y.C., and Brennen, C.E., 1999. Numerical computation of shock waves in a spherical cloud of cavitation bubbles, *ASME J. Fluids Eng*, **121**(4), 872-880
- Wang, Y.C. and Brennen, C.E., 1995. The noise generated by the collapse of a cloud of cavitation bubbles, In *ASME* (No. 226, pp. 17-29). American Society of Mechanical Engineers.
- Ward, W.D., 1997. Effects of high intensity sound, *Encyclopedia of Acoustics – Volume three* (Wiley, New York), pp. 1497-1507
- Watson, L., Dunham, E., and Ronen, S., 2016. Numerical modeling of seismic air-guns and low-pressure sources. In *SEG Technical Program Expanded Abstracts* (pp. 219-224). Society of Exploration Geophysicists
- Wei, Z., Phillips, T.F. and Hall, M.A., 2010. Fundamental discussions on seismic vibrators Basic overview on seismic vibrators. *Geophysics*, **75**(6), pp.W13-W25.
- Weilgart, L., 2013. A review of the impacts of seismic airgun surveys on marine life. Submitted to the CBD Expert Workshop on Underwater Noise and its Impacts on Marine and Coastal Biodiversity, 25-27 February 2014, London, UK
- Weir, C.R. and Dolman, S.J., 2007. Comparative review of the regional marine mammal mitigation guidelines implemented during industrial seismic surveys, and guidance towards a worldwide standard. *Journal of International Wildlife Law and Policy*, **10**(1), pp.1-27.
- Wensveen, P.J., Huijser, L.A., Hoek, L. and Kastelein, R.A., 2014. Equal latency contours and auditory weighting functions for the harbour porpoise (*Phocoena phocoena*). *Journal of Experimental Biology*, **217**(3), pp.359-369.
- Williams, R., Clark, C.W., Ponirakis, D. and Ashe, E., 2014. Acoustic quality of critical habitats for three threatened whale populations. *Animal Conservation*, **17**(2), pp.174-185.
- Williams, R.G. and Pollatos, J., 2012. Signal to noise-the key to increased marine seismic bandwidth. *First Break*, **30**(11).
- Wilson, P.S. and Roy, R.A., 2008. An audible demonstration of the speed of sound in bubbly liquids. *American Journal of Physics*, **76**(10), pp.975-981.

References

- Wisniewska, D.M., Johnson, M., Teilmann, J., Siebert, U., Galatius, A., Dietz, R. and Madsen, P.T., 2018. High rates of vessel noise disrupt foraging in wild harbour porpoises (*Phocoena phocoena*). *Proceedings of the Royal Society B: Biological Sciences*, **285**(1872), p.20172314.
- Wood, A. B. 1946. *A Textbook of Sound*. London: G. Bell and Sons Ltd.
- Woolf, D.K., 2001. Fluxes at the Sea Surface. IR Radiometers. Langmuir Circulation and Instability. Surface, Gravity and Capillary Waves. Wave Generation by Wind. Whitecaps and Foam. *J. Phys. Oceanogr*, **22**, p.412.
- Wright, A. J., Soto, N. A., Baldwin, A. L., Bateson, M., Beale, C. M., Clark, C., Deak, T., Edwards, E. F., Fernandez, A., Godinho, A., and Hatch, L. T., 2007. Do marine mammals experience stress related to anthropogenic noise?, *International Journal of Comparative Psychology*. **20**(2), 247-316.
- Wright, A.J. and Cosentino, A.M., 2015. JNCC guidelines for minimising the risk of injury and disturbance to marine mammals from seismic surveys: We can do better. *Marine pollution bulletin*, **100**(1), pp.231-239.
- Wursig, B., Greene Jr, C.R. and Jefferson, T.A., 2000. Development of an air bubble curtain to reduce underwater noise of percussive piling. *Marine environmental research*, **49**(1), pp.79-93.
- Yasui, K., Tuziuti, T., Lee, J., Kozuka, T., Towata, A. and Iida, Y., 2010. Numerical simulations of acoustic cavitation noise with the temporal fluctuation in the number of bubbles. *Ultrasonics sonochemistry*, **17**(2), pp.460-472.
- Yee, K., 1966. Numerical solution of initial boundary value problems involving Maxwell's equations in isotropic media. *IEEE Transactions on antennas and propagation*, **14**(3), pp.302-307.
- Yuen, M.M., Nachtigall, P.E., Breese, M. and Supin, A.Y., 2005. Behavioral and auditory evoked potential audiograms of a false killer whale (*Pseudorca crassidens*). *The Journal of the Acoustical Society of America*, **118**(4), pp.2688-2695.
- Zhang, Y., Guo, Z., Gao, Y. and Du, X., 2018. Acoustic wave propagation in bubbly flow with gas, vapor or their mixtures. *Ultrasonics sonochemistry*, **40**, pp.40-45.
- Ziolkowski, A., 1970. A method for calculating the output pressure waveform from an air gun. *Geophysical Journal International*, **21**(2), pp.137-161.
- Ziolkowski, A., Parkes, G., Hatton, L. and Haugland, T., 1982. The signature of an air gun array: Computation from near-field measurements including interac-

- tions. *Geophysics*, **47**(10), pp.1413-1421.
- Zygidis, T.T. and Tsiboukis, T.D., 2004. Higher-order finite-difference schemes with reduced dispersion errors for accurate time-domain electromagnetic simulations. *International Journal of Numerical Modelling: Electronic Networks, Devices and Fields*, **17**(5), pp.461-486.